NASA CR-137748

SMALL SCALE NOISE AND WIND TUNNEL TESTS OF UPPER SURFACE BLOWING NOZZLE FLAP CONCEPTS

VOLUME II. ACOUSTIC TEST RESULTS

Prepared by

Yoram Kadman

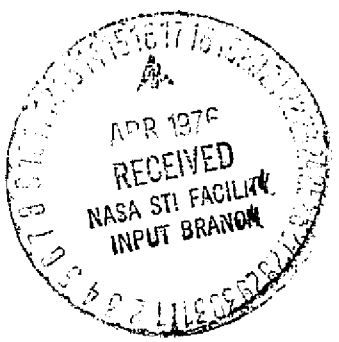

January 1976

Prepared Under Contract NAS2-8607
By Bolt Beranek and Newman, Inc.
Cambridge, Mass.
For
ROCKWELL INTERNATIONAL CORPORATION
Los Angeles, California
For
AMES RESEARCH CENTER
NATIONAL AERONAUTICS AND SPACE ADMINISTRATION

FOREWORD

This report summarizes the acoustic test results on two advanced concepts of upper-surface-blowing propulsive lift devices.

In a companion report, NASA CR-137747, which was prepared by Rockwell International Corporation, the aerodynamic characteristics of the same devices is summarized.

The work described in this report was performed by Bolt Beranek and Newman for Rockwell International, under NASA Ames Research Center Contract No. NAS2-8607.

This report has been designated BBN Report No. 3130.

SUMMARY

The viability and utility of short-takeoff-and-landing (STOL) aircraft will be determined by both the aerodynamic and acoustic performance of the propulsive lift devices used to power these aircraft.

This report deals with some advanced concepts of upper-surface-blowing (USB) devices which were designed to attain acceptable noise levels, both in the community and inside the aircraft, while minimizing or eliminating the aerodynamic performance penalties usually associated with noise suppressing nozzles.

The underlying principle of this approach is that by forcing the propulsive lift flow to turn through a cascade of large aspect-ratio slots, efficient turning at lower noise levels will result. The small size of the slots will also shift the noise spectra to higher frequencies, where the atmospheric attenuation is more effective. The potentially serious problem of cabin interior low frequency noise is also alleviated since the fuselage can attenuate the high frequencies which result from the slotted nozzles.

An additional, and perhaps the most important, advantage of the multislot nozzle concept is that the high frequency noise that results from these devices can be reduced *at the source* by modifying the noise generation mechanisms. Porous edges and edge blowing are the type of methods that are readily applicable to the slotted nozzle design. This study, however, deals only with the effects on the noise of the slot's size and location. No attempt has been made to modify the composition of the individual elements or the detailed structure of the flow around these individual elements.

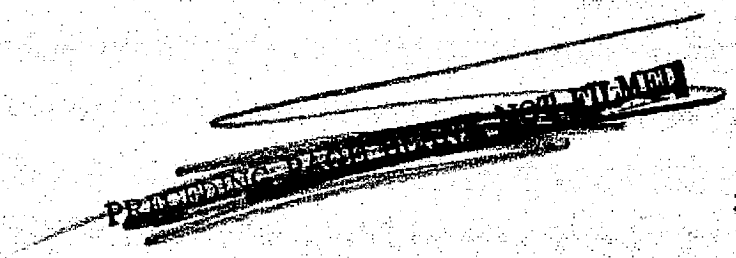

This series of tests dealt with two 1/5-scale models of propulsive lift devices, the first having a 7-slot nozzle, including 2-slot articulating flap, and the second having a split nozzle with 4-slot articulating flap.

This summary also includes, for comparison, test results from a previous investigation [1]* of a 14-slot nozzle and a Coanda Nozzle.

Table 1 summarizes the predicted acoustic performance of the full scale aircraft. These results have been scaled from the model tests.

The results, when expressed in PNdB, show that the 7-slot nozzle and the 14-slot nozzle are about equal in performance and are generally quieter than the split flow nozzle or the Coanda nozzle. However, the noise levels when expressed in PNdB tend to obscure the fact that the Coanda Nozzle is much richer in low frequency noise than the multislotted nozzles. In order to clarify this point the table includes the reduction in the low frequency noise peak of the various devices as compared to the Coanda nozzle at nozzle flap angle of 60°. While this comparison is strictly valid only at the same flap deflections for all devices, it is believed that the values will not change by more than 2 dB for any value of the Coanda flap setting.

It is estimated that the high frequency noise can be reduced by about 6 dB (with comparable reductions in the Perceived Noise levels) by treating the noise sources on the individual flaps in the manner alluded to above.

---

*The numbers in brackets refer to the references at the end of the report.

TABLE 1. PREDICTED ACOUSTIC PERFORMANCE OF USB STOL CONCEPTS.

Model data scaled to full scale condition.
21,800 Kg (48,000 lbs) aircraft powered by 4 engines,
26,800 N (6000 lbs) thrust each.
Propulsive jet velocity is 244 m/s (800 fps) at full power (takeoff),
172 m/s (565 fps) at half power (landing).
No forward speed effects.
Standard day condition (15°C, 70% relative humidity).

USB Device	Propulsive Nozzle Flap Angle δ_N[Deg]	Mechanical Flap Angle δ_F[Deg]	Noise Level at Takeoff [PNdB] 152 m (500 ft) Sideline (full power)	Reduction of Low Frequency (200 Hz) Noise Peak* [dB]	Noise Level at Landing [PNdB] 113 m (370 ft) Under Aircraft (half power)	Reduction of Low Frequency (160 Hz) Noise Peak* [dB]	Interior Noise Level (full power) [PNdB]
Split Nozzle	40	40	96	12	93.1	7	101.5
	60	60	97.6	10	97.5	6	103.7
	90	90	98.5	11	92	5	104.3
7-Slot Nozzle	40	40	93.4	14	92.6	9	98.2
	60	60	95	13	94.5	10	100.3
	90	60	98	12	93.4	7	101.8
14-Slot Nozzle	40	40	95.5	12	90.9	9	100.7
	60	60	98.2	11	95.2	10	102.0
	90	60	95.6	9	91.2	10	100.6
Coanda	60	60	98.1	0	93.5	0	103.6

*Compared to Coanda nozzle at δ_N = 60°.

TABLE OF CONTENTS

LIST OF FIGURES

LIST OF TABLES

1. INTRODUCTION

The noise problem associated with propulsive lift devices for STOL aircraft is recognized as one of the main obstacles to their acceptance.

This report is a continuation of an effort to evaluate the concept of slotted nozzles as USB propulsive lift devices. The feasibility of the concept was proven [2], and later incorporated into a small scale semispan model as a 14-slot nozzle [1,3]. In the above studies, it was shown that the slotted nozzles were quieter than the Coanda nozzle and that the low frequency noise levels associated with conventional USB or EBF concept were reduced by as much as 20 dB.

This report summarizes the acoustic behavior of two additional variations on the theme of multislotted nozzle, the Split-Flow nozzle, and the 7-slot nozzle. These nozzles are shown, schematically in Figs. 1 and 2 where the drawing of the 14-slot nozzle is also included. A detailed description of the nozzles, together with the aerodynamic evaluation of their performance is given in a companion report [4].

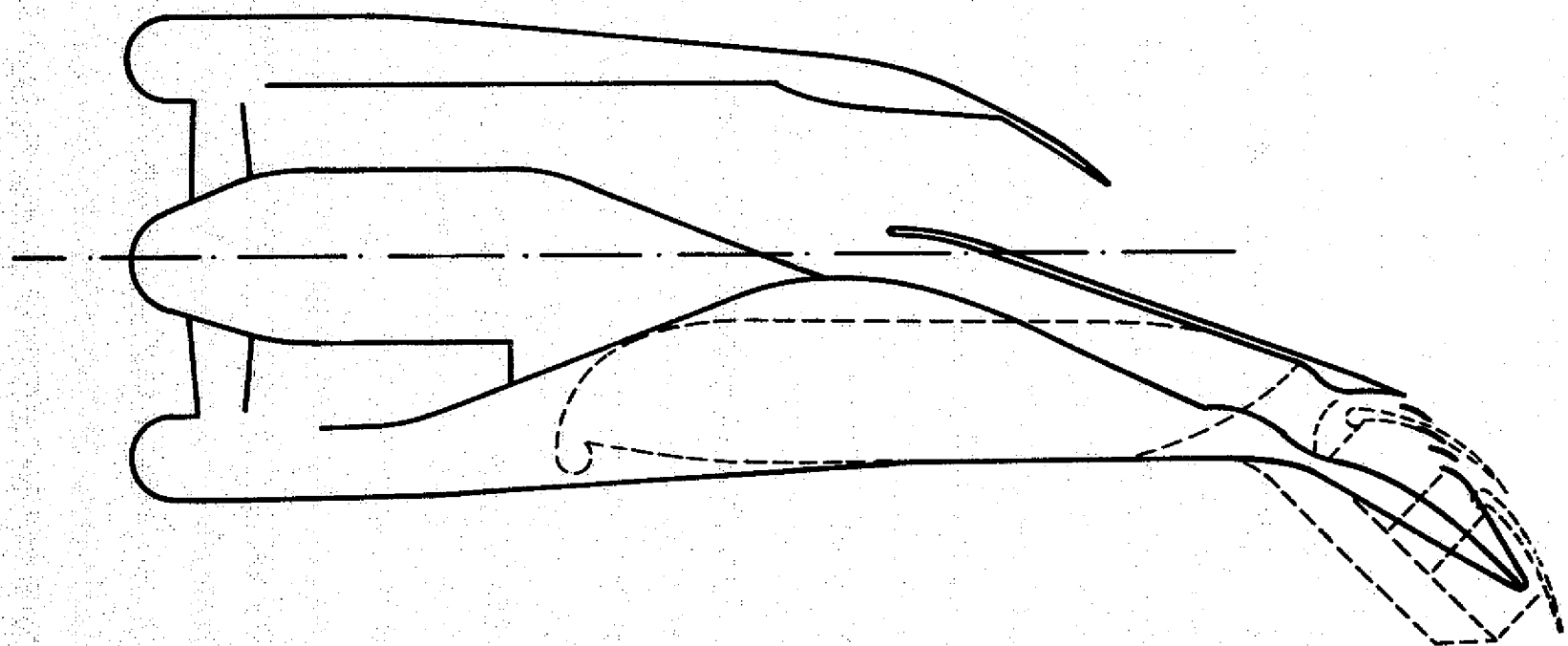

FIG. 1. SPLIT FLOW NOZZLE.

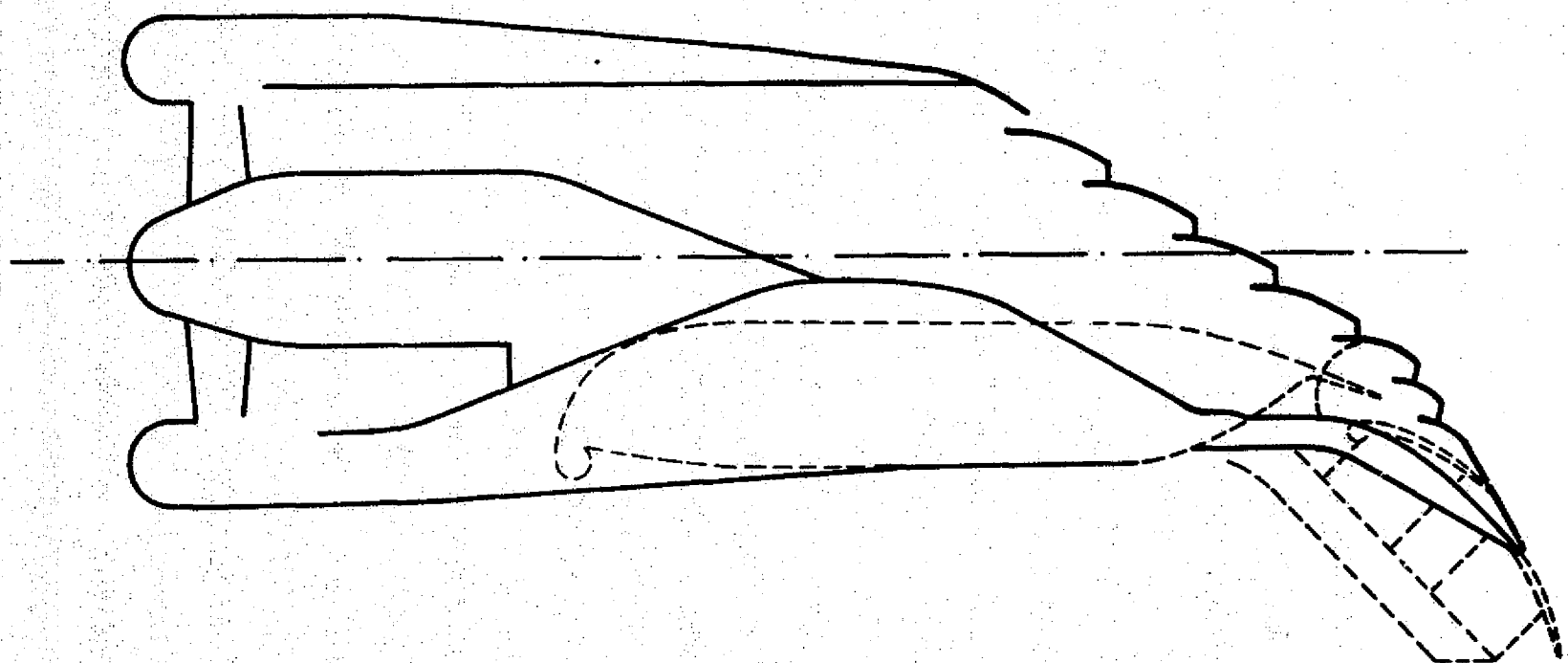

FIG. 2(a). 7-SLOT NOZZLE.

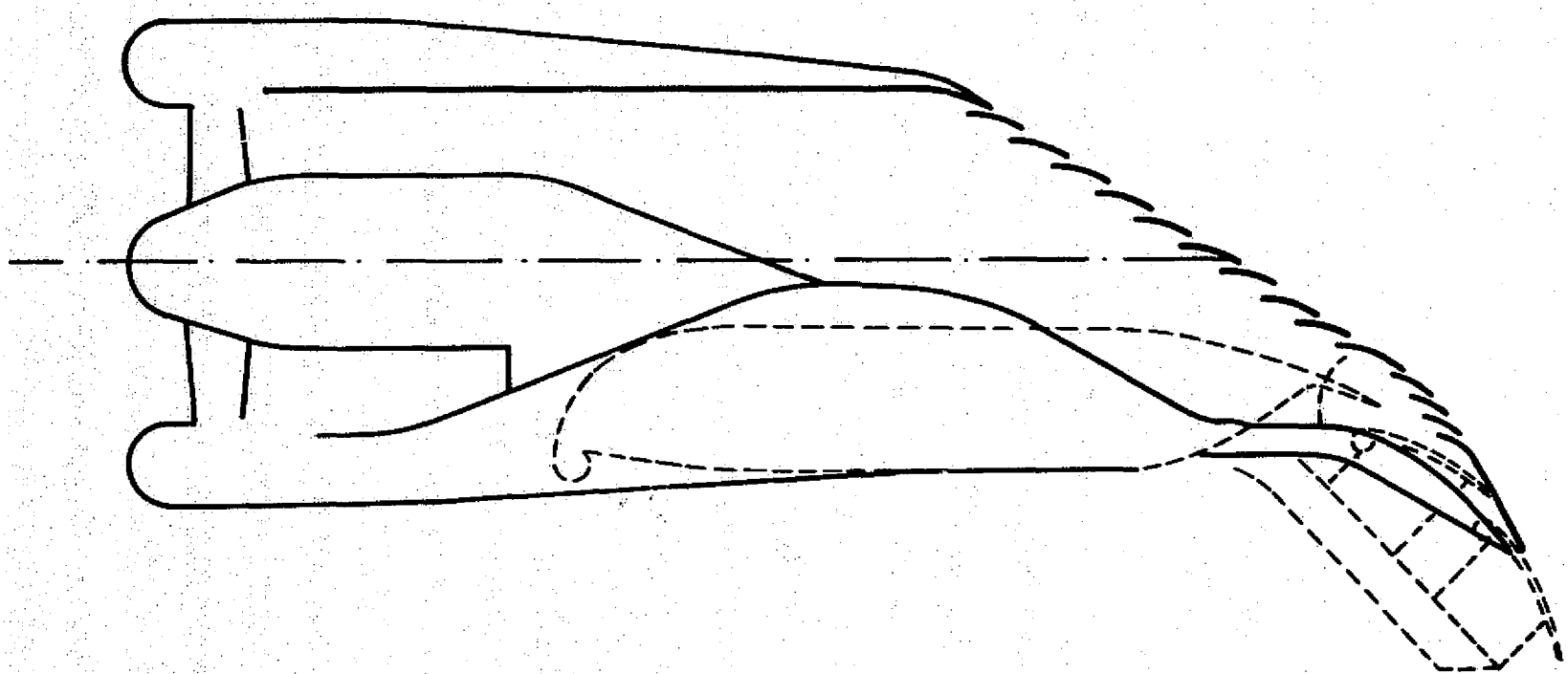

FIG. 2(b). 14-SLOT NOZZLE.

2. EXPERIMENTAL ARRANGEMENT

2.1 The Test Facility

The model of the propulsive wing was placed in BBN's large free jet acoustic wind tunnel. The tunnel test chamber was used in the anechoic mode. Figures 3 (a,b) show two views of this facility.

The propulsive lift nozzles were supplied with quiet, high pressure air from a remote compressor (the Tech Development tip driven fan used to power the models for the aerodynamic tests is too noisy for the acoustic tests). Figure 4 depicts the model installed in the tunnel test section. Since no forward speed tests were carried out in this effort, the tunnel was used as a large anechoic test chamber.

2.2 The Experimental Set Up and Instrumentation

Figure 5 shows the microphone arrangement used to acquire the data. Three microphones were used in this test. The first, a boom mounted microphone, measured the noise in the flyover plane. Two stationary microphones were used to measure the sideline noise levels. One sideline location (22° SL) corresponds to the 152 m (500 ft) sideline, 61 m (200 ft) altitude measuring point and the other (36° SL) corresponds to 152 m (500 ft) sideline and 113 m (370 ft) altitude measuring point. All microphones used were 1/4-inch B&K type 4135 without protective grid, having a calibrated frequency response to 80 kHz. The microphone output was fed, through an amplifier, to a General Radio Type 1971 one-third octave band Real Time Analyzer. The nozzle flow velocity was measured by the total head probe inside the nozzle.

Table 2 summarizes the experimental test matrix.

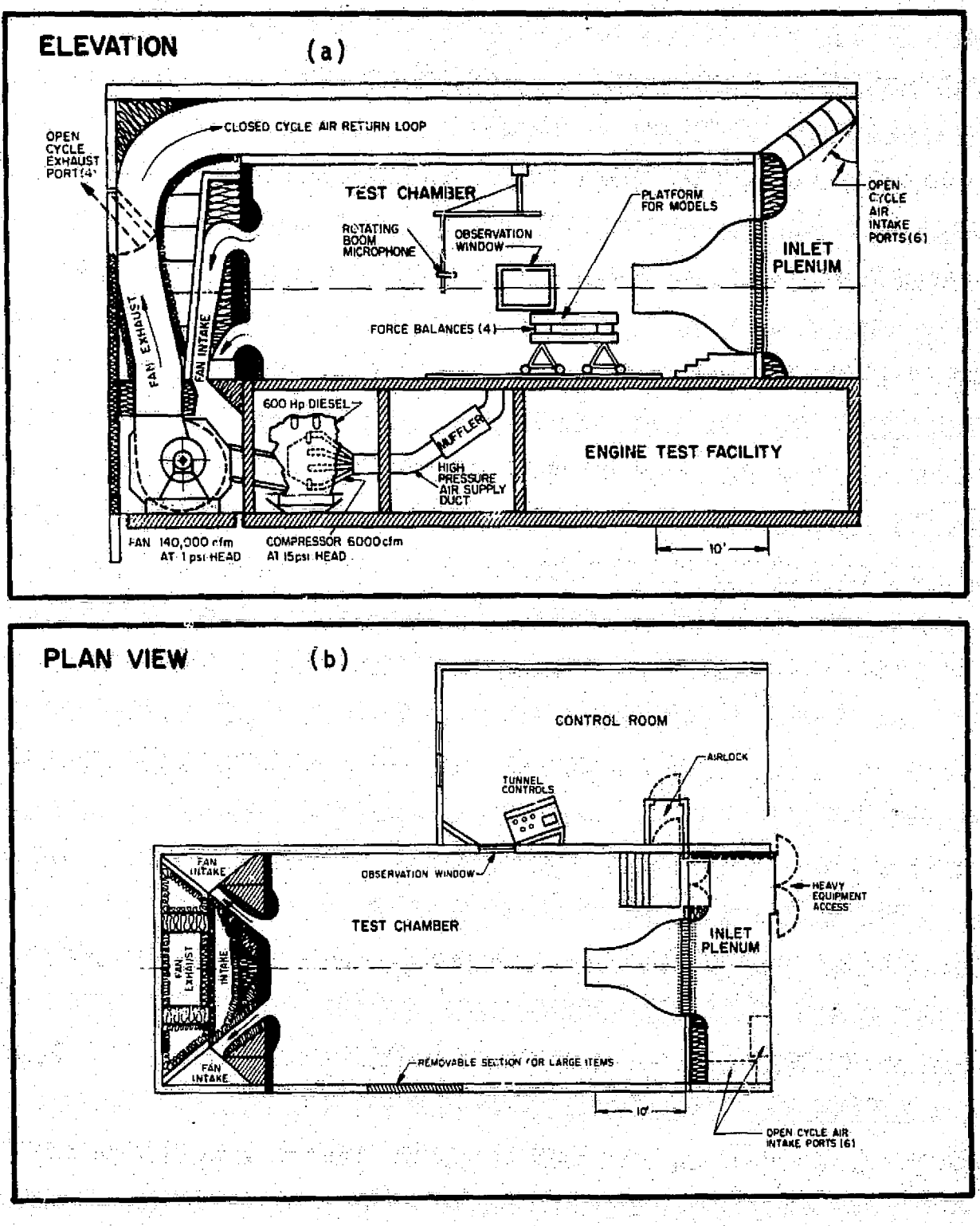

FIG. 3(a,b). BBN HIGH-SPEED FREE-JET ACOUSTIC WIND TUNNEL.

Dimensions are in cm (in)

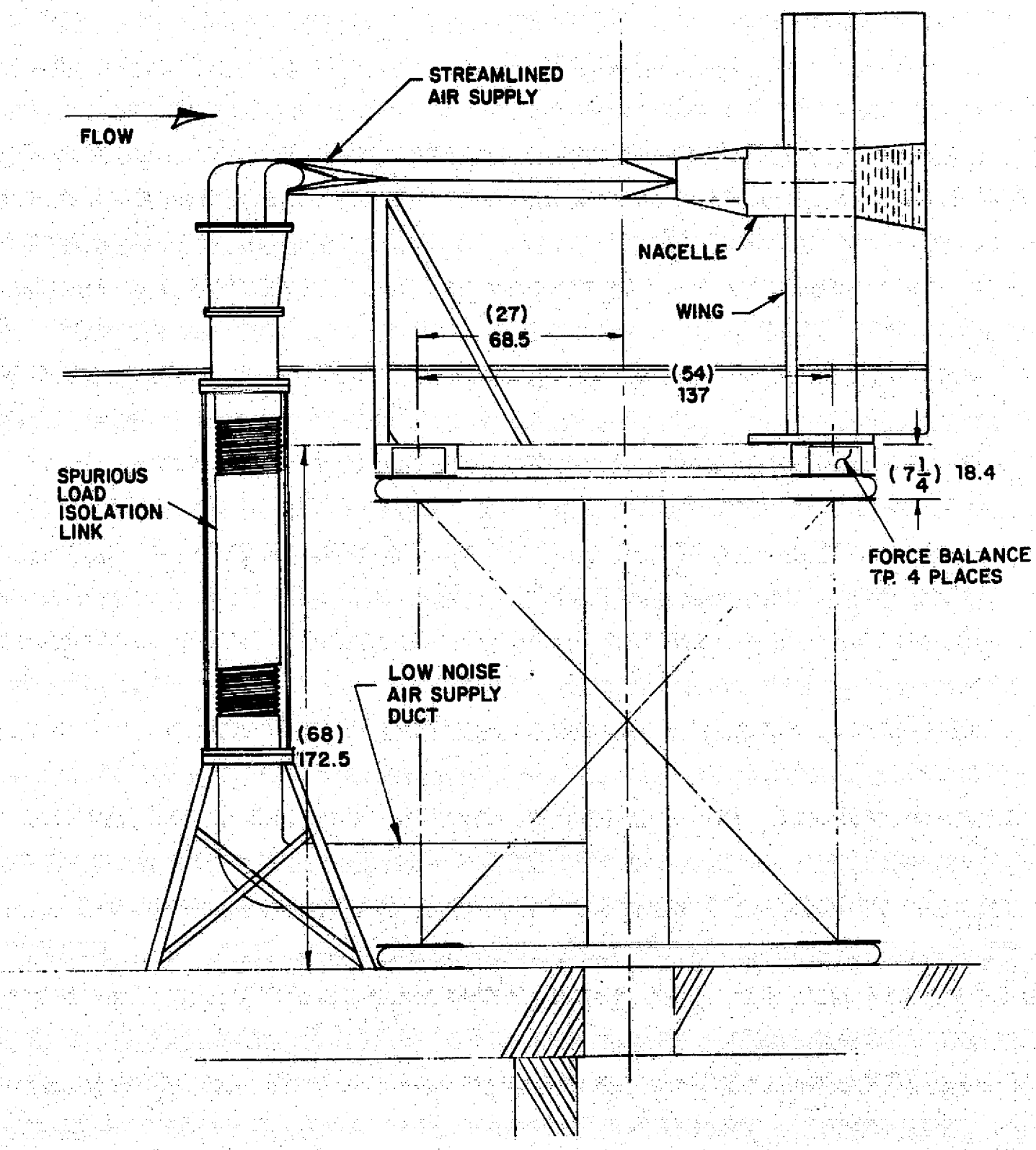

FIG. 4(a). SIDE VIEW OF EXPERIMENTAL ARRANGEMENT.

Dimensions are in cm (in)

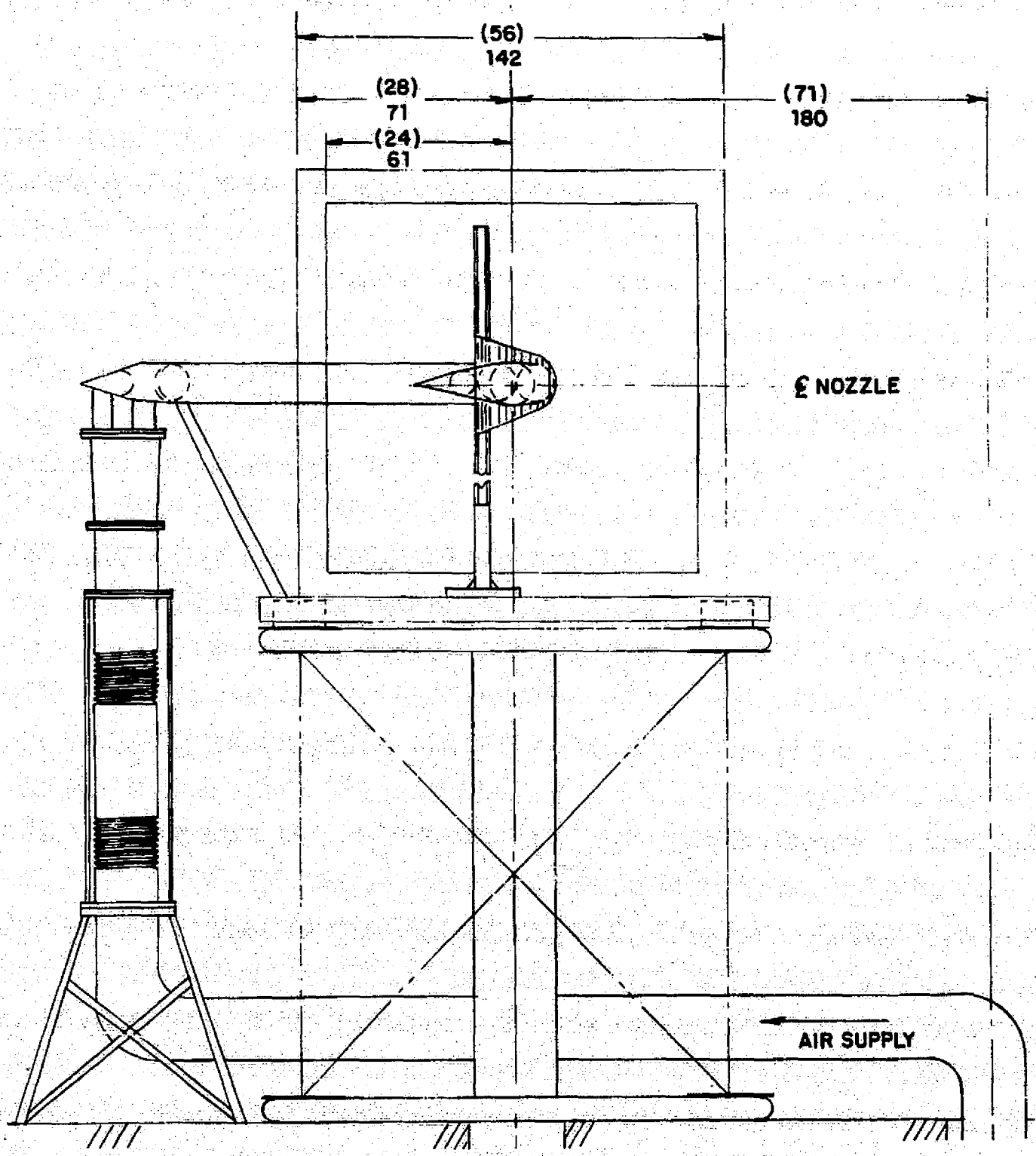

FIG. 4(b). END VIEW OF EXPERIMENTAL ARRANGEMENT.

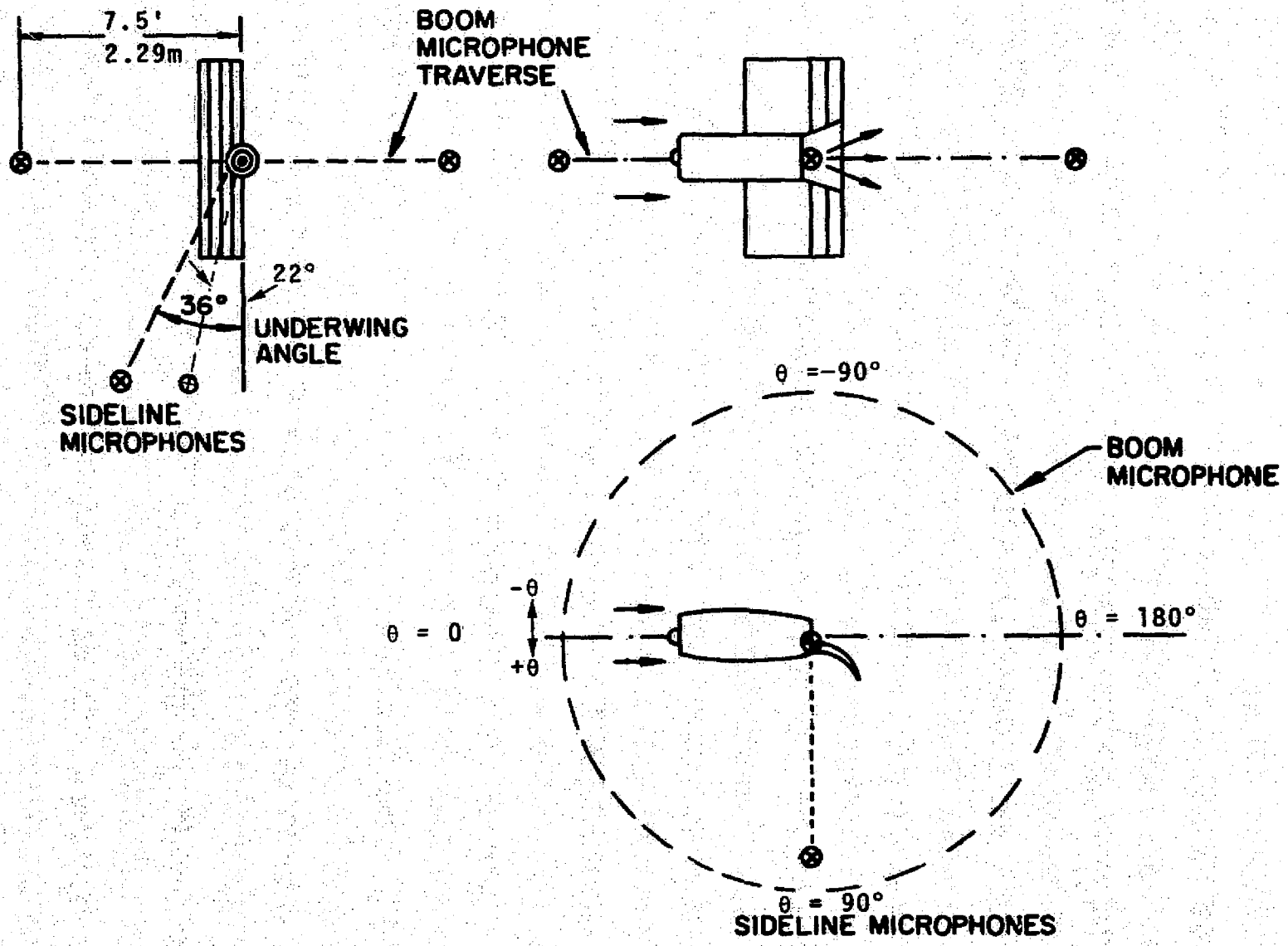

FIG. 5. SIDELINE AND BOOM MICROPHONE ARRANGEMENT.

TABLE 2. SUMMARY OF TEST RUNS.

USB Configuration	Nozzle Flap Angle δ_N	Mechanical Flap Angle δ_F	Nozzle Flow Velocity m/s (fps)	Microphone Measuring Points
7-Slot Nozzle	40° 60° 90°	40° 60° 60°	122, 152, 192 (400, 500, 630)	Every 30° in the flyover plane. 22° Sideline Location
Split Flow Nozzle	40° 60° 90°	40° 60° 60°	122, 152 (400, 500)	
14-Slot Nozzle [1]	40° 60° 90°	40° 60° 60°	122, 152, 192 (400, 500, 630)	36° Sideline Location
Coanda Flap [1]	60°	60°	122, 152, 192 (400, 500, 600)	Every 30° in the flyover plane. 36° Sideline Location

3. SUMMARY OF ACOUSTIC CHARACTERISTICS

3.1 General Remarks

The results of the model acoustic tests were scaled to four 26,800 N (6000 lb) thrust engines mounted on a wing. Engine jet velocity was assumed to be 244 m/s (800 fps), which corresponds to a pressure ratio of 1.35. No corrections were introduced to account for the elevated temperatures of a real engine.

The scaling factor was determined by the thrust requirements and since the reference thrust (see Section 4, Aerodynamics) for the various concepts varied, the scaling factor is not the same for all configurations. A detailed discussion of the scaling procedure is attached in Appendix A.

It was found that the acoustic data from all tested configurations scale as the velocity to the fifth power (U^5_{jet}). This result is an empirical one, and was decided upon by trial. While U^6_{jet} dependence yields reasonable results as well, the spectra peaks seem to diverge less when fifth power law is used.

Figures 6(a,b,c,d), 7(a,b,c,d) and 8(a,b,c,d) compare the acoustic performance of the 7-slot nozzle, 14-slot nozzle and split-flow nozzle at four points in the flyover plane for each of the nozzle flap angles tested. In the 60° nozzle flap angle data, the performance of a regular Coanda USB device [1] was added.

The patterns that emerge from the above figures indicate that the slotted nozzles, in their various configuration, affords one control over the relative contribution of the low and the high frequencies to the sound spectrum generated by the propulsive lift device.

Most spectra are characterized by two peaks: a low frequency peak, which is almost always at 200 Hz for the full scale USB device (630 Hz for the model) and a high frequency peak, which varies from 1600 Hz to 8000 Hz.

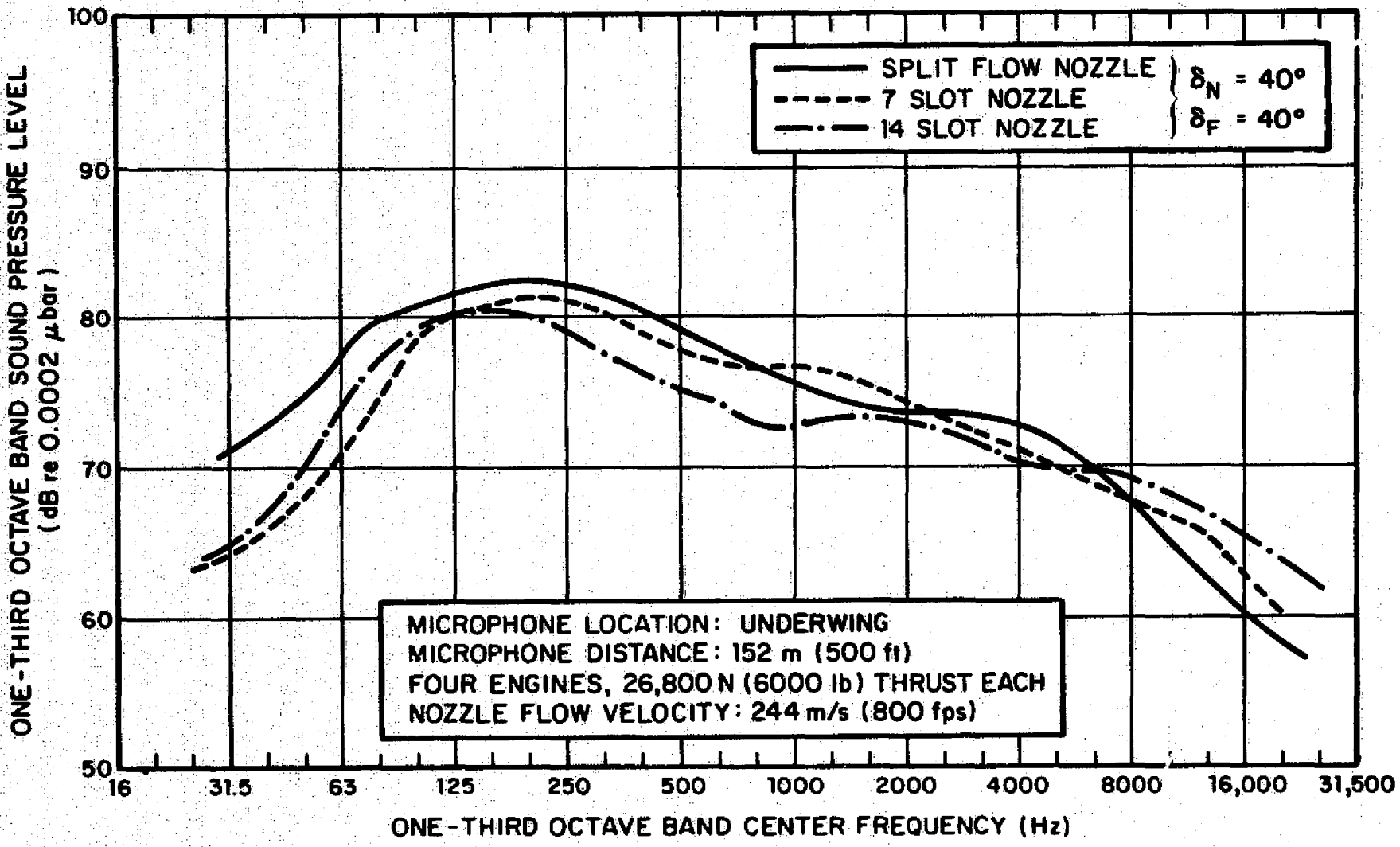

FIG. 6(a). COMPARISON OF NOISE FROM USB DEVICES.

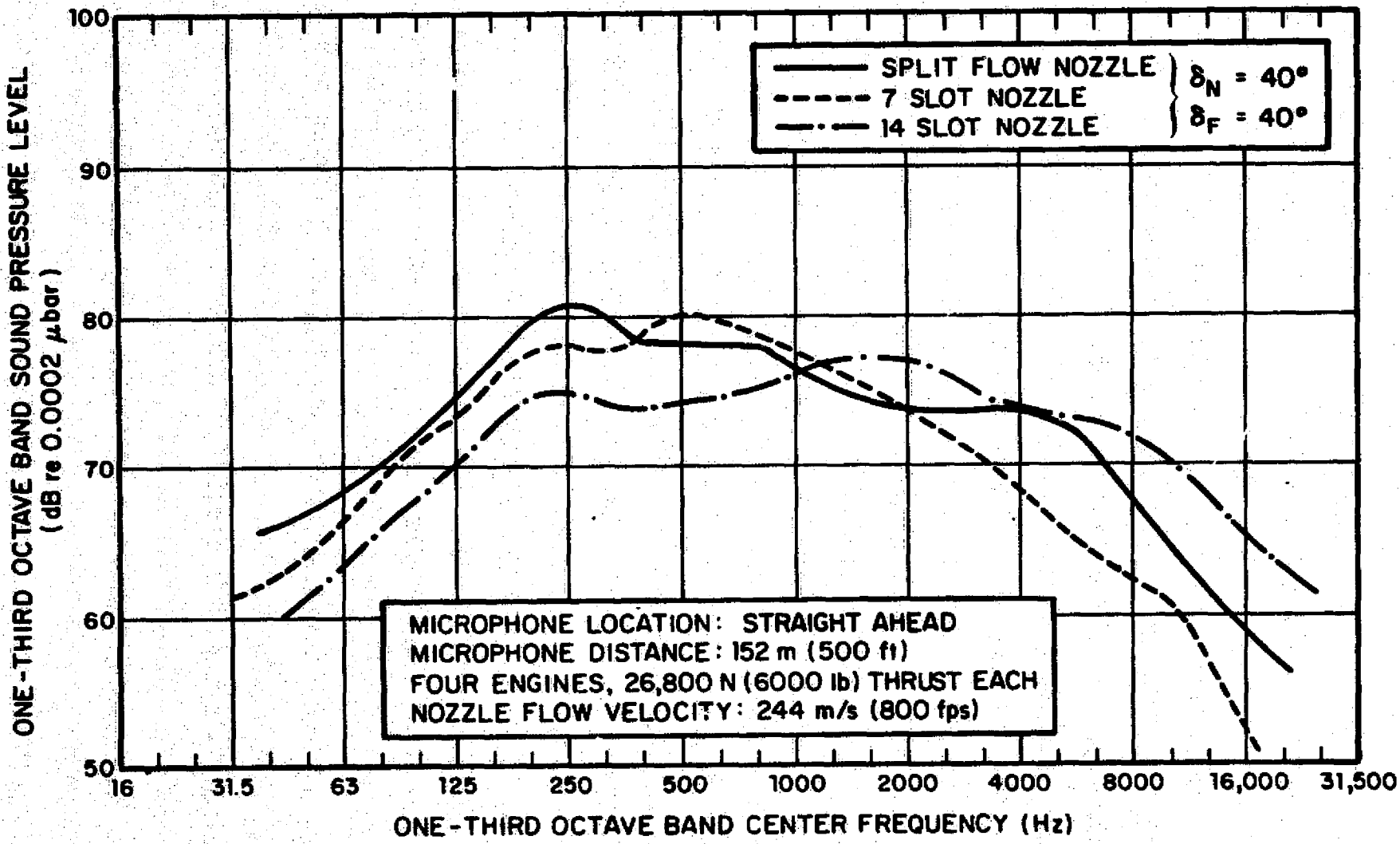

FIG. 6(b). Continued

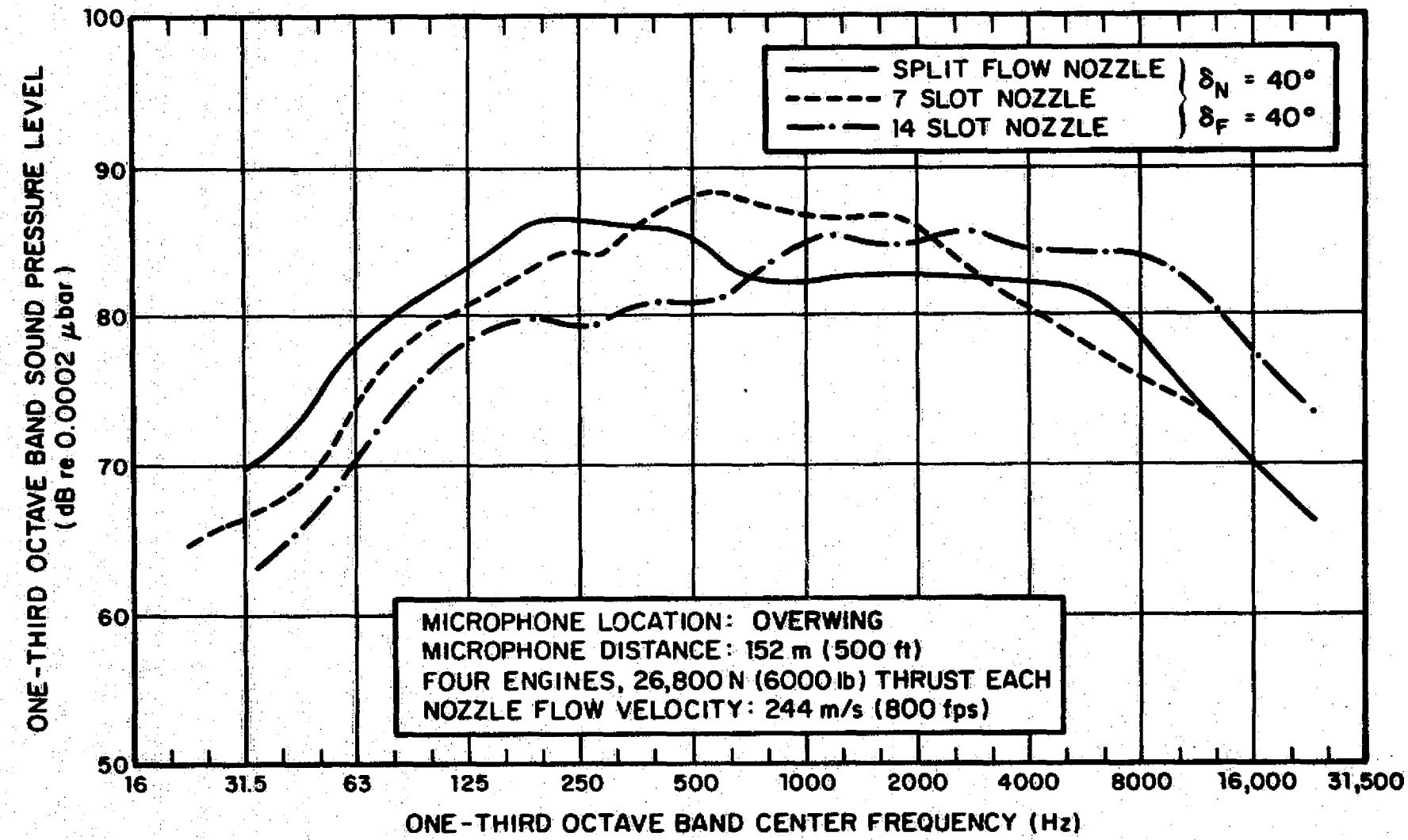

FIG. 6(c). Continued

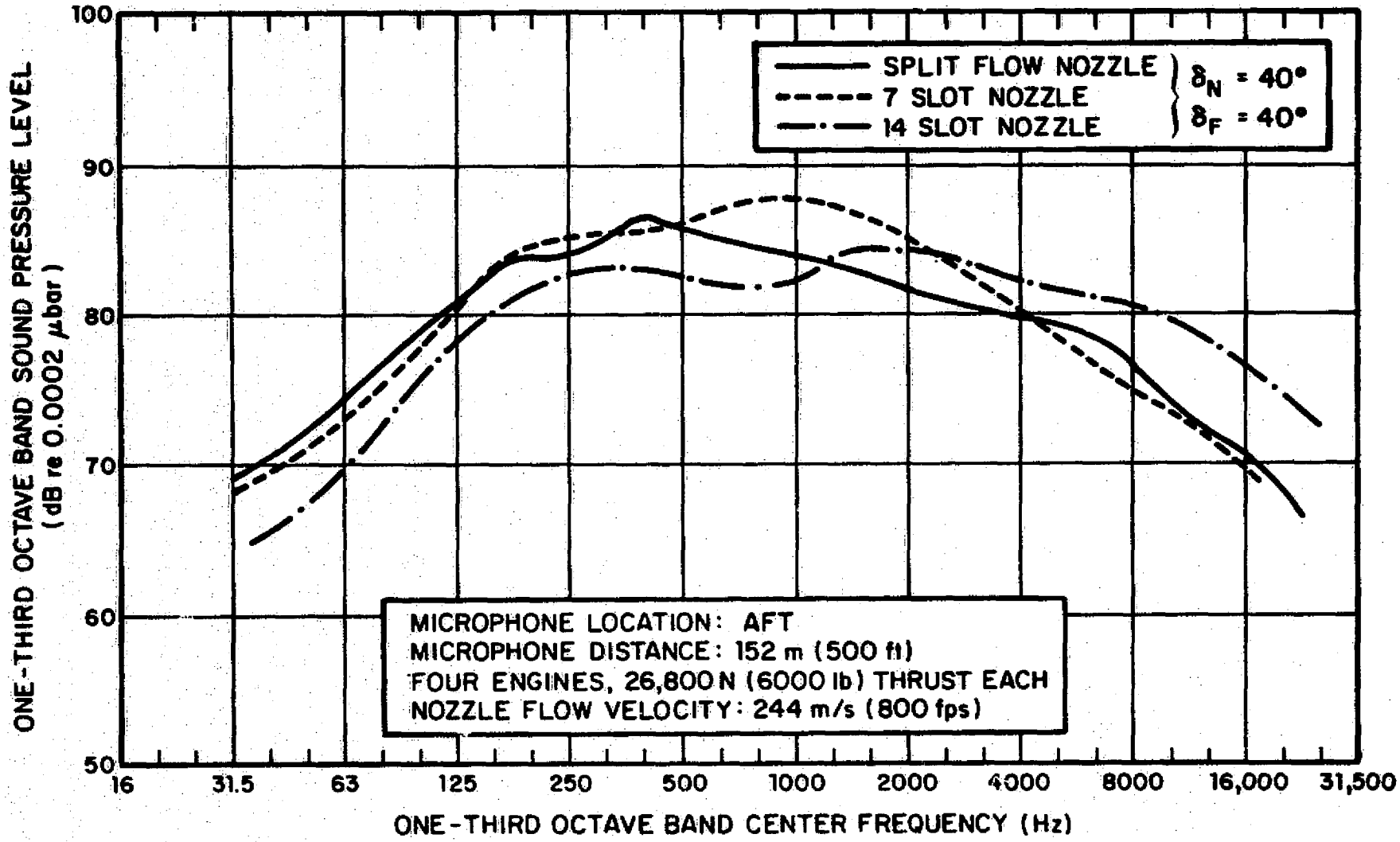

FIG. 6(d). Continued

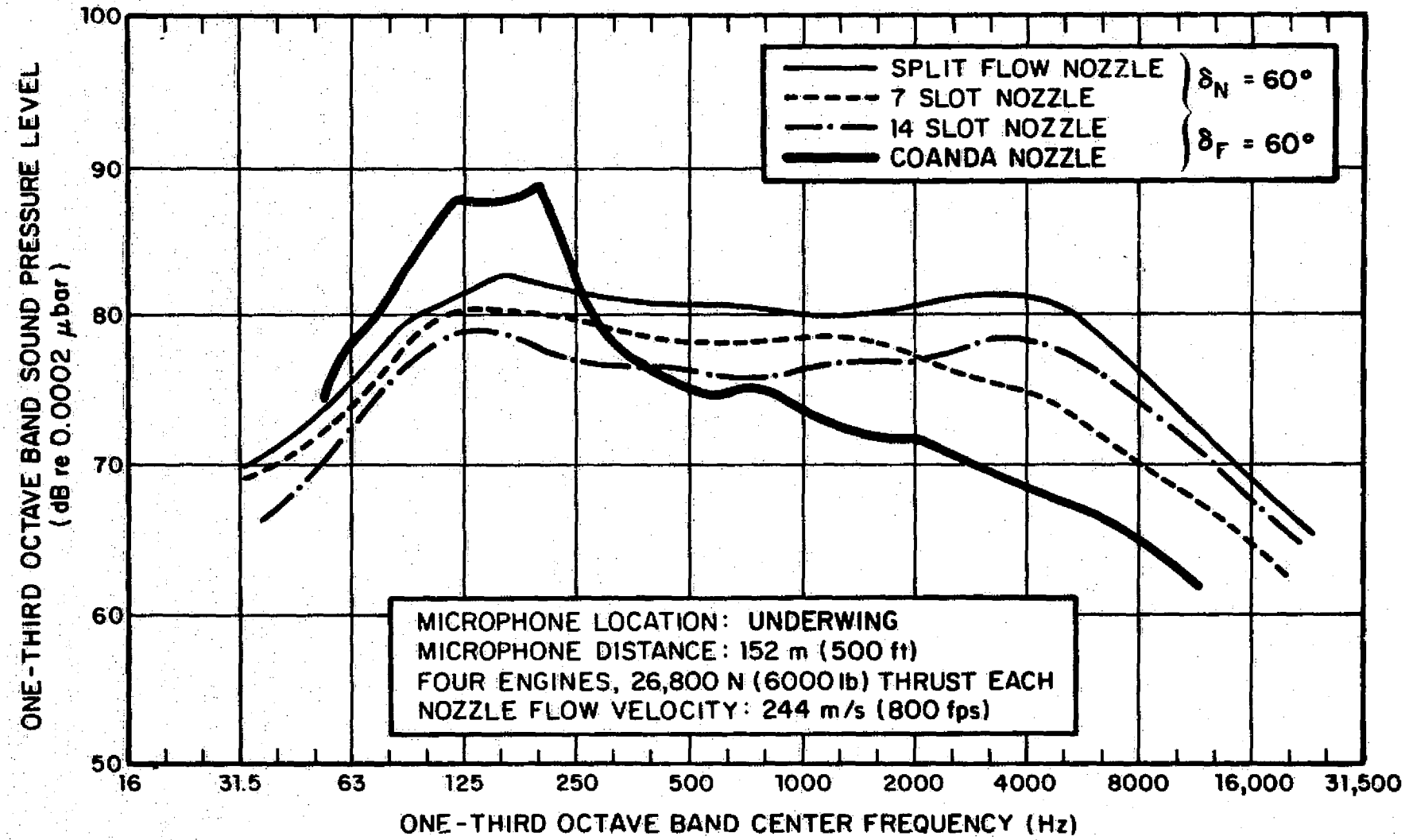

FIG. 7(a). COMPARISON OF NOISE FROM USB DEVICES.

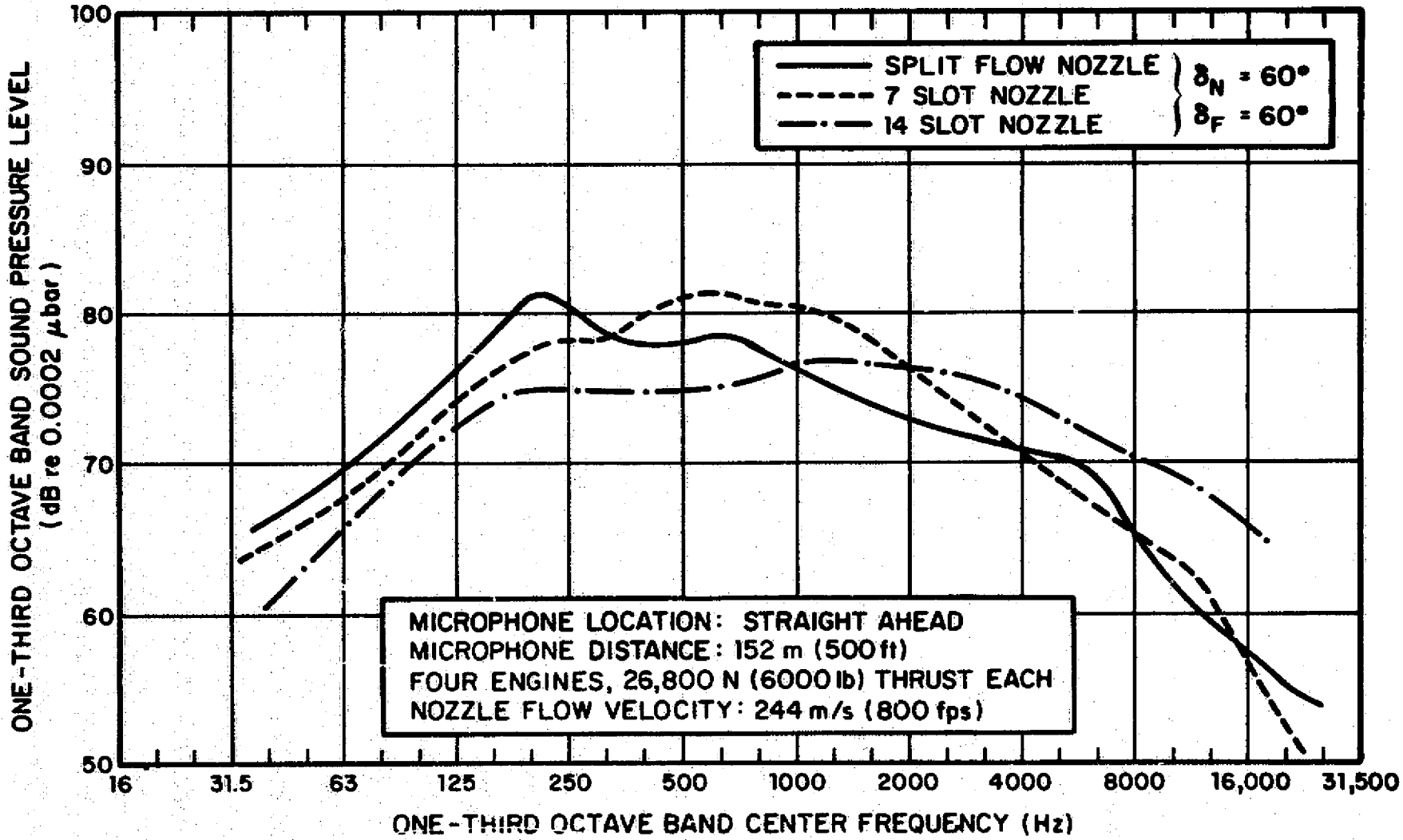

FIG. 7(b). Continued

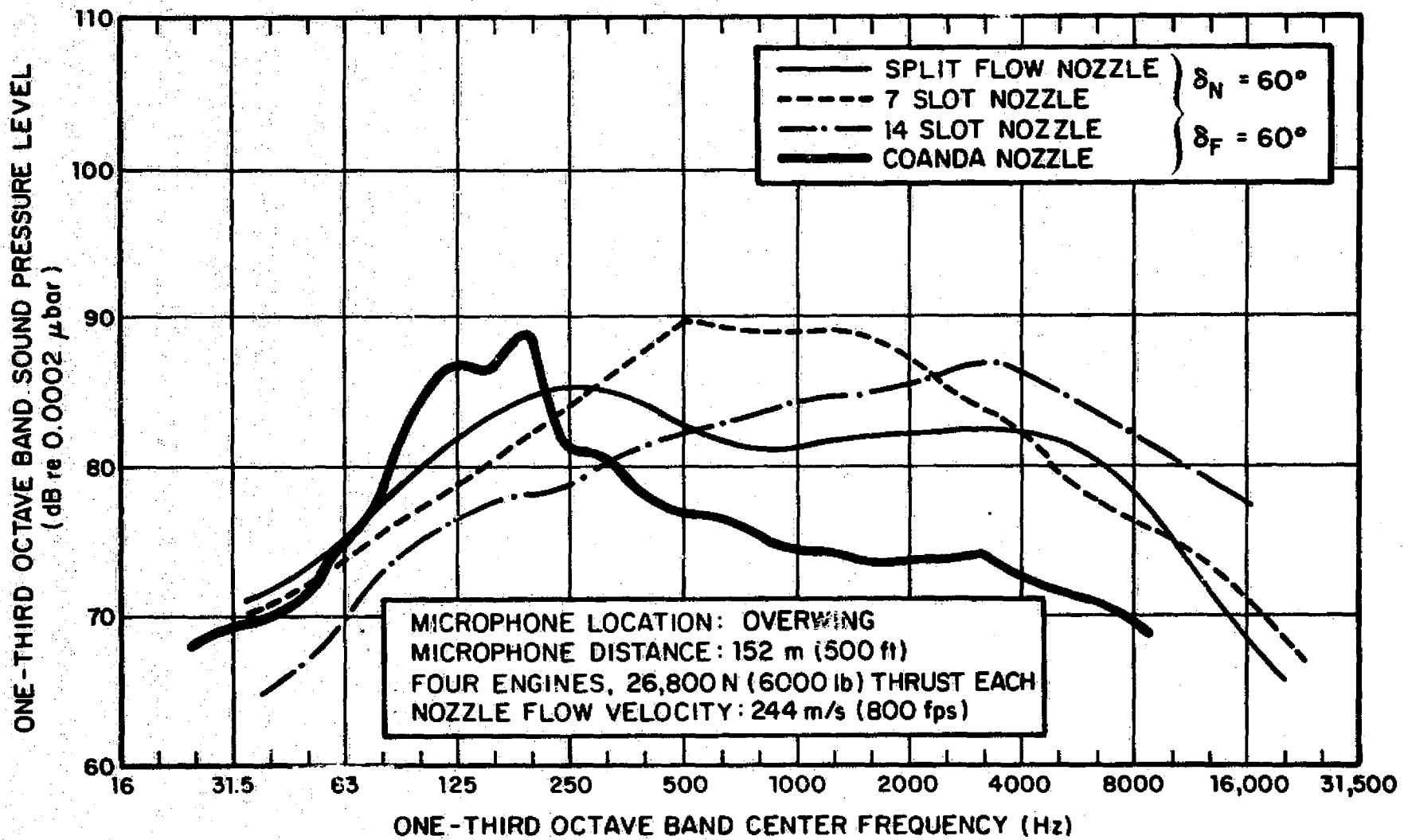

FIG. 7(c). Continued

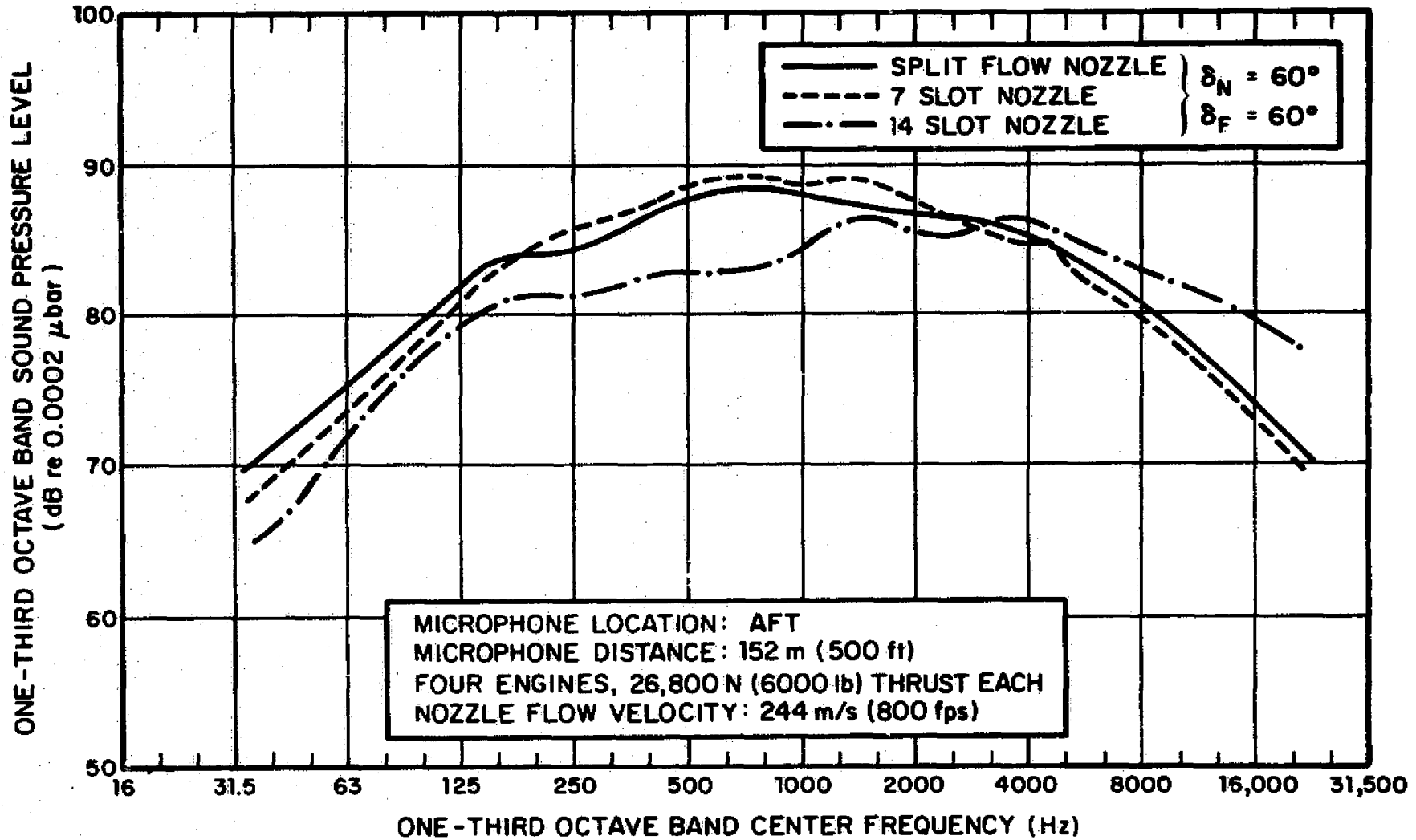

FIG. 7(d). Continued

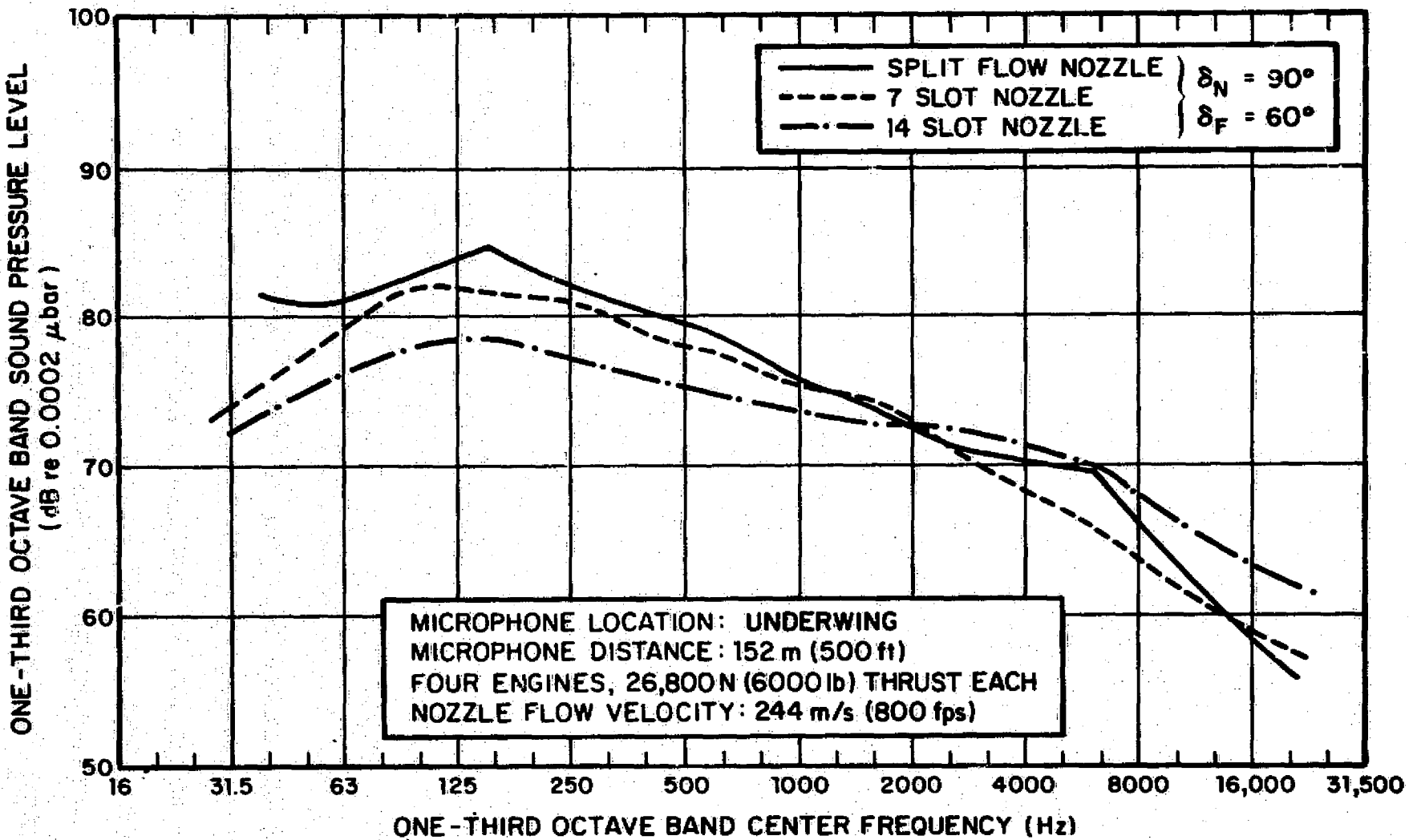

FIG. 8(a). COMPARISON OF NOISE FROM USB DEVICES.

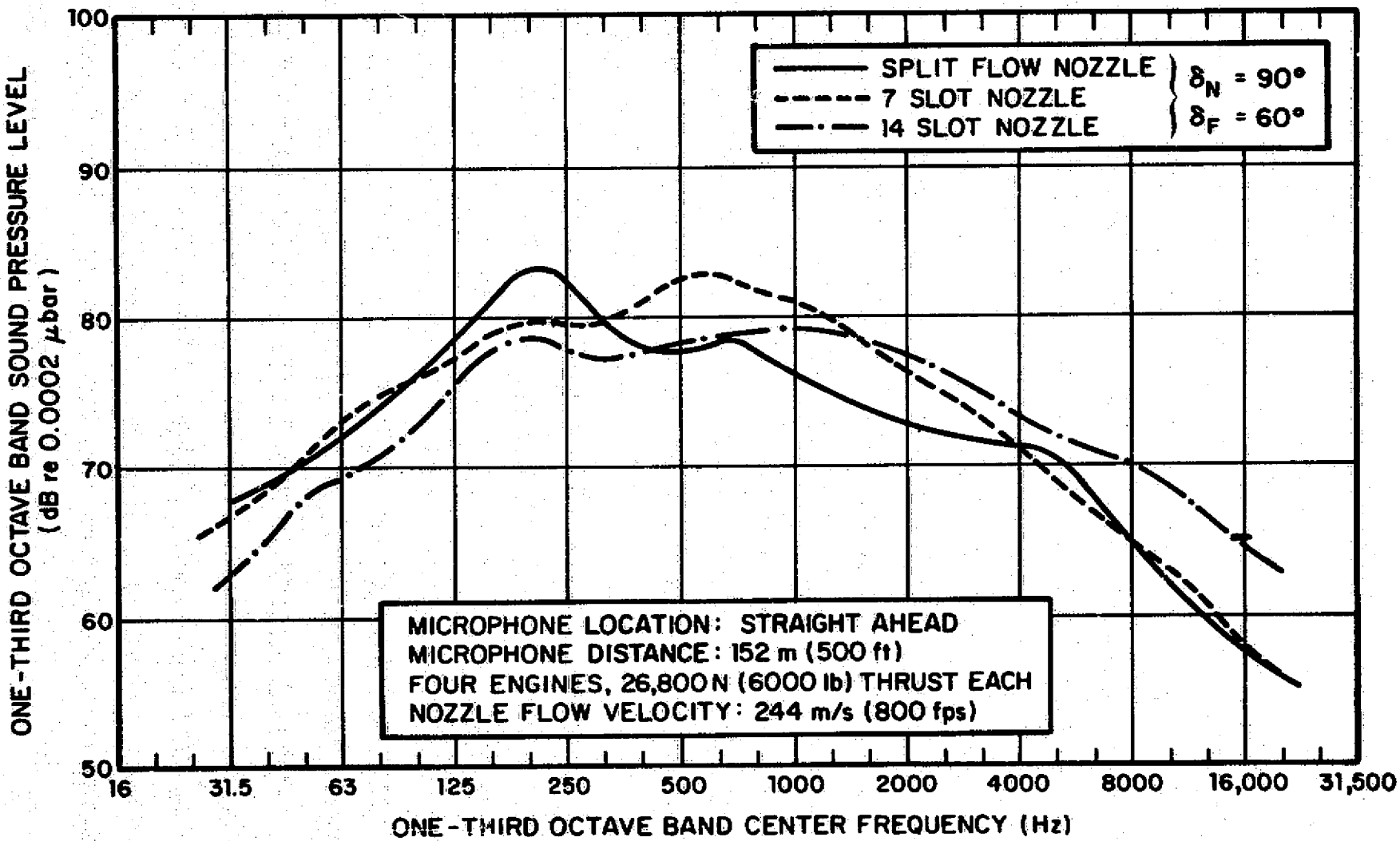

FIG. 8(b). Continued

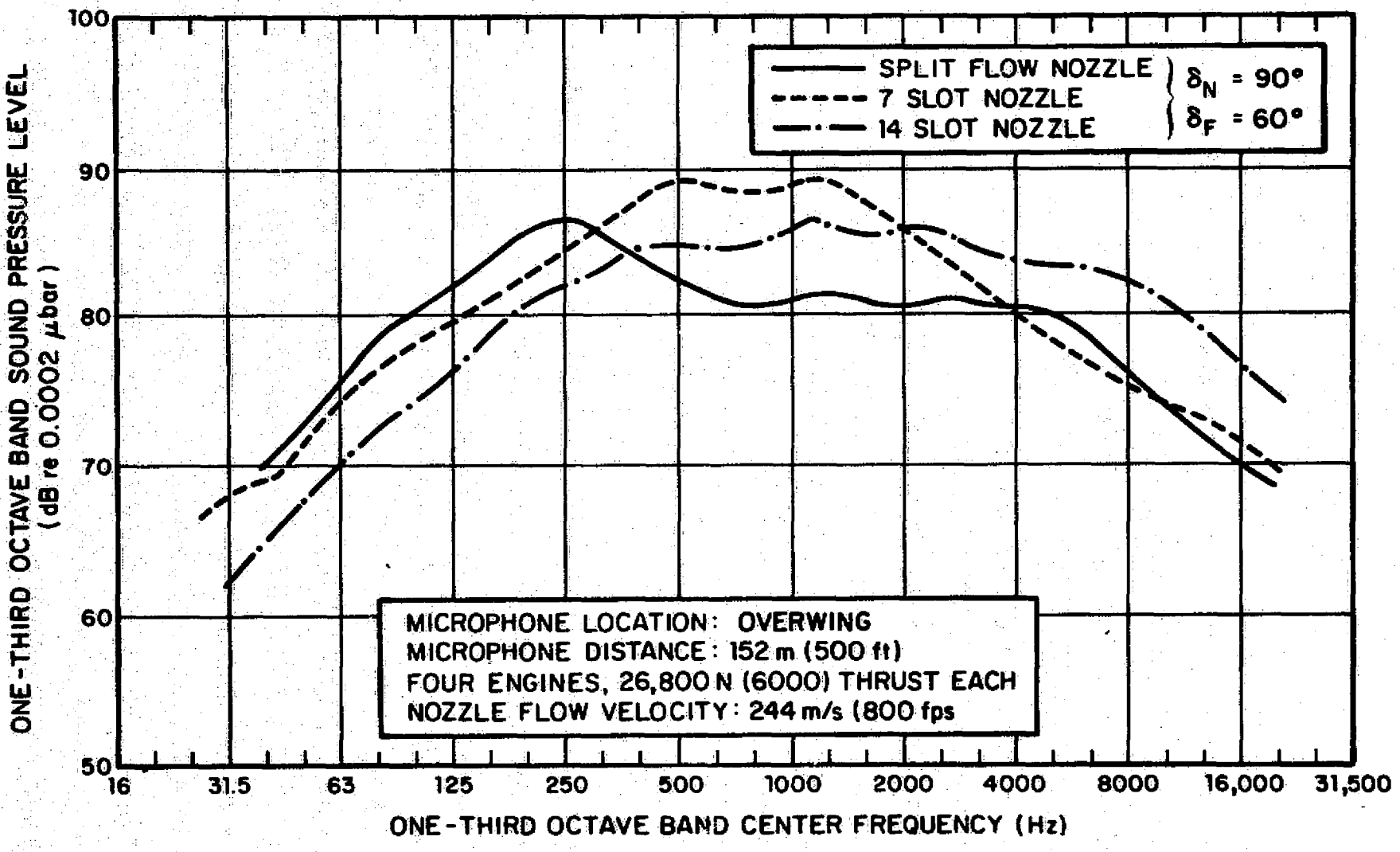

FIG. 8(c). Continued

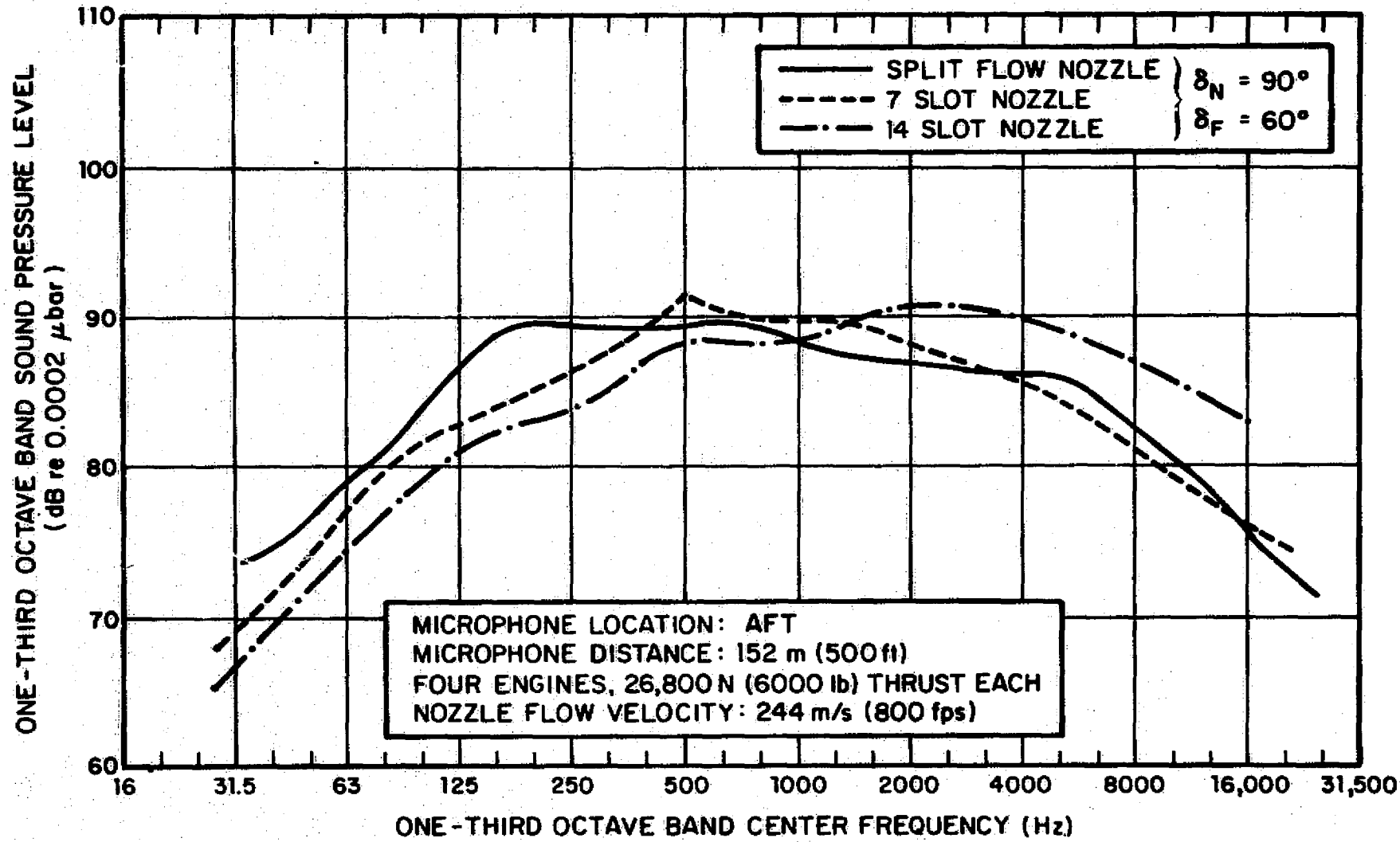

FIG. 8(d). Continued

The regularity of the low frequency peak suggests that this area of the sound spectrum is dominated by a source whose size is of the same order as the Nacelle or the propulsive lift device as a whole. The details of the particular nozzles affect the level of the low frequency peak but not its frequency. As will be shown later, there is some reason to assume that this low frequency peak is due to a monopole, rather than a dipole sound source.

The high frequency peak, which is not as regular in frequency as the low frequency one, is sensitive to the details of the USB device. Since the wavelengths at the higher frequencies are smaller than the wing chord, shielding effects are much more pronounced and the dipole directivity pattern is more evident. The directivity of the USB devices is presented in a section below, where the above arguments will be amplified upon.

It should be noted that the presence of these two peaks and the fact that they may be caused by different sources is significant when it is realized that the main problem associated with the 200 Hz peak is internal cabin noise while the high frequency peak creates a community noise problem.

3.2 Directivity Patterns

Figures 9(a,b), 10(a,b), and 11(a,b) show the directivity patterns for the tested devices. For comparison, previously [*1*] acquired data for the 60° Coanda flap were added to Fig. 10. It was found that the presentation of the directivity patterns of the two peaks alluded to above is much more instructive for diagnostic purposes than some overall measure of the nozzle performance. Part (a) of each of the above figures show the directivity pattern of the low frequency peak (200 Hz), part (b) is that of the high frequency (around 2000 Hz). The low frequency

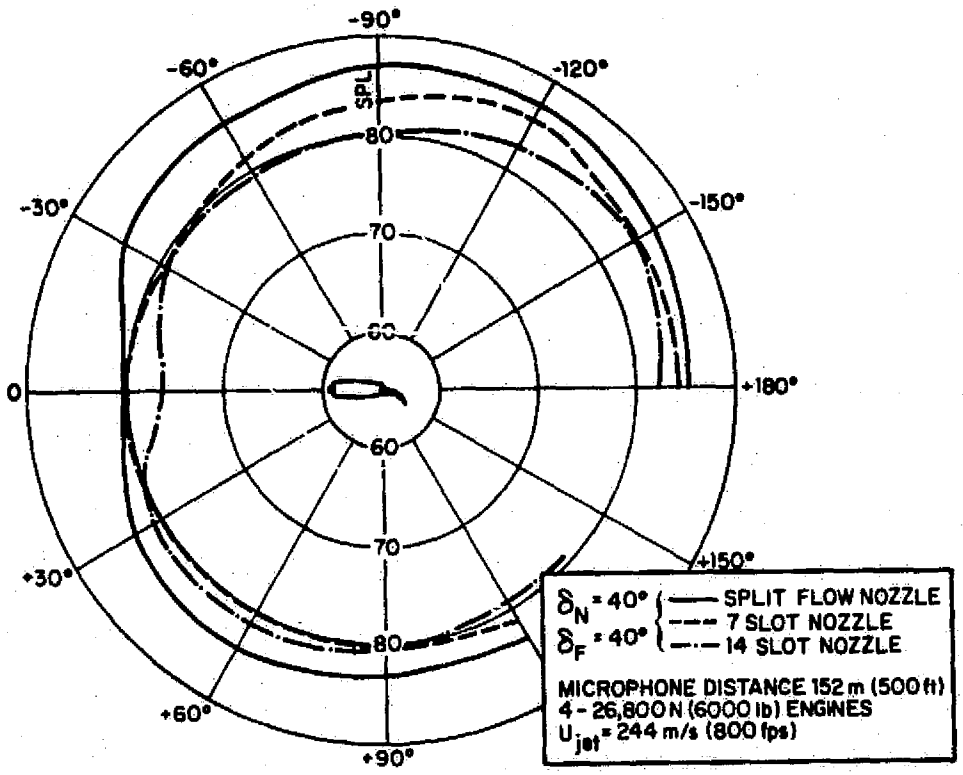

FIG. 9(a). FLYOVER PLANE LOW FREQUENCY (200 Hz) DIRECTIVITY PATTERN.

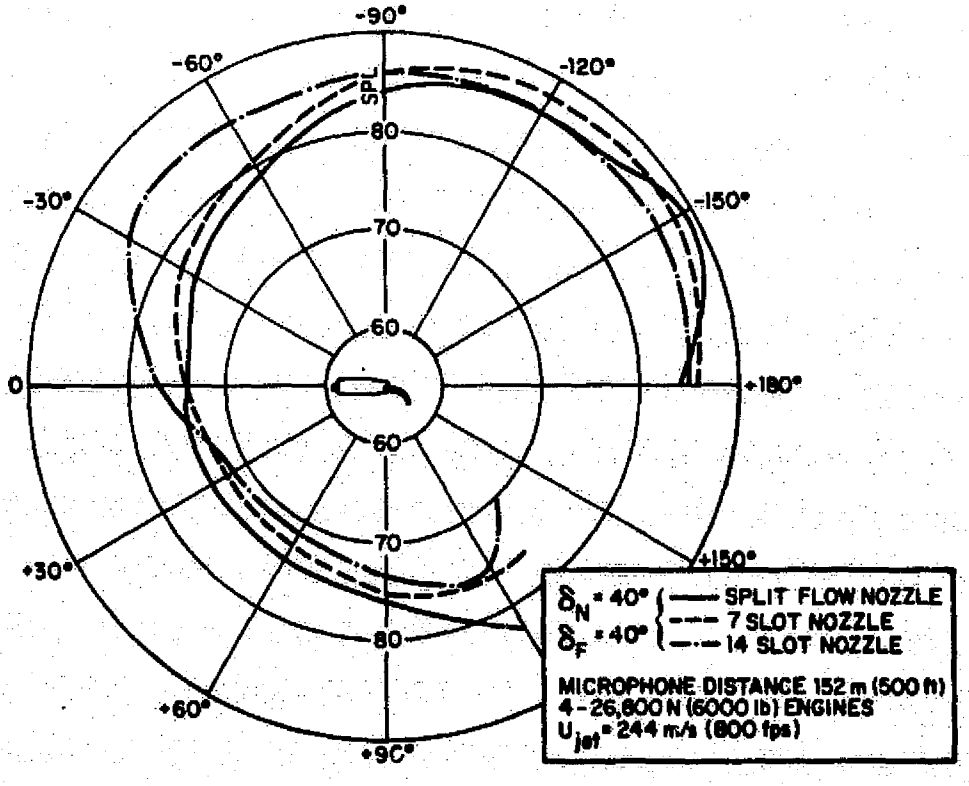

FIG. 9(b). FLYOVER PLANE HIGH FREQUENCY (2000 Hz) DIRECTIVITY PATTERN.

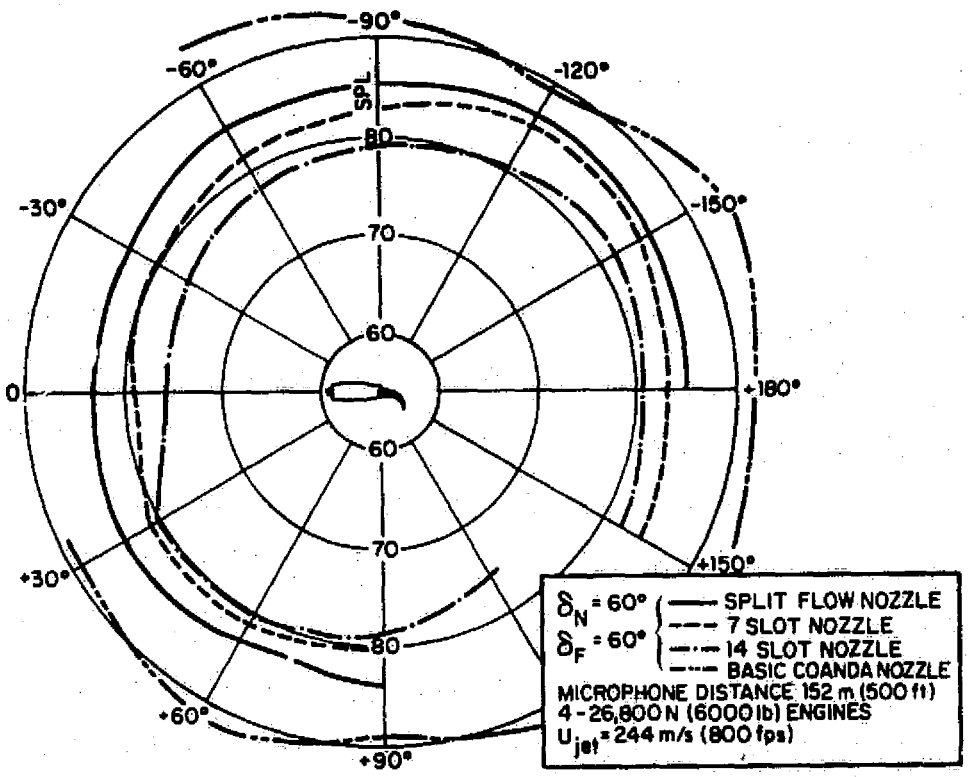

FIG. 10(a). FLYOVER PLANE LOW FREQUENCY (200 Hz) DIRECTIVITY PATTERN.

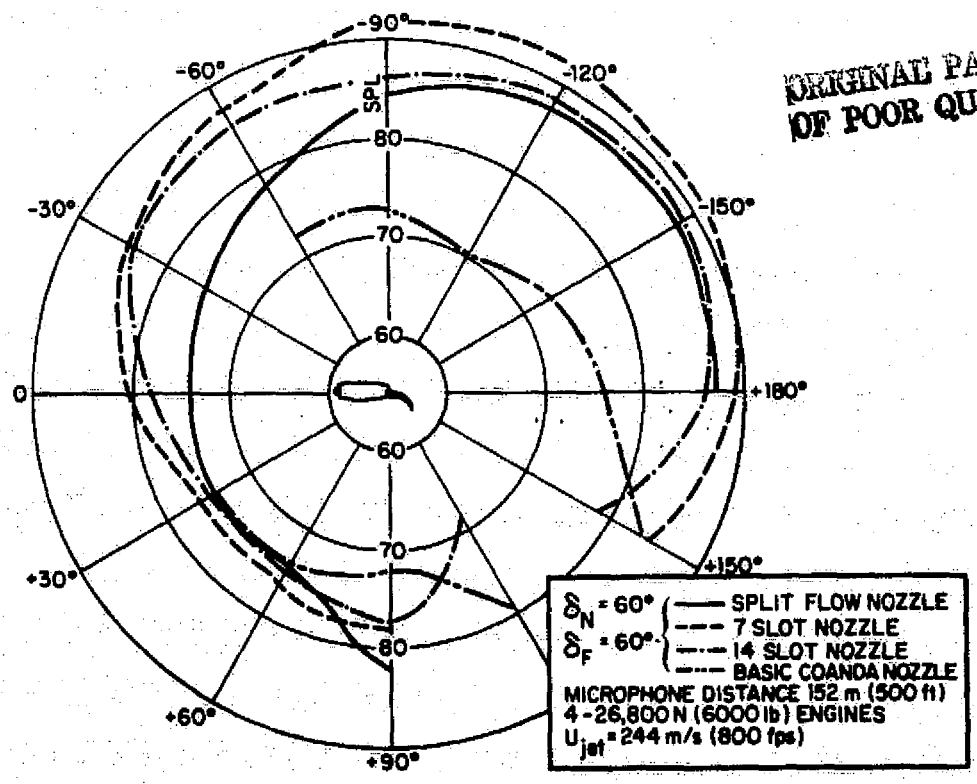

FIG. 10(b). FLYOVER PLANE HIGH FREQUENCY (2000 Hz) DIRECTIVITY PATTERN.

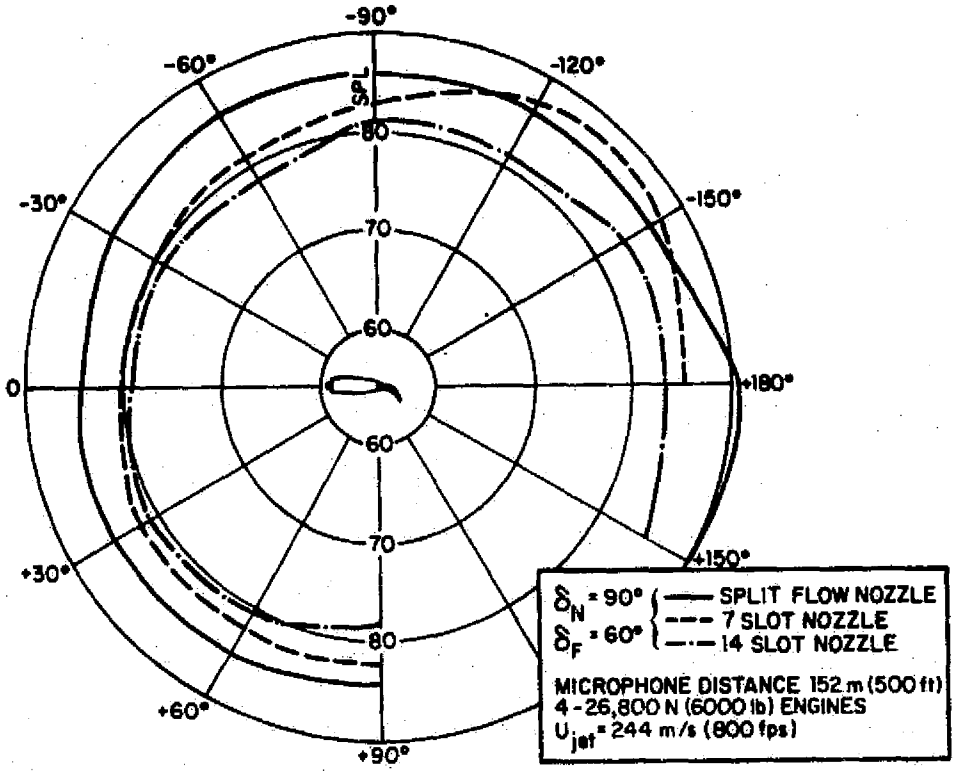

FIG. 11(a). FLYOVER PLANE LOW FREQUENCY (200 Hz) DIRECTIVITY PATTERN.

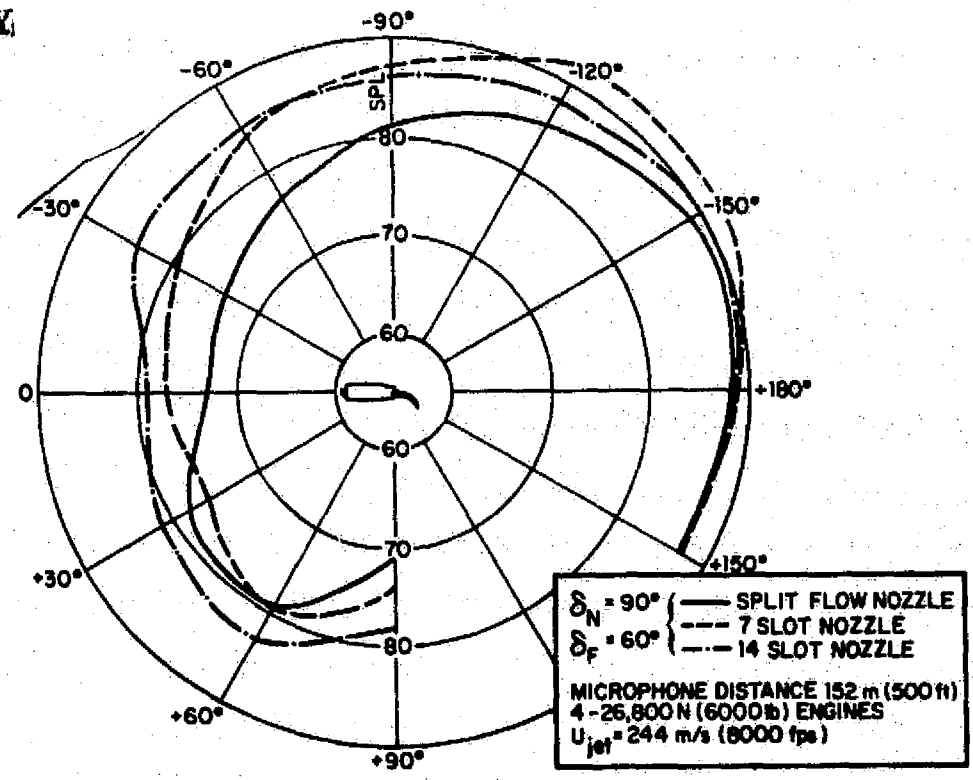

FIG. 11(b). FLYOVER PLANE HIGH FREQUENCY (2000 Hz) DIRECTIVITY PATTERN.

directivity patterns reveal that the 200 Hz third-octave band level is essentially omnidirectional for all USB devices tested. The level of this band depends on the magnitude of the aspect ratio of the largest slot in each of the devices with the Coanda nozzle (Fig. 10a) being the noisiest, followed by the split flow nozzle, then the 7-slot nozzle, with the 14-slot nozzle being the quietest. Acoustic tests of the Nacelle noise only (no USB device attached) indicate that internal flow obstruction in the Nacelle itself may be responsible for the low frequency noise.

The high frequency patterns show the USB devices are ranked in the reverse order. As expected, the larger the number of slots the higher the level. There are strong indications that it is the articulating part of the nozzle which dominates the high frequency noise patterns. In Figs. 6 through 8 as well as in the directivity plots, the split flow nozzle, which is equipped with the turning flap of the 14-slot nozzle, exhibits high frequency levels approaching that of the 14-slot nozzle and exceeding the levels of the 7-slot nozzle. While the 7-slot nozzle exceeds the split-flow nozzle's noise levels at mid-frequencies.

It seems that the narrow slots on the fixed part of the 14-slot nozzle are the most effective in suppressing the low frequency noise while the generation of high frequency noise could be reduced, or shifted to even higher frequencies by modifications of the articulated nozzle-flap.

3.3 Takeoff and Landing Spectra

Figures 12(a,b,c) and 13(a,b,c) show the predicted noise spectra during takeoff and landing. Takeoff noise levels are predicted for the 152 m (500 ft) sideline (aircraft altitude 61 m or 200 ft) with all engines at full power (jet velocity 244 m/s).

The landing noise levels are predicted for the engines at half power (164 m/s) with the aircraft 133 m (370 ft) directly overhead. Atmospheric attenuation effects are included (standard day 15°C, 75% relative humidity) but no forward speed effects. The PNdB values that are presented in Table 1 were calculated from these spectra.

3.4 Potential for Further Noise Reduction

The relatively high levels of the high frequency noise produced by the slotted nozzles can be significantly reduced by modifying the individual flaps. Hayden *et al* [6] and Scharton *et al* [7] have shown, by correlating the fluctuating pressure on a blowing flap with the far field noise, that the high frequency noise is generated in a small area near the trailing edge of the flap. This area, which is confined to the aft quarter of the flap chord, is amenable to treatment. By employing porous trailing edges on an upper-surface-blown flap system, Hayden [8] has achieved noise reductions of 6 to 10 dB at the Strouhal peak with no deterioration of the aerodynamic performance. This type of treatment, when applied to the slotted nozzles, will reduce their high frequency noise to the same levels as those of the Coanda flaps while preserving their advantage in the low frequency part of the spectrum.

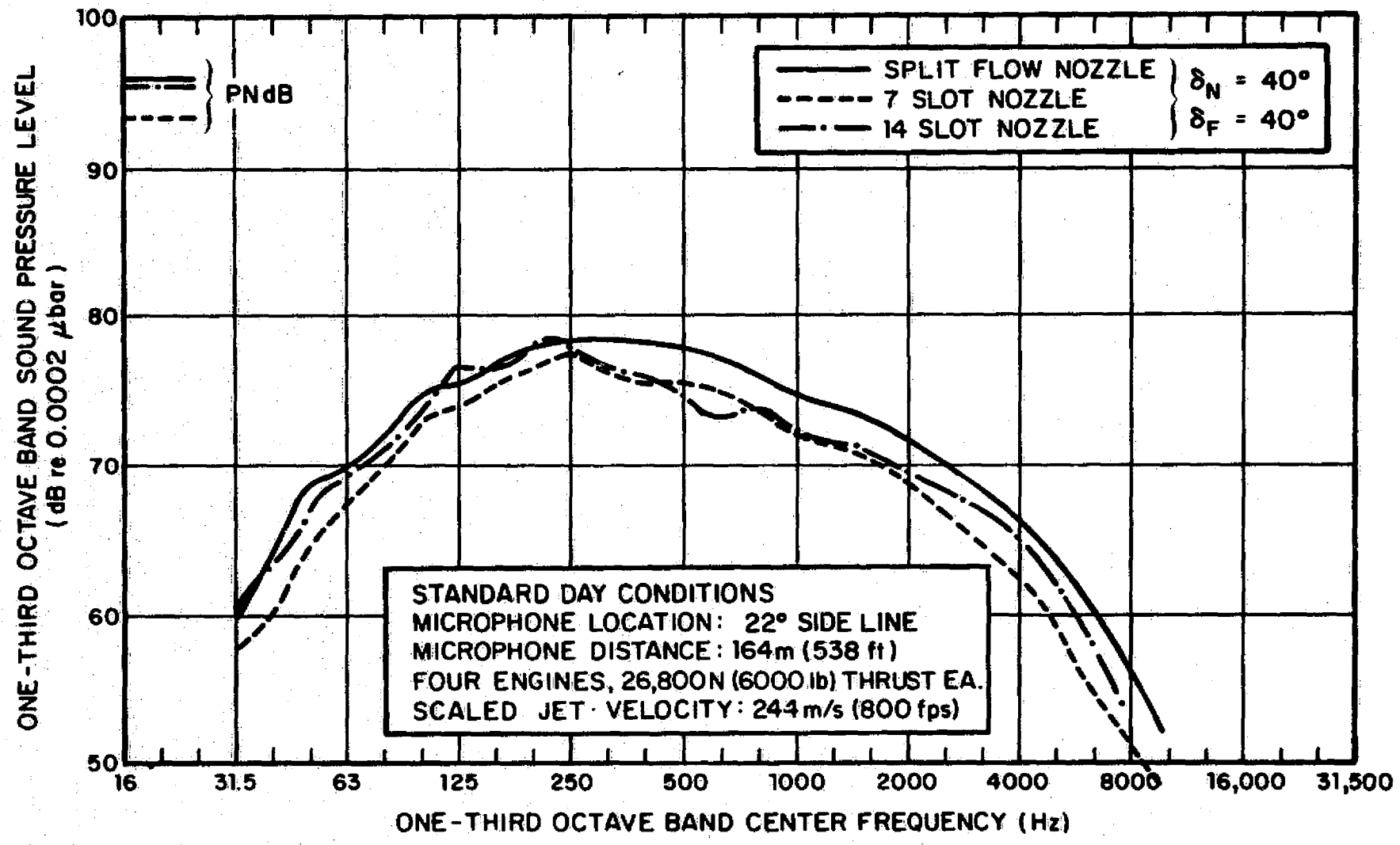

FIG. 12(a). COMPARISON OF NOISE FROM USB DEVICES - TAKEOFF.

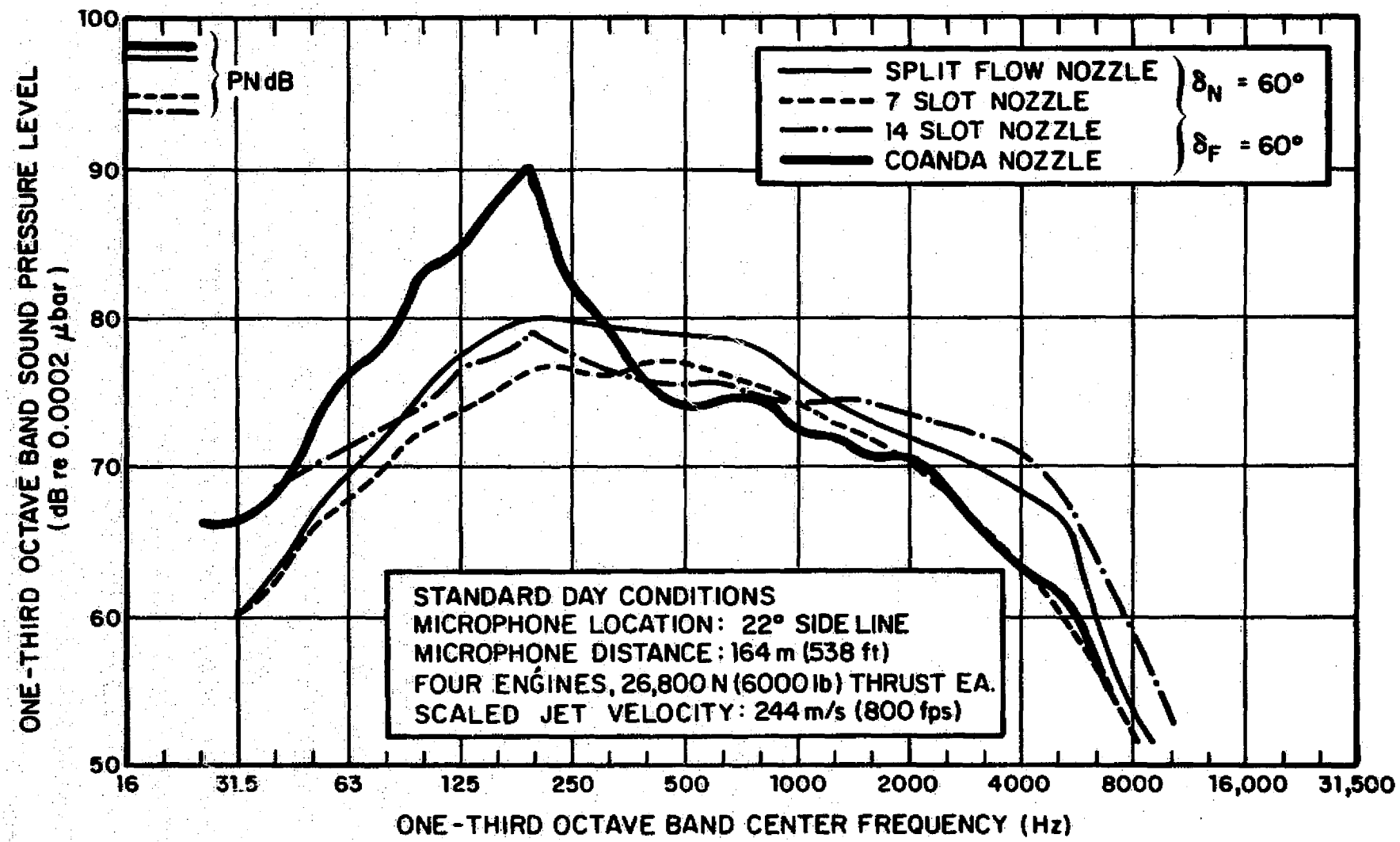

FIG. 12(b). Continued

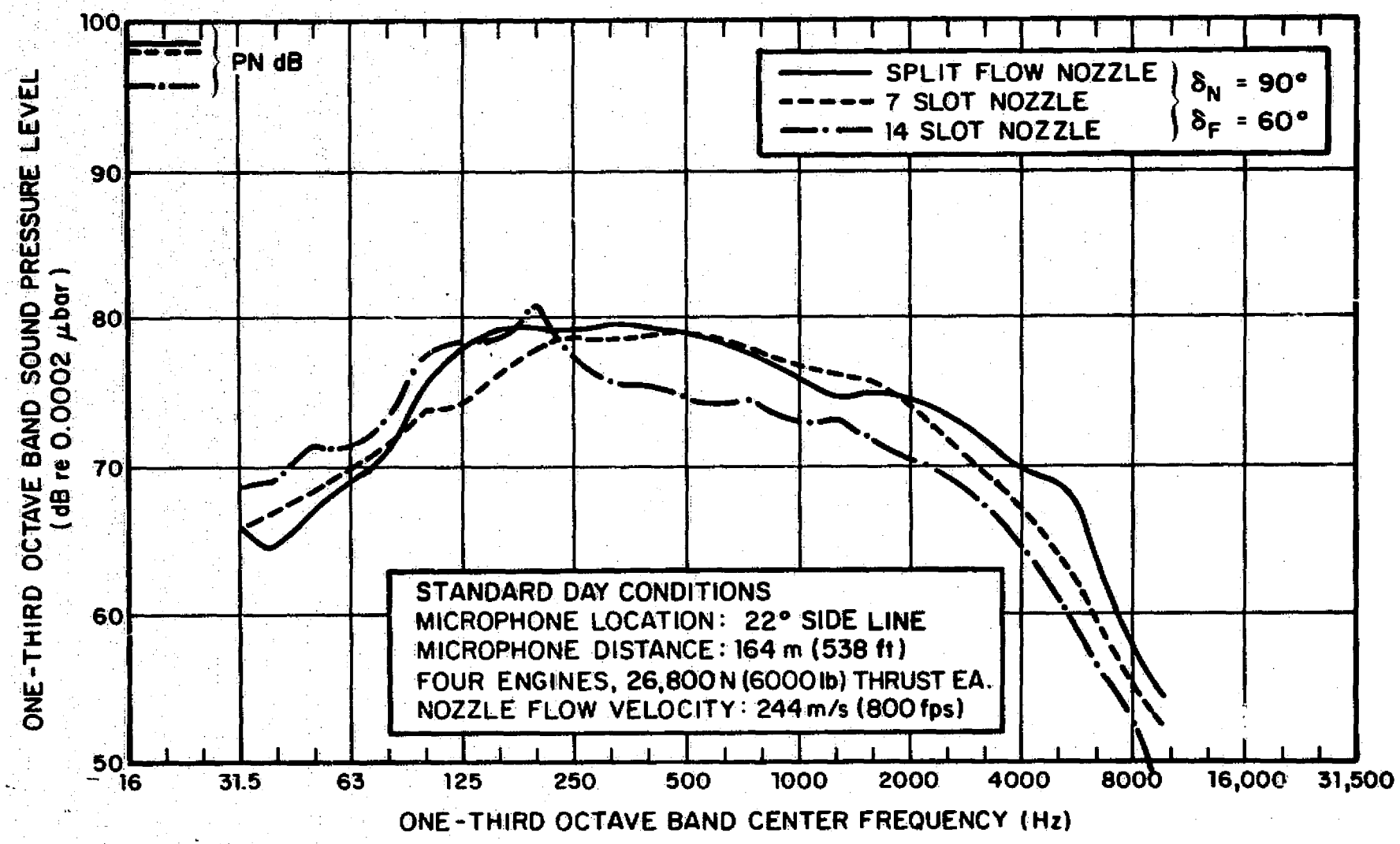

FIG. 12(c). Continued

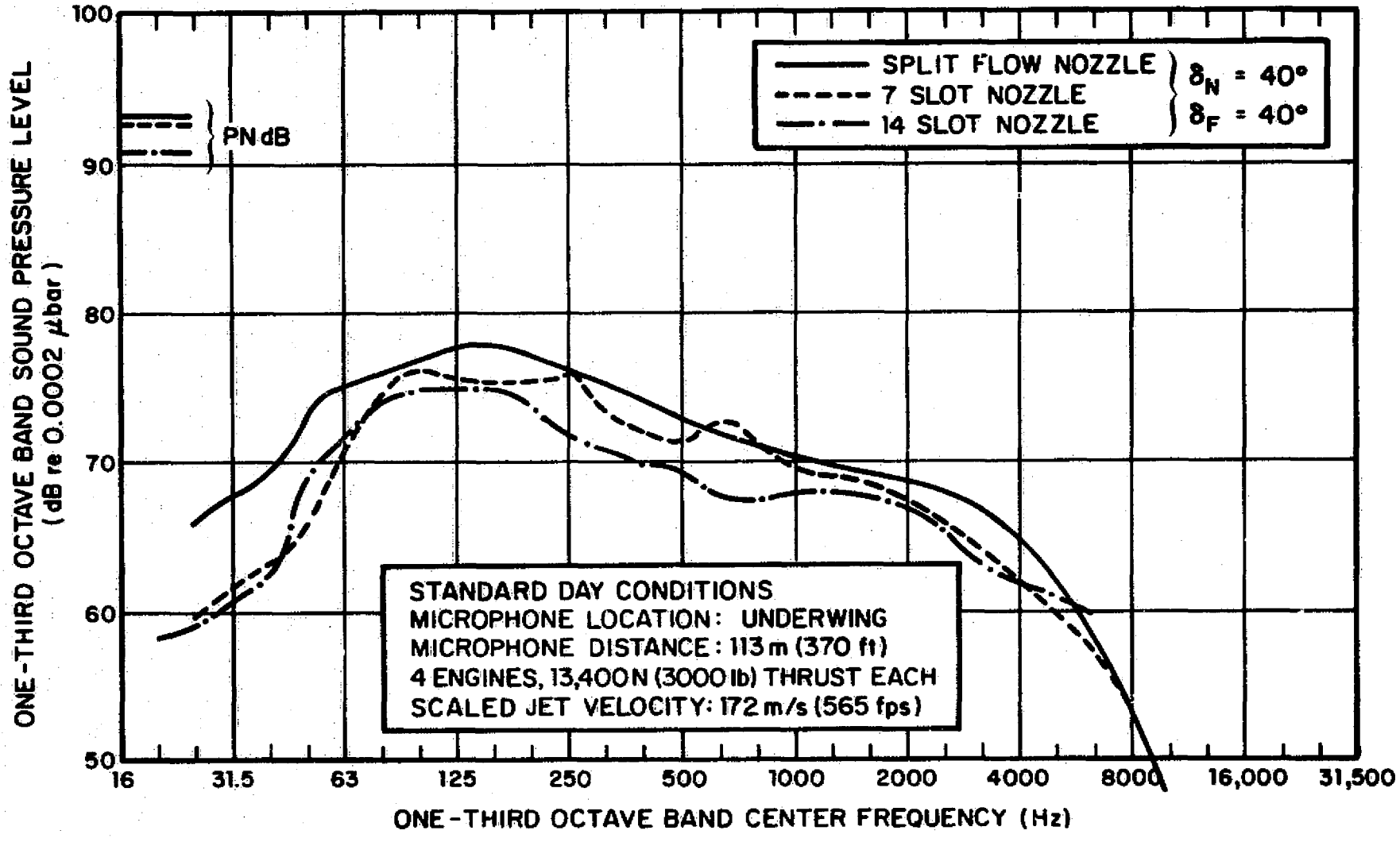

FIG. 13(a). COMPARISON OF NOISE FROM USB DEVICES - LANDING.

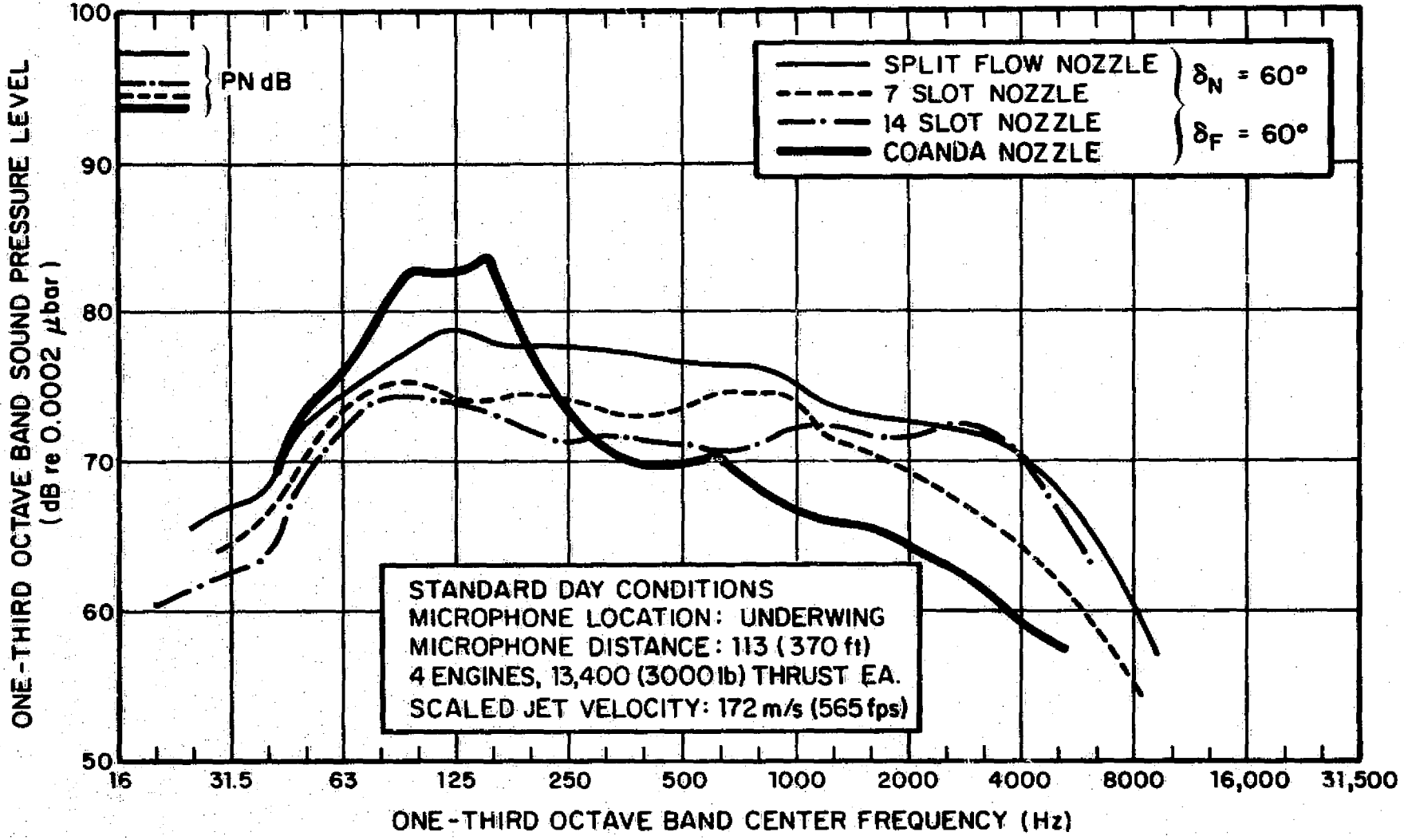

FIG. 13(b). Continued

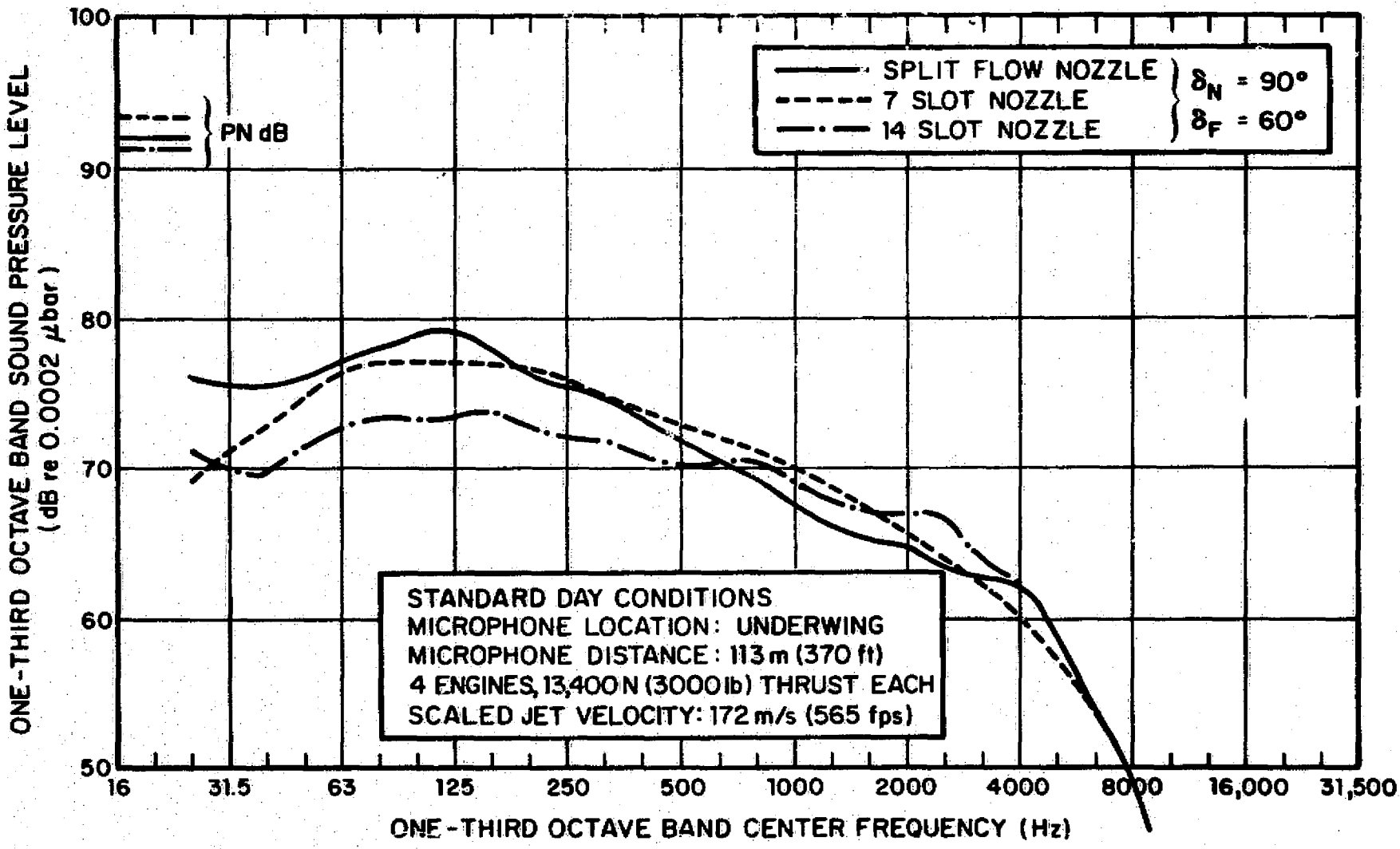

FIG. 13(c). Continued

4. CABIN INTERIOR NOISE

The interior noise of an aircraft during the deployment phase of the propulsive lift device comes from three sources: (1) sound generated by the interaction of the jet exhaust with the propulsive nozzles and flaps, (2) excitation of the fuselage by direct impingement of the turbulent jet exhaust on the cabin walls and (3) vibration which are transmitted from the flap and wing structure to the fuselage.

In this report only (1), - the sound generated by the propulsive lift device, will be considered. Sources (2) and (3) are important, and may, in fact, under certain conditions be the dominant sources, but have little to do with the intrinsic noise production of the propulsive lift device and depend on the engine's location and the structural details of the airframe. We also do not consider here conventional sources of jet aircraft interior noise such as turbomachinery, auxiliaries, jet exhaust, or turbulent boundary layer excitation of the cabin during cruise.

The fuselage noise reduction characteristics used to estimate the STOL aircraft interior noise are shown in Fig. 14. This noise reduction curve is from a recent study [5] of acoustic transmission through a fuselage sidewall. The range of various aircraft data as well as the values chosen for this study are also shown in the figure.

The assumed location of the engines, and the geometry of the relevant portion of the aircraft are shown in Fig. 15. The source noise used in this estimate is the 22° sideline microphone spectra. No atmospheric attenuation was allowed, and all engines are operating at full power with a jet velocity U_{jet} = 244 m/s (800 fps). No forward speed effects are considered.

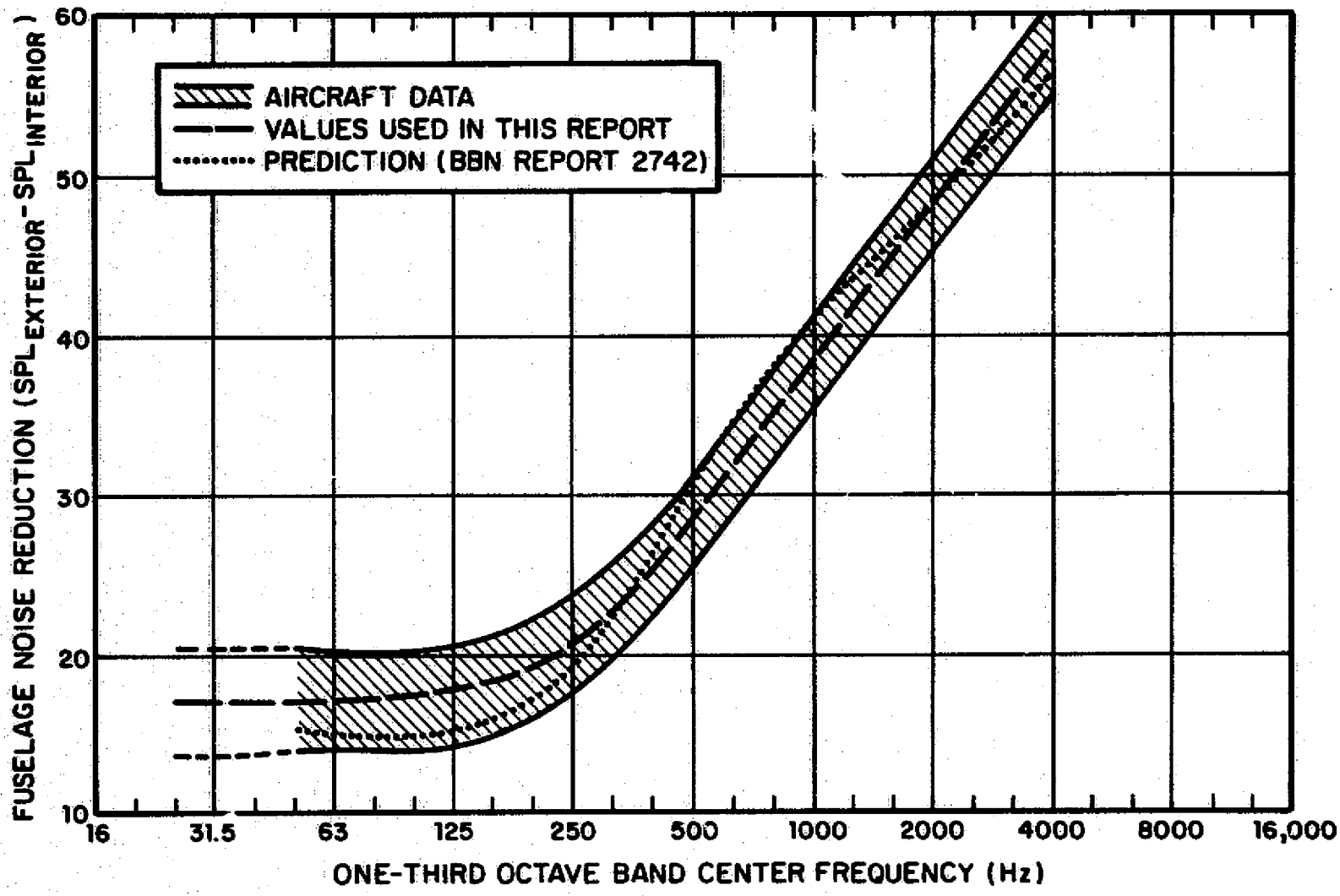

FIG. 14. FUSELAGE NOISE REDUCTION (ACOUSTIC EXCITATION ONLY).

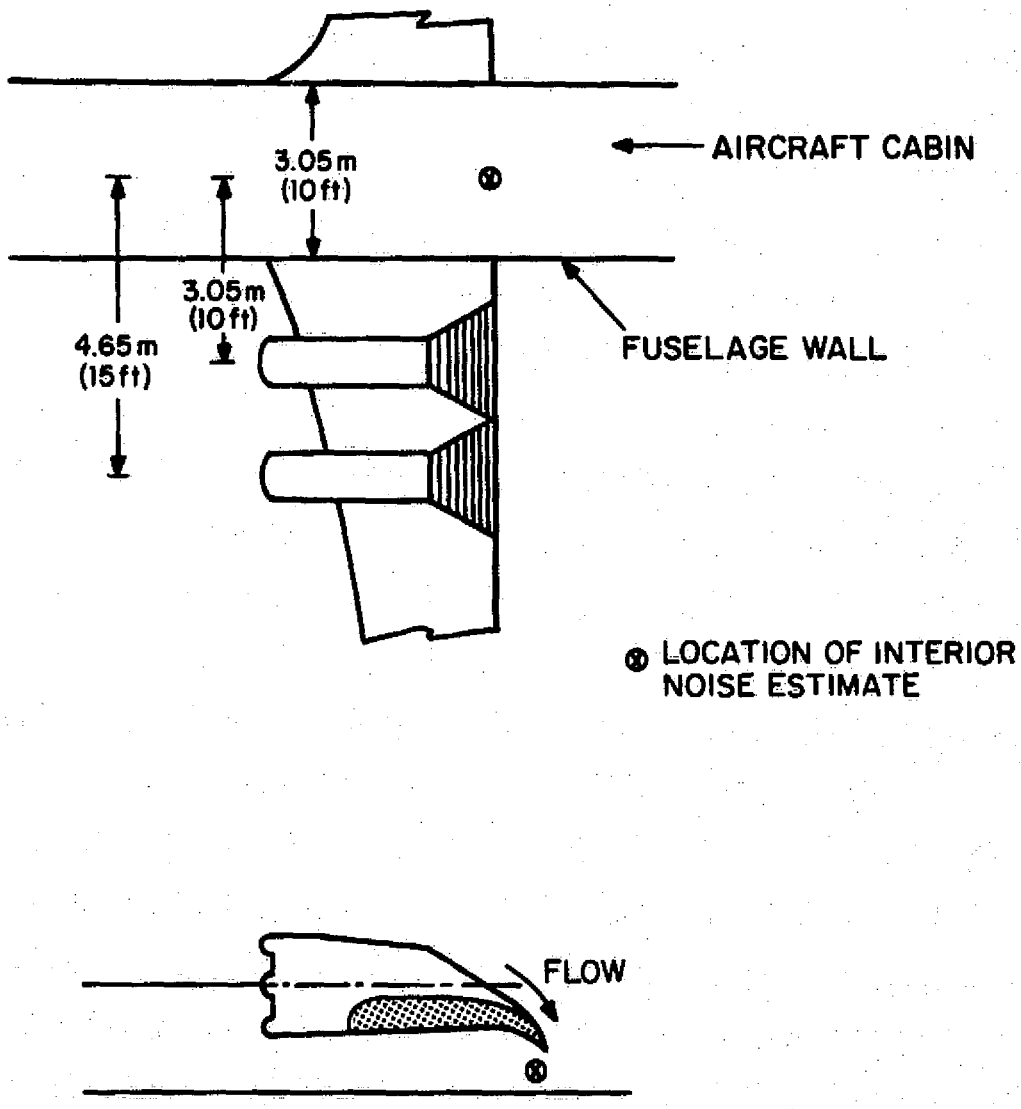

FIG. 15. ASSUMED GEOMETRY FOR CABIN INTERIOR NOISE ESTIMATES.

Figures 16(a,b,c) compare the predicted cabin interior noise levels for the configurations tested. Of particular interest is the comparison between the Coanda nozzle and the multislotted nozzle (Fig. 16b). While the noise levels, when expressed in PNdB, exhibit small differences, the spectral peak of the Coanda nozzle (at 200 Hz) is some 10-15 dB higher than the levels of the other nozzles.

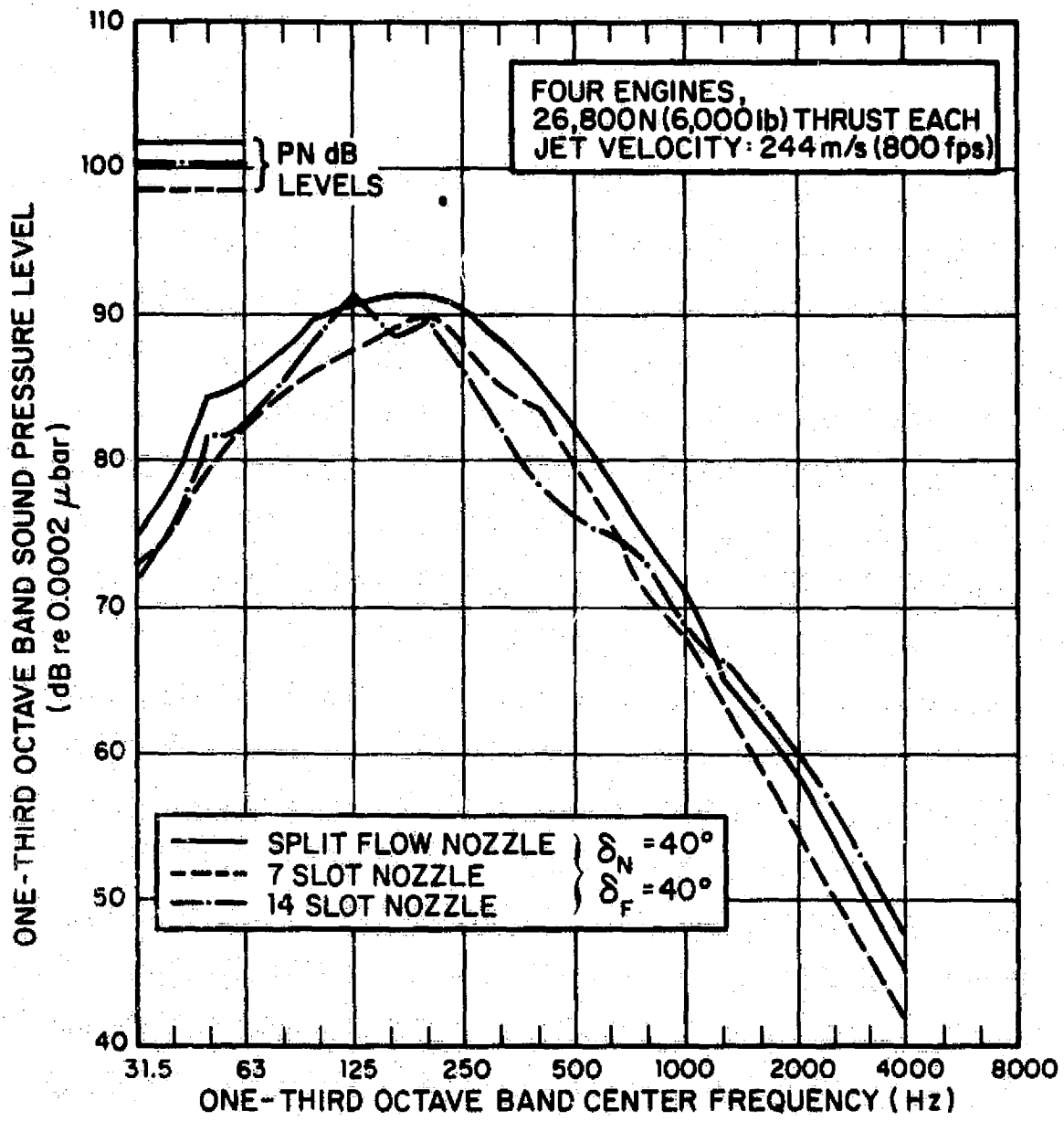

FIG. 16(a). COMPARISON OF CABIN INTERIOR NOISE LEVELS.

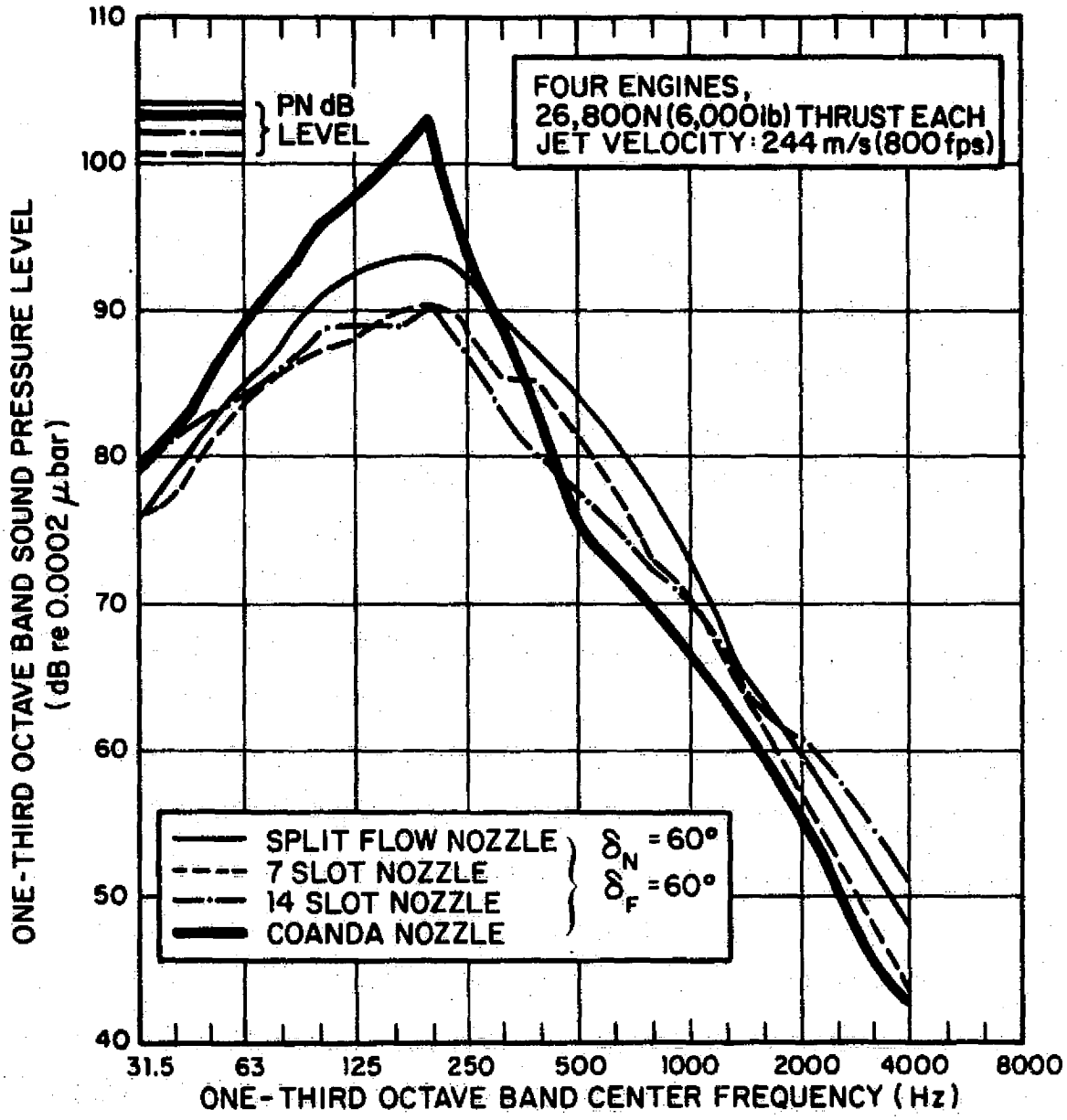

FIG. 16(b). Continued

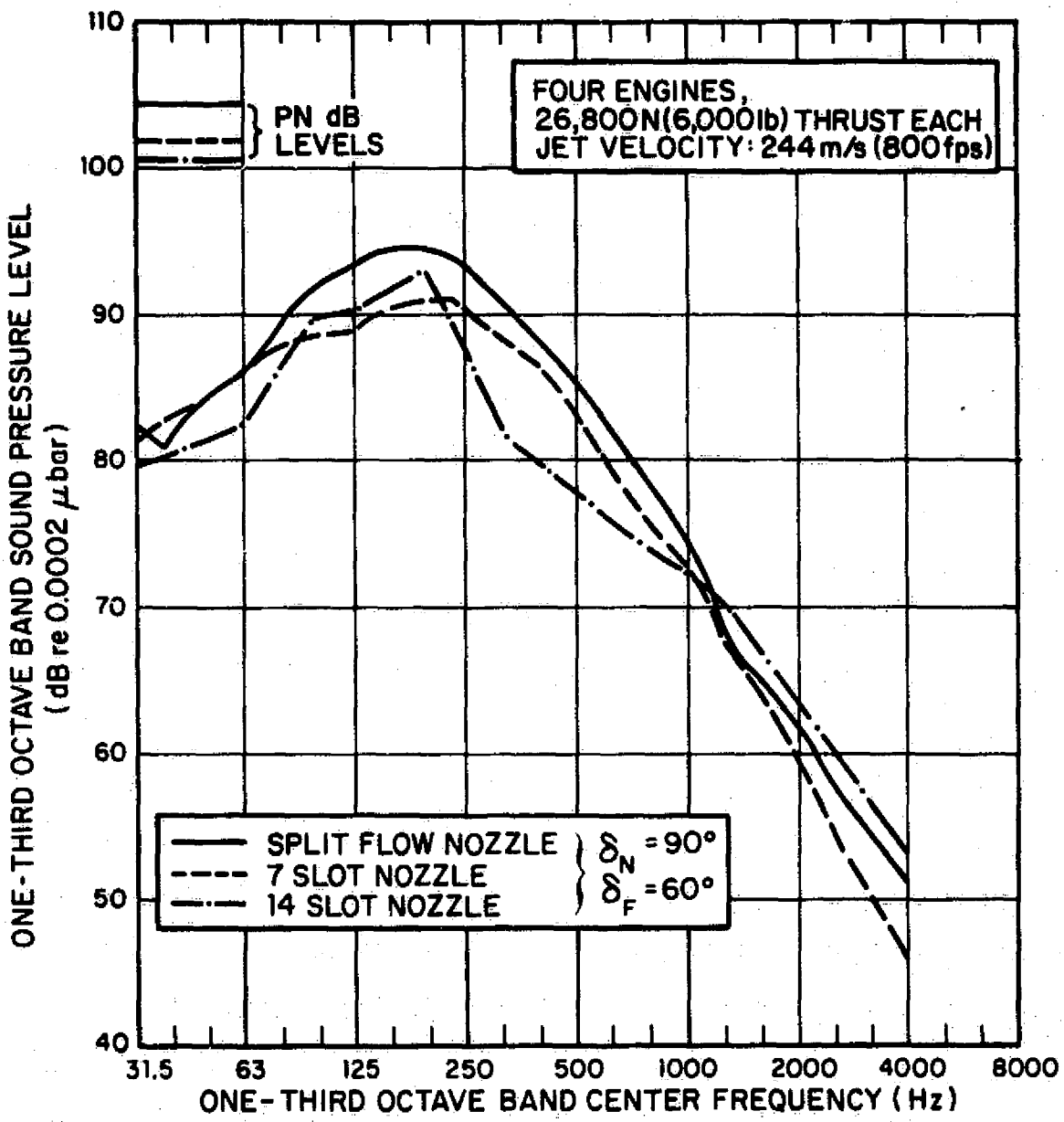

FIG. 16(c). Continued

5. CONCLUSIONS

The following conclusion can be derived from the tests that were carried out in this study:

1. The concept of modifying the flow field of USB devices by blowing the propulsive jet through a cascade of narrow slots achieved the desired result of shifting the acoustic energy to higher frequencies. It was found that the more slots one uses, the less low frequency noise is generated.

2. Significant reductions of the characteristic low frequency spectral peak associated with conventional USB devices were obtained. It is believed that the high frequency noise generated by the multislotted nozzles can be substantially reduced by addressing the noise transduction mechanism. Porous edges, cleaner flow and improved geometry are some of the methods that have been proven beneficial on similar devices.

3. The multislot nozzle designs tested show that by varying the number and location of the slots, one can shape the acoustic spectrum to benefit both the communities near STOL airports and the passengers inside the aircraft.

4. On the basis of acoustic performance, it is hard to choose a multislot nozzle configuration that is clearly superior to the others. It is suggested that further experimentation and analysis are required to optimize, and determine the full potential, of these designs. Larger scale models, which will afford possibilities of

surface treatment and better flow control should be tested. Correlation studies will be very useful to determine the precise location of the noise sources and their contribution to the far field noise.

REFERENCES

1. Kadman, Y., Hayden, R.E., and Scharton, T.D., "Noise Characteristics of Conventional and Multislotted Upper Surface Blowing-Nozzle Concepts With and Without Forward Speed," BBN Report No. 2889, September 1974.

2. Hayden, R.E., Kadman, Y., and Scharton, T.D., "Preliminary Studies of Feasible Noise Reduction Concepts for Upper Surface Blown (USB) Propulsive Wings," BBN Report No. 2770, February 1974.

3. Renselaer, D.J., "A Comparison of Aerodynamic Test Data of Upper Surface Blown Flaps with Single and Multiple Thrust Exhausts," LAAD, Rockwell International Report NA-74-324.

4. Renselaer, D.J., Nishida, R.S., and Wilkin, C.A., "Small Scale Noise and Wind Tunnel Test of Upper Surface Blowing Nozzle Flap Concepts," Volume I. "Aerodynamic Test Results." NASA CR-137747, December 1975.

5. Wilby, J.F., and Scharton, T.D., "Acoustic Transmission Through a Fuselage Sidewall," BBN Report No. 2742, July 1974.

6. Hayden, R.E., Scharton, T.D., Kadman, Y., Wilby, J. and Rudd, M.J., "A Preliminary Evaluation of Noise Reduction Potential for the Upper Surface Blown Flap," BBN Report No. 2478, Nov. 1972.

7. Scharton, T.D., Pinkel, B., Wilby, J.F., and Hansen, G.L., "A Study of Trailing Edge Blowing as a Means of Reducing Noise Generated by the Interaction of Flow with a Surface," BBN Report No. 2593, September, 1973.

8. Hayden, R.E., "Exploratory Investigation of Aeroacoustic Optimization of the Variable Impedance Edge Concept Applied to Upper Surface Blown Configurations," BBN Report No. 3245, February 1976.

9. Renselaer, D.J., private communication. These values were measured in the experimental study that is reported in [4].

APPENDIX A: SCALING OF EXPERIMENTAL RESULTS

The basic relationships between the acoustic performance for the model and for the full-scale configuration follow:

Level Scaling

$$SPL_{fs} = SPL_m + 10n\log \frac{U_{fs}}{U_m} - 20 \log \frac{r_{fs}}{r_m} + 10 \log \frac{A_{fs}}{A_m} \quad .$$

where n is the power dependence of the sound level on the velocity.

Frequency Scaling is based on constant Strouhal number scaling: i.e.,

$$S_m = \frac{f_m d_m}{U_m} = \frac{f_{fs} d_{fs}}{U_{fs}} = S_{fs} \quad ,$$

which yields

$$\frac{f_{fs}}{f_m} = \frac{U_{fs}}{U_m} \cdot \frac{d_m}{d_{fs}} \quad ,$$

where U is flow velocity, r is distance to observation point, A is nozzle area, d is characteristic nozzle dimension, f is frequency, S is Strouhal number, and the subscripts m and fs denote model and full scale, respectively.

The scaling factor

$$K = d_{fs}/d_m$$

is determined by the thrust requirements. The "reference thrust," defined in the aerodynamic section of this report (Reference 4), has been used as shown in Table A.1.

TABLE A.1. SCALING FACTOR DETERMINATION

USB Device	T_o Reference* Thrust N(lbs)	U_o Reference** Thrust Velocity m/s (ft/s)	U_{fs} Full Power Jet Velocity m/s (ft/sec)	T_m Model Thrust at 244 m/s Jet Velocity N(lbs)	K Scaling Factor $\sqrt{\frac{26800}{T_m}}$	ΔdB_K Level Change Due to Scaling 20 log K
7-Slot Nozzle	465 (105)	148 (486)	244 (800)	1140 (257)	4.84	+13.7
14-Slot Nozzle	457 (103)	165 (541)	244 (800)	998 (225)	5.16	+14.2
Split Flow Nozzle	412 (93)	137 (458)	244 (800)	1260 (284)	4.6	+13.2

*Reference 4.
**Reference 9.

All nozzles are assumed to be operating with cold flow with flow velocity of 244 m/s. Since the efficiencies of the nozzles vary, the scaling factor is not the same for each configuration. An alternative way of scaling would be to decide on a geometrical scale factor and adjust the pressure ratio of each device to arrive at the required thrust. This latter method, however, costs more in terms of noise since the noise levels are proportional to U_{jet}^5. The level change due to the increase in the area from the model to the full scale device is tabulated in Table A.1.

Level corrections due to change in distance to the observation point (from r_m = 2.29 m to r_{fs} = 152 m) are given, for all models, by

$$\Delta dB_r = 20 \log \frac{2.29}{152} = -36.5 \text{ dB}.$$

Level correction due to velocity change (e.g., from U_m = 152 m/s to U_{fs} = 244 m/s) is given by

$$\Delta dB_U = 50 \log \frac{244}{152} = 10 \text{ dB}.$$

Finally, four engines are to be used on the full scale aircraft which will increase the individual engine noise output by a factor of four, i.e., 6 dB.

We can now sum all the level correction factors:

$$SPL_{fs} = SPL_m + \Delta dB_K + \Delta dB_r + \Delta dB_U + 6$$

$$= SPL_m - \begin{cases} -5.2 \text{ dB for 7-slot nozzle} \\ -5.75 \text{ dB for 14-slot nozzle} \\ -4.75 \text{ dB for split flow nozzle} \end{cases}$$

The frequency scaling will be given by

$$\frac{f_{fs}}{f_m} = \frac{U_{fs}}{U_m} \cdot \frac{1}{K} = \frac{244}{152} \times \frac{1}{5} = .32$$

i.e., five third octave band down in frequency.

The reliability of the velocity scaling, and the associated frequency scaling can be tested by normalization of the model noise output at different velocities. As mentioned before, the velocity scaling is not clear cut. Figures A.1 through A.3 show the result of such scaling for the 7-slot nozzle. The shaded area represents the range into which the sound spectra from three jet velocities (122, 152, 186 m/s) normalize. This range is acceptably narrow, particularly at the spectra peaks.

One should note that the scaling was performed at constant aspect ratio. Since the individual slot size can be varied independently of the nozzle dimensions, one could change the number of slots to shift the peak level frequencies without altering the size of the nozzles.

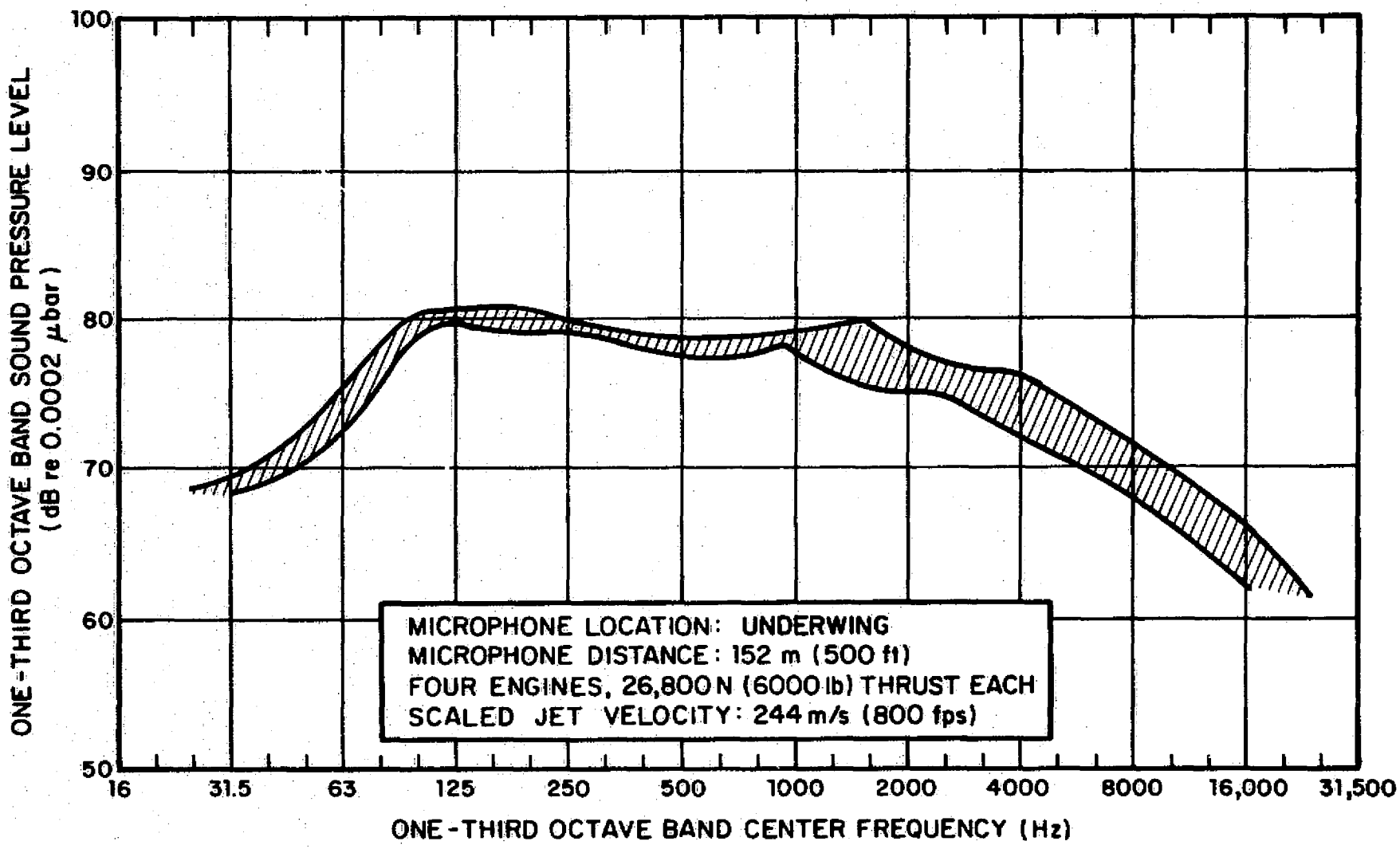

FIG. A.1. VELOCITY AND FREQUENCY NORMALIZATION FOR 7-SLOTTED NOZZLE $\delta_N = 60°$, $\delta_F = 60°$.

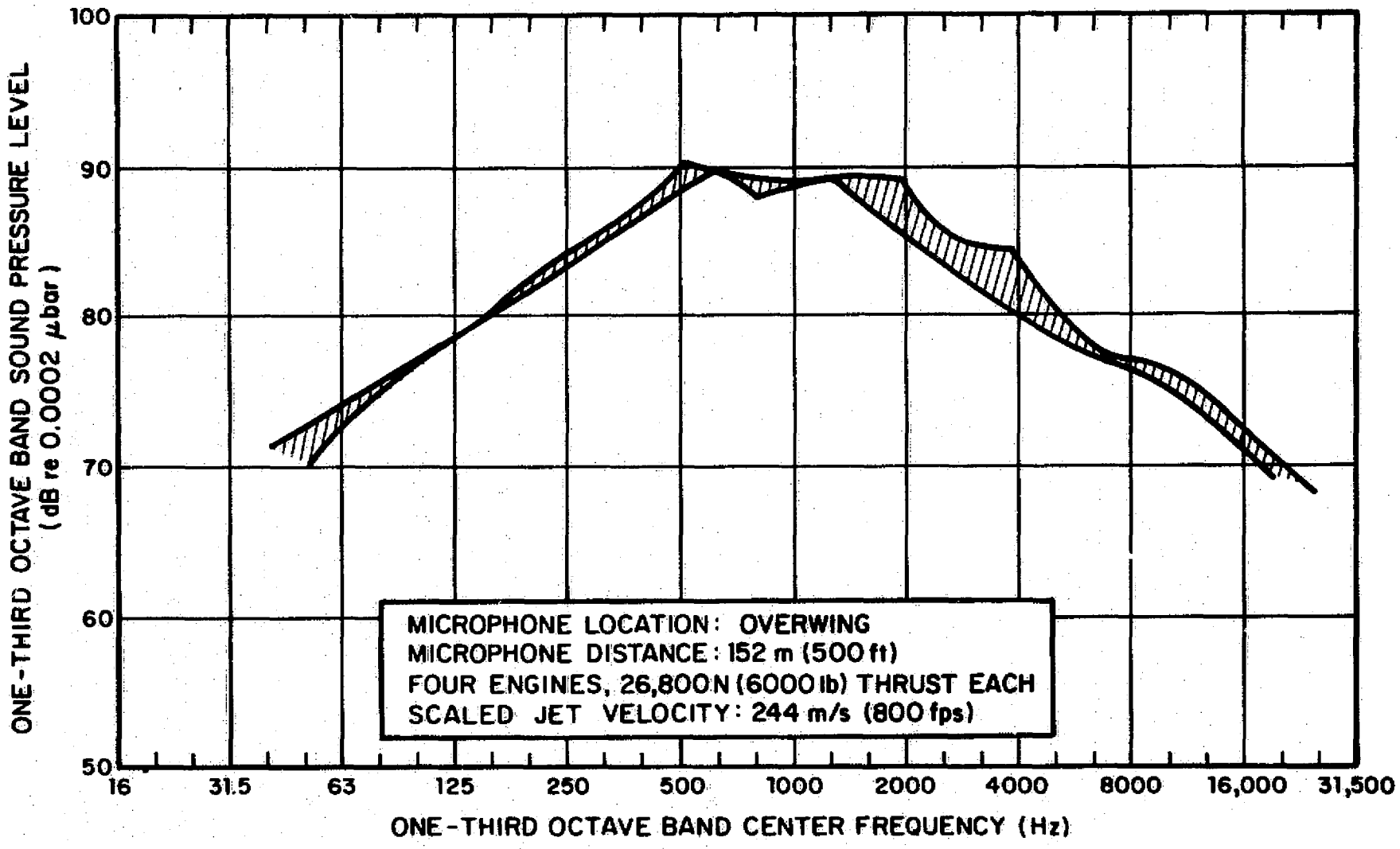

FIG. A.2. Continued

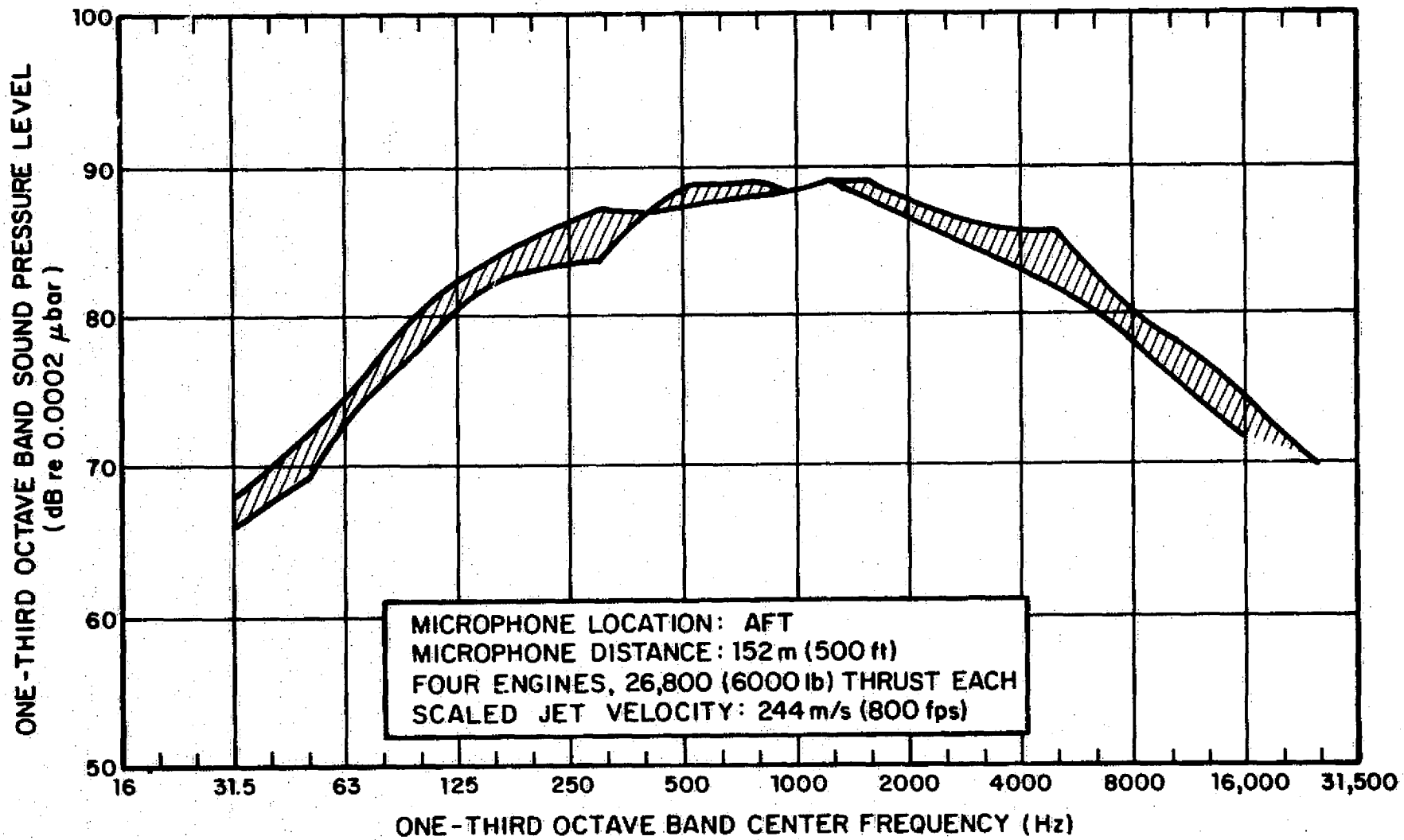

FIG. A.3. Continued

APPENDIX B: PRESENTATION OF RAW DATA

In Figs. B.1 through B.75, the raw data that has been acquired in the experimental effort is presented.

Table B.1 is a summary of and a guide to the figures. Refer to Fig. 5 for the sideline and flyover plane microphone arrangement.

As shown on the figures, the acoustic spectra were usually taken for three jet velocities: 122 m/s (400 ft/sec), 152 m/s (500 ft/sec) and 192 m/s (630 ft/sec).

TABLE B.1. SUMMARY OF RAW DATA FIGURES.

Model Type	Figures	Measurement Plane	Nozzle Flap Setting δ_N [deg]	Mechanical Flap Setting δ_F [deg]	Microphone Distance
7-SLOT NOZZLE	B.1-B.11 B.12 B.13	Flyover 37° Sideline 22° Sideline	40	40	2.3 m (7.5 ft) for flyover 4.35 m (14.3 ft) for sidelines
	B.14-B.24 B.25 B.26	Flyover 37° Sideline 22° Sideline	60	60	
	B.27-B.36 B.37 B.38	Flyover 22° Sideline 37° Sideline	90	60	
SPLIT NOZZLE	B.39-B.49 B.50 B.51	Flyover 37° Sideline 22° Sideline	40	40	2.3 m (7.5 ft) for flyover 4.35 m (14.3 ft) for sidelines
	B.52-B.60 B.61 B.62	Flyover 37° Sideline 22° Sideline	60	60	
	B.63-B.73 B.74 B.75	Flyover 37° Sideline 22° Sideline	90	60	

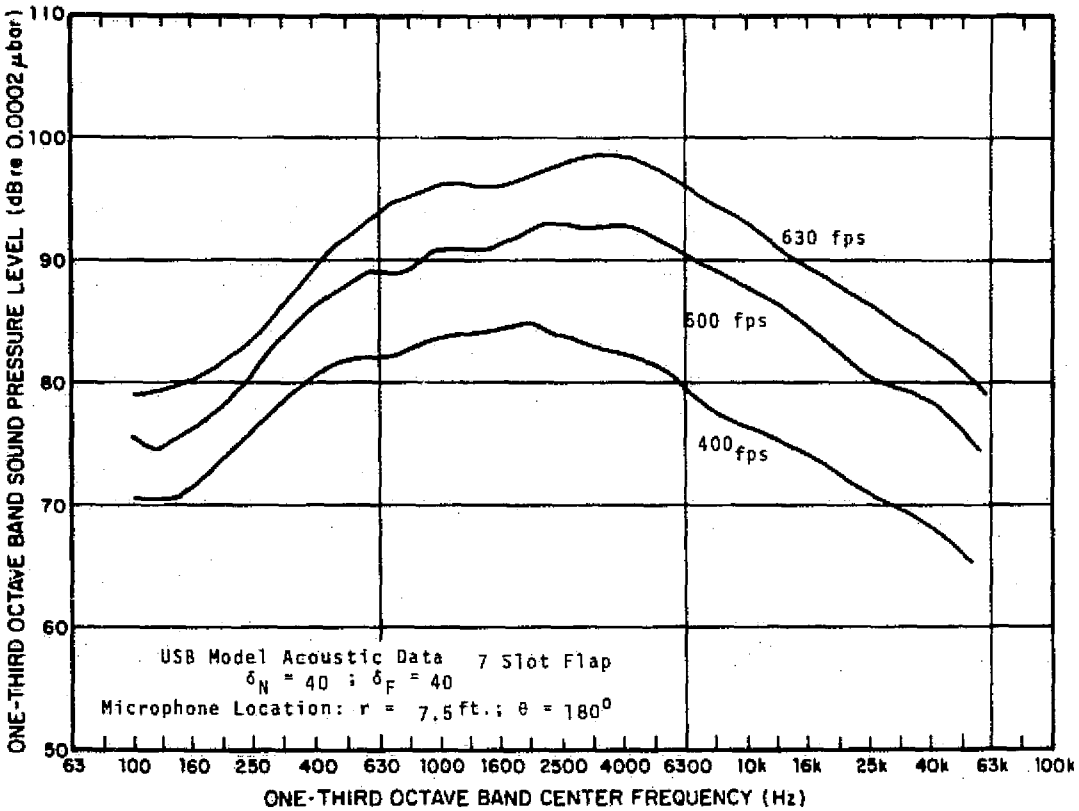

FIG. B- 1 RAW DATA FROM PROPULSIVE LIFT DEVICE MODEL TEST.

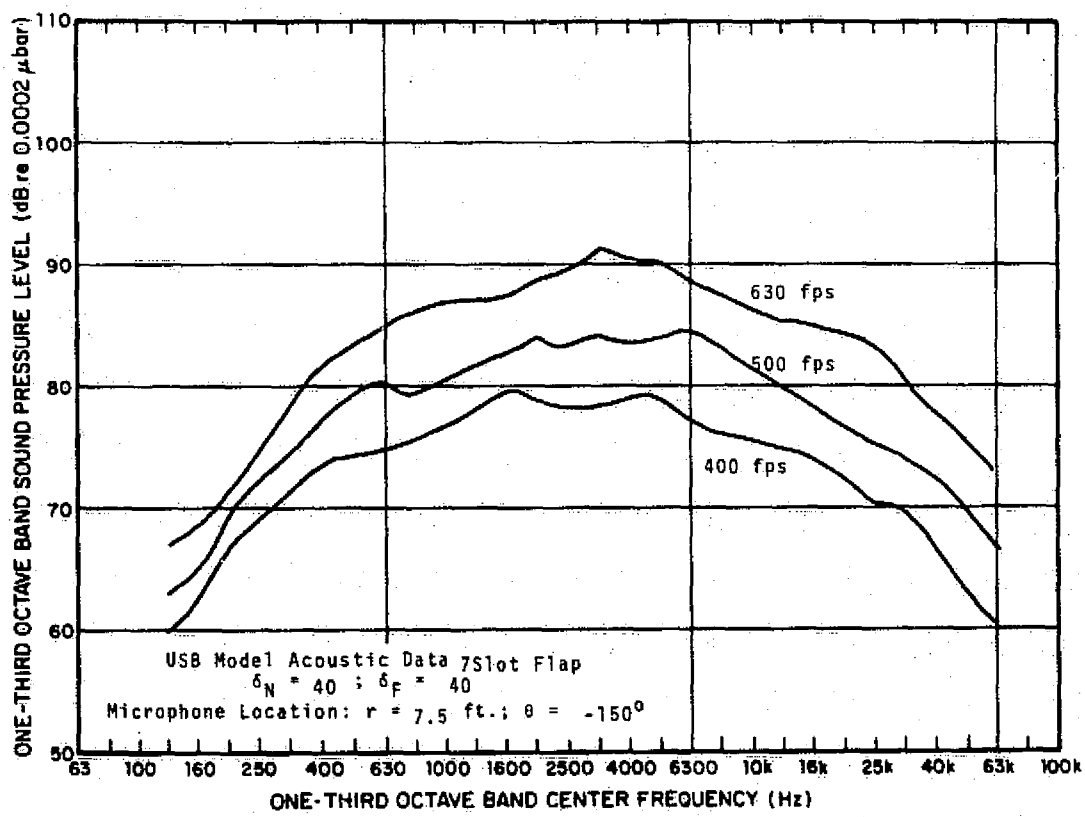

FIG. B- 2 RAW DATA FROM PROPULSIVE LIFT DEVICE MODEL TEST.

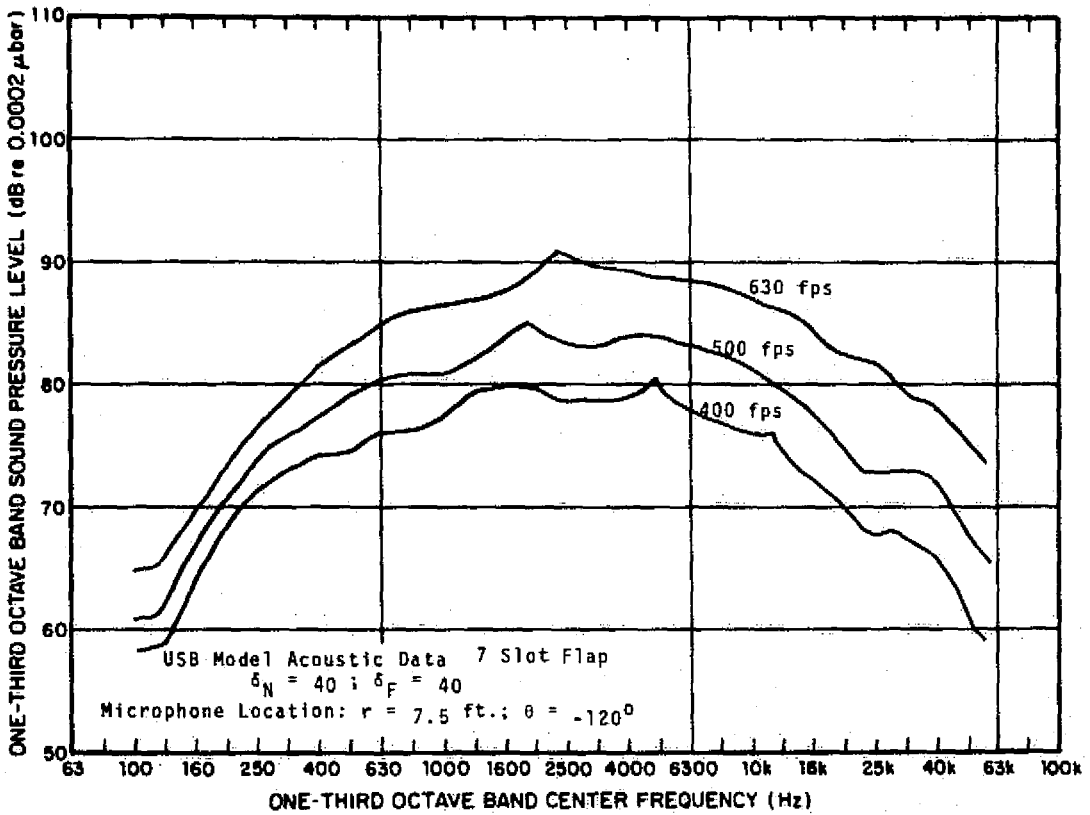

FIG. B- 3 RAW DATA FROM PROPULSIVE LIFT DEVICE MODEL TEST.

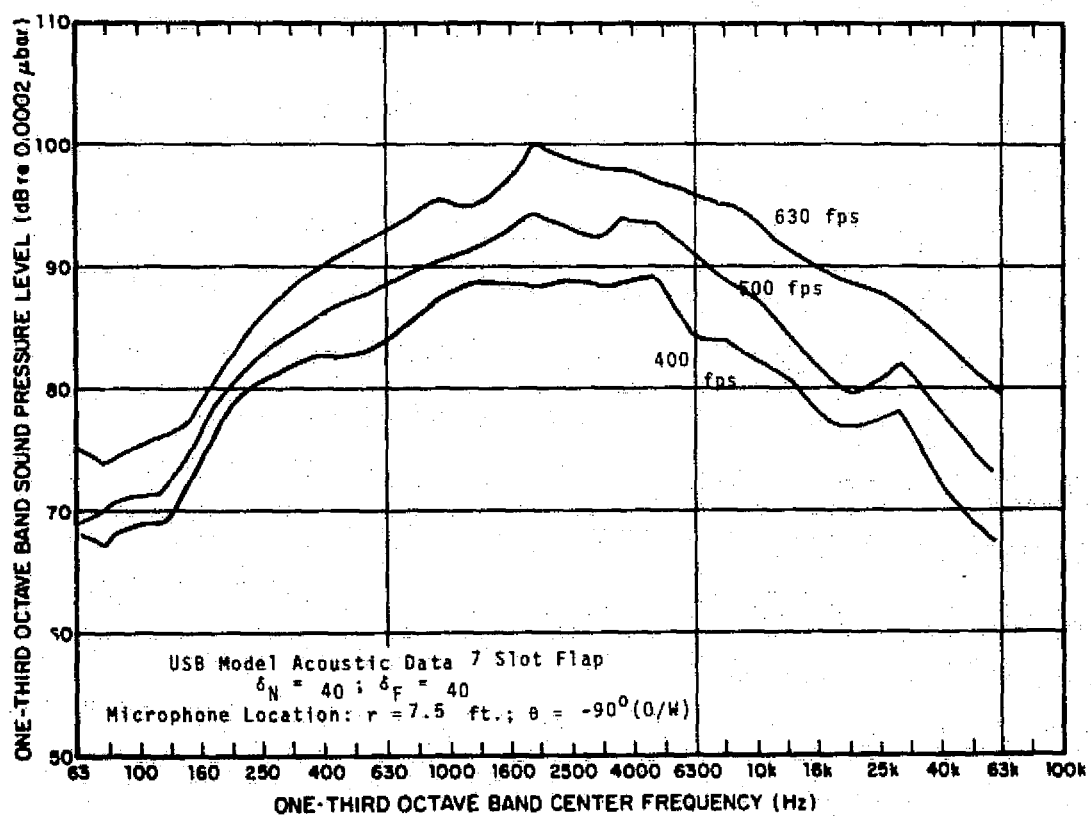

FIG. B- 4 RAW DATA FROM PROPULSIVE LIFT DEVICE MODEL TEST.

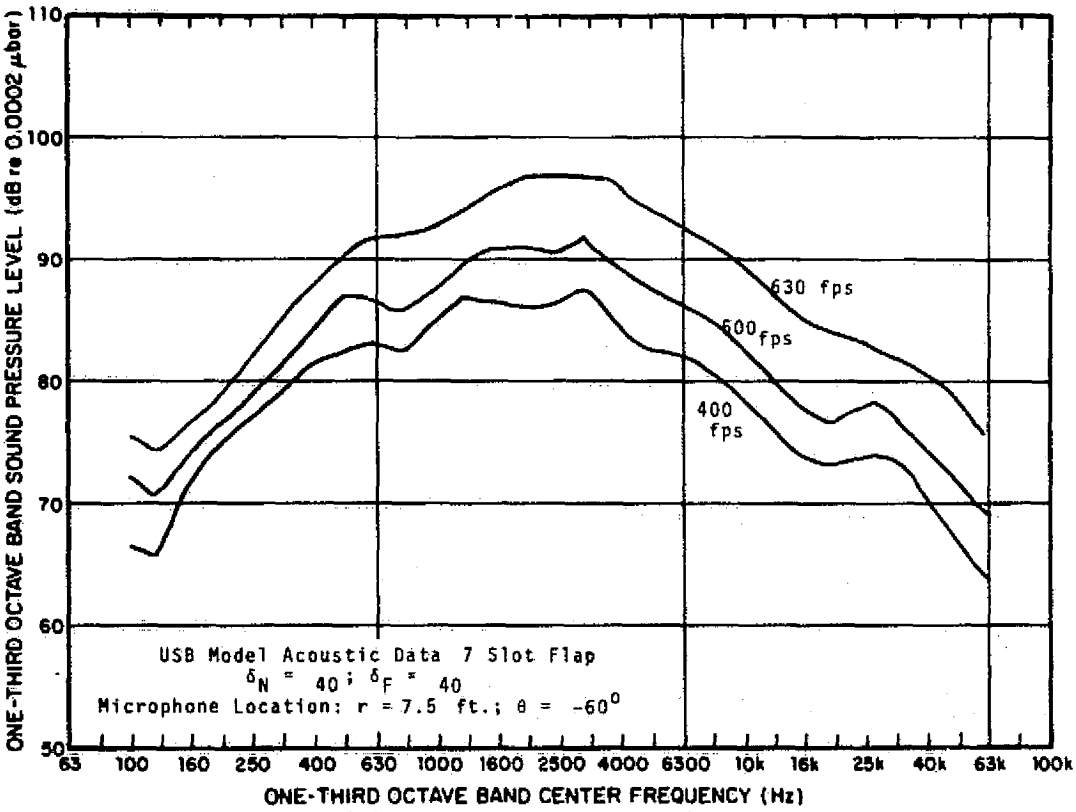

FIG. B- 5 RAW DATA FROM PROPULSIVE LIFT DEVICE MODEL TEST.

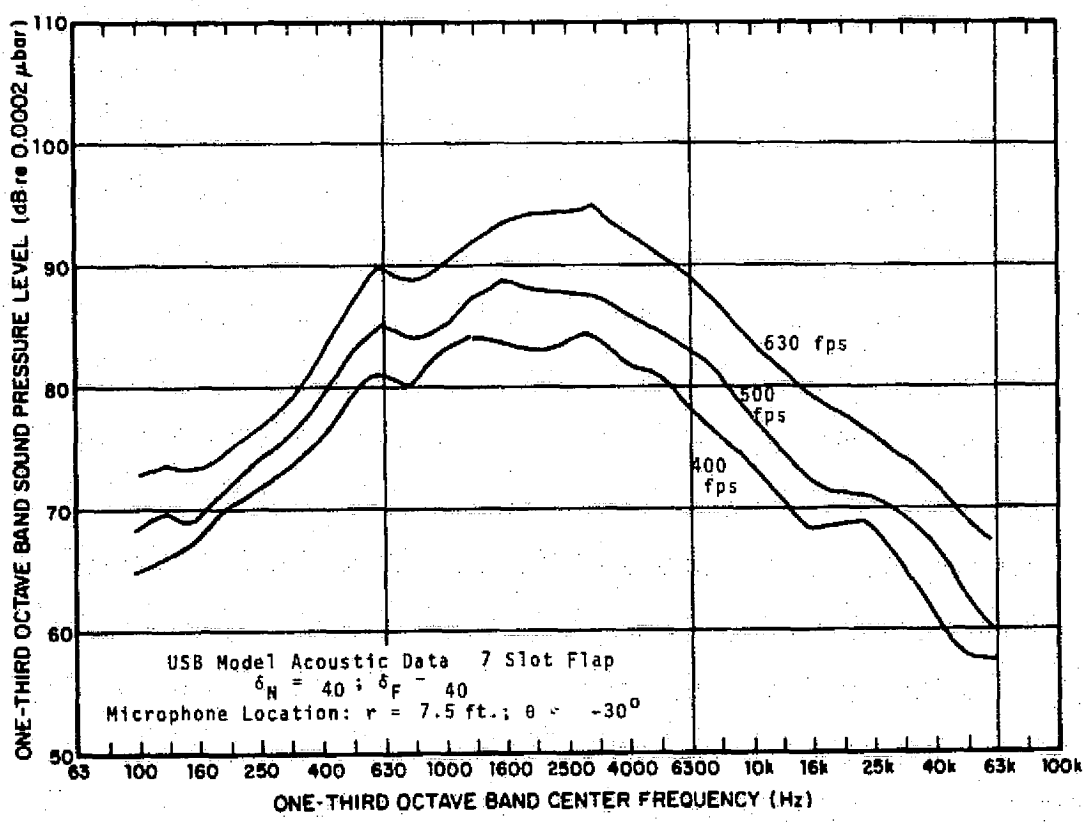

FIG. B- 6 RAW DATA FROM PROPULSIVE LIFT DEVICE MODEL TEST.

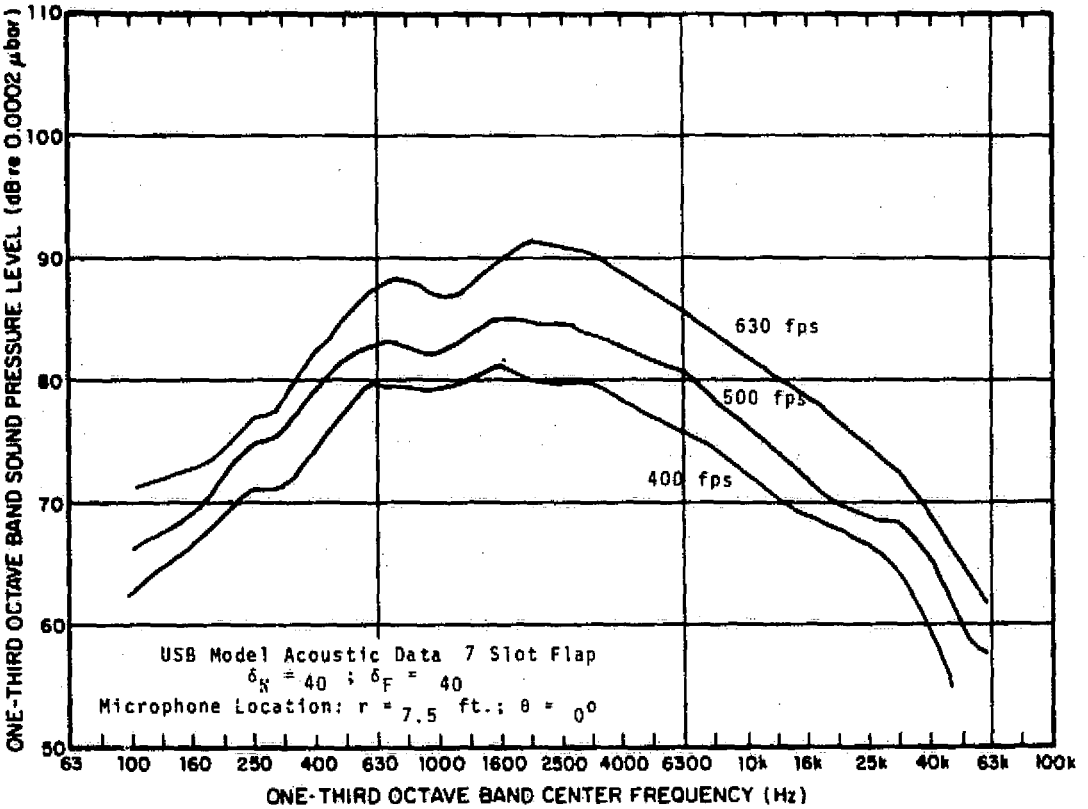

FIG. B-7 RAW DATA FROM PROPULSIVE LIFT DEVICE MODEL TEST.

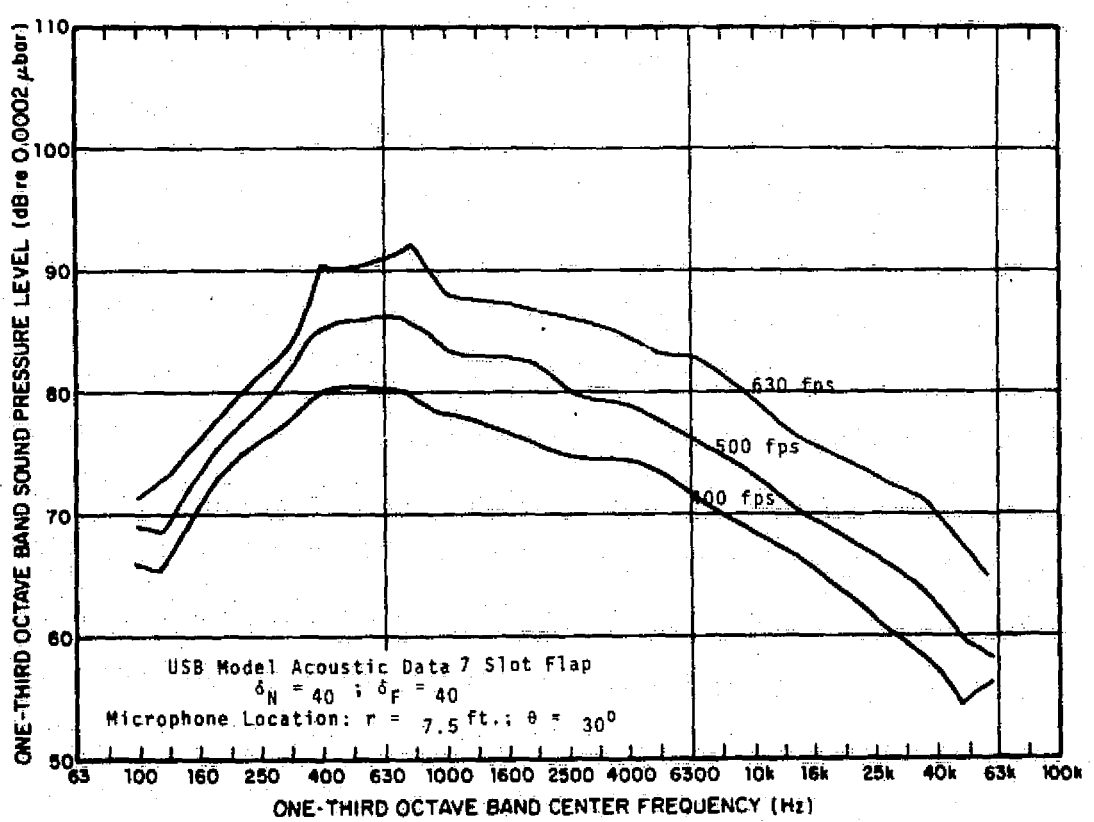

FIG. B- 8 RAW DATA FROM PROPULSIVE LIFT DEVICE MODEL TEST.

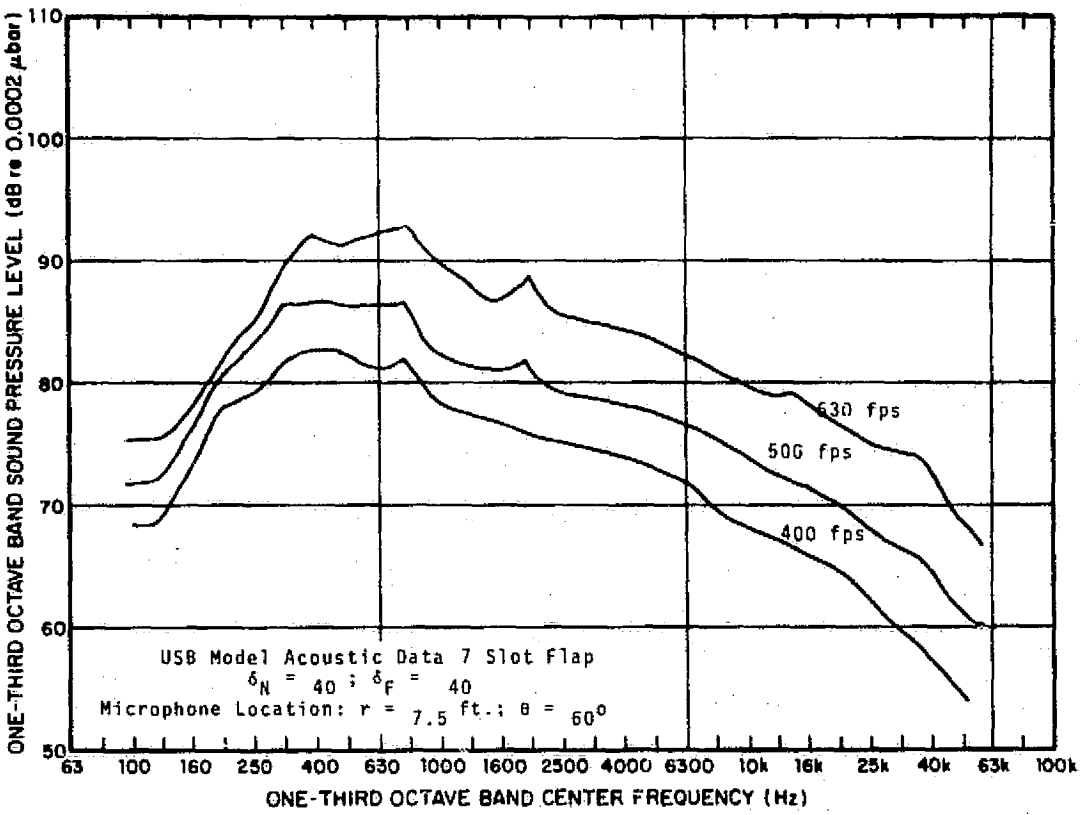

FIG. B- 9 RAW DATA FROM PROPULSIVE LIFT DEVICE MODEL TEST.

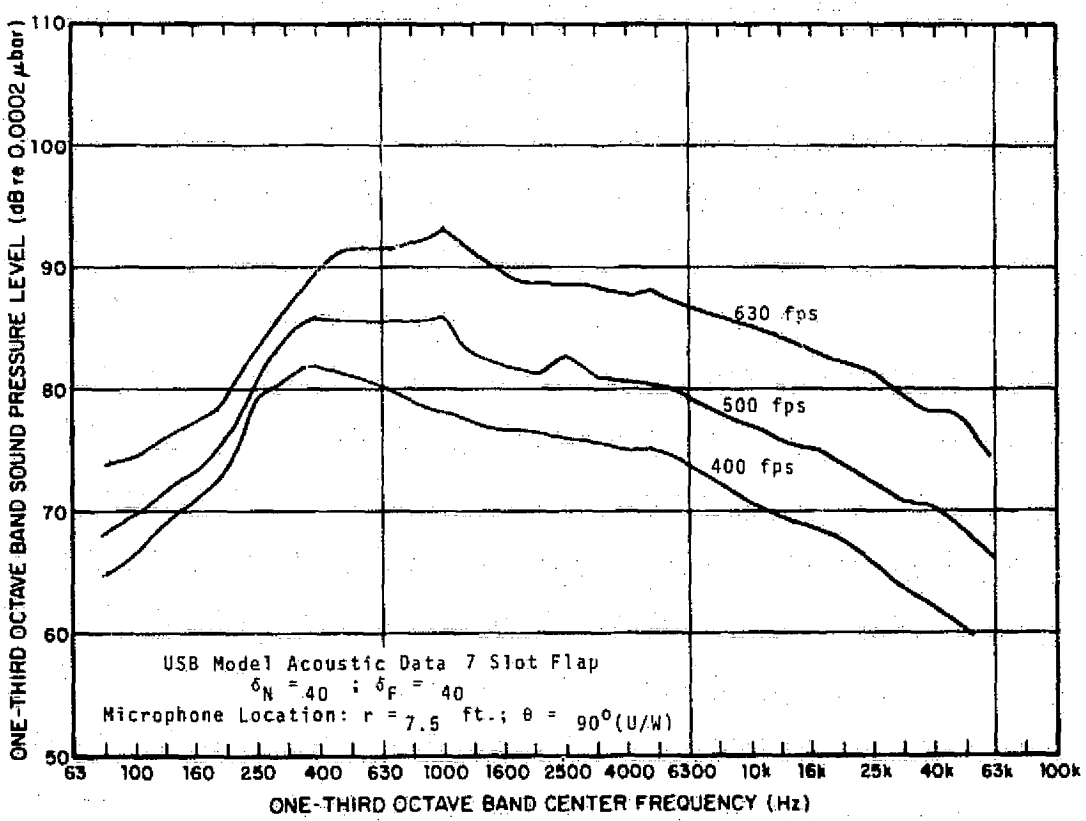

FIG. B-10 RAW DATA FROM PROPULSIVE LIFT DEVICE MODEL TEST.

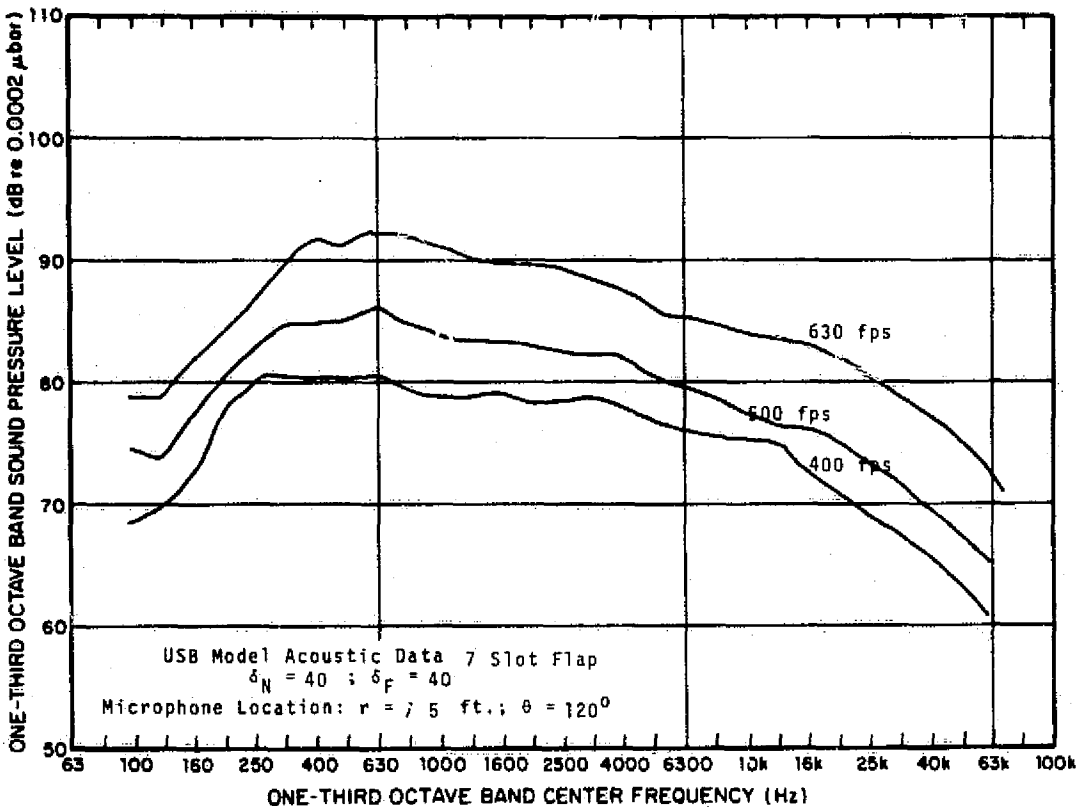

FIG. B-11 RAW DATA FROM PROPULSIVE LIFT DEVICE MODEL TEST.

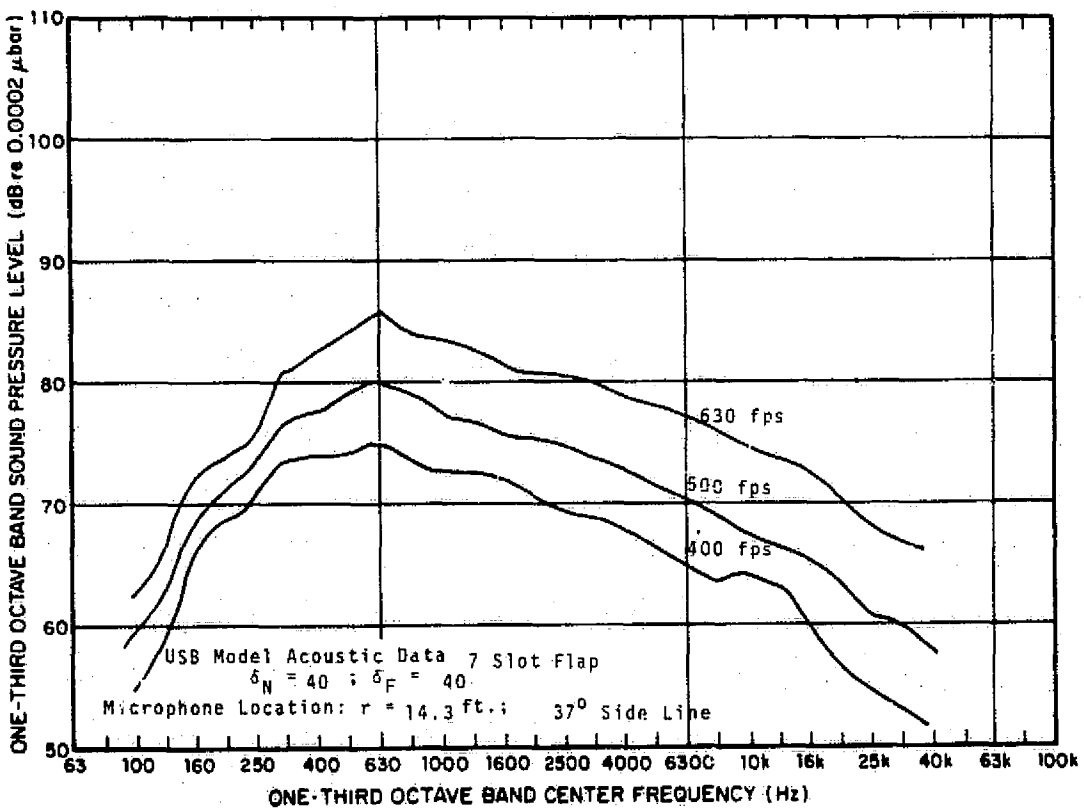

FIG. B-12 RAW DATA FROM PROPULSIVE LIFT DEVICE MODEL TEST.

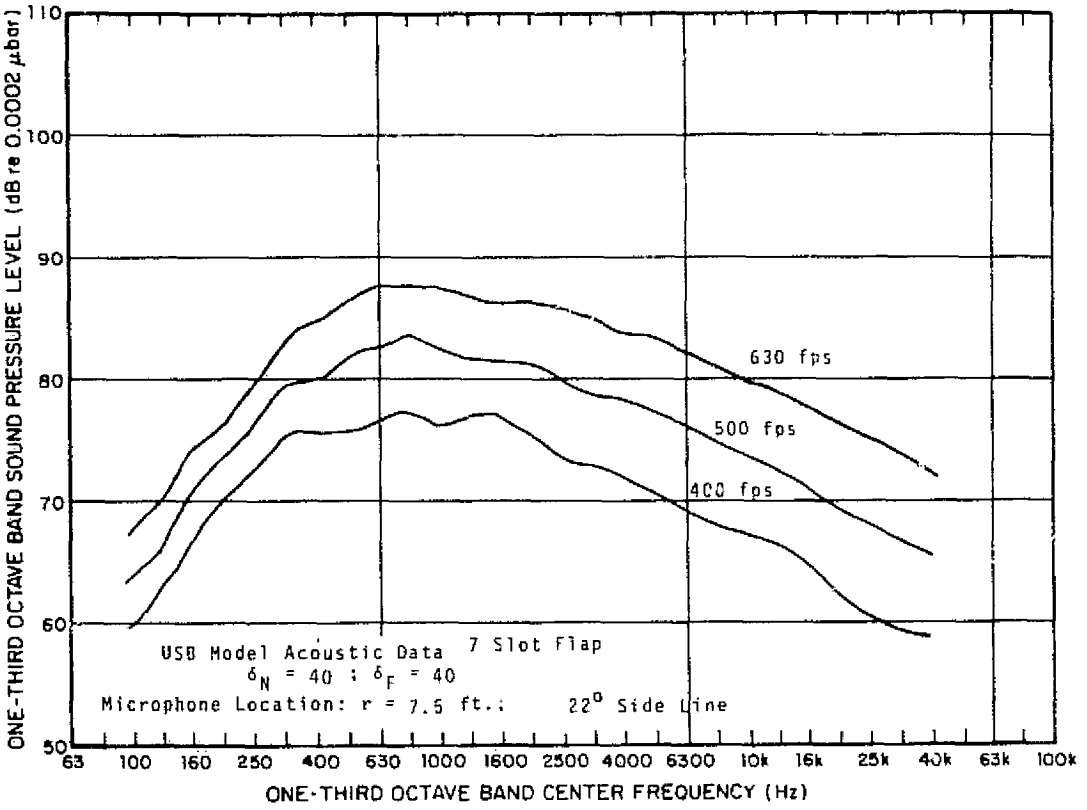

FIG. B- 13 RAW DATA FROM PROPULSIVE LIFT DEVICE MODEL TEST.

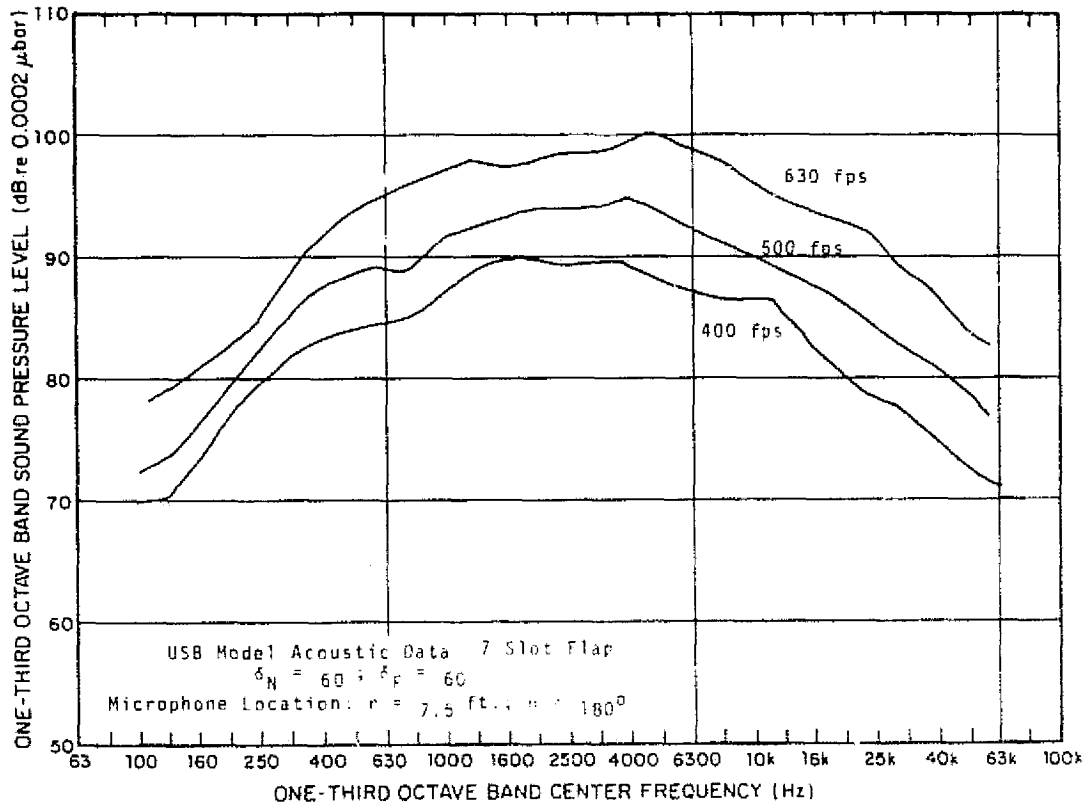

FIG. B- 14 RAW DATA FROM PROPULSIVE LIFT DEVICE MODEL TEST.

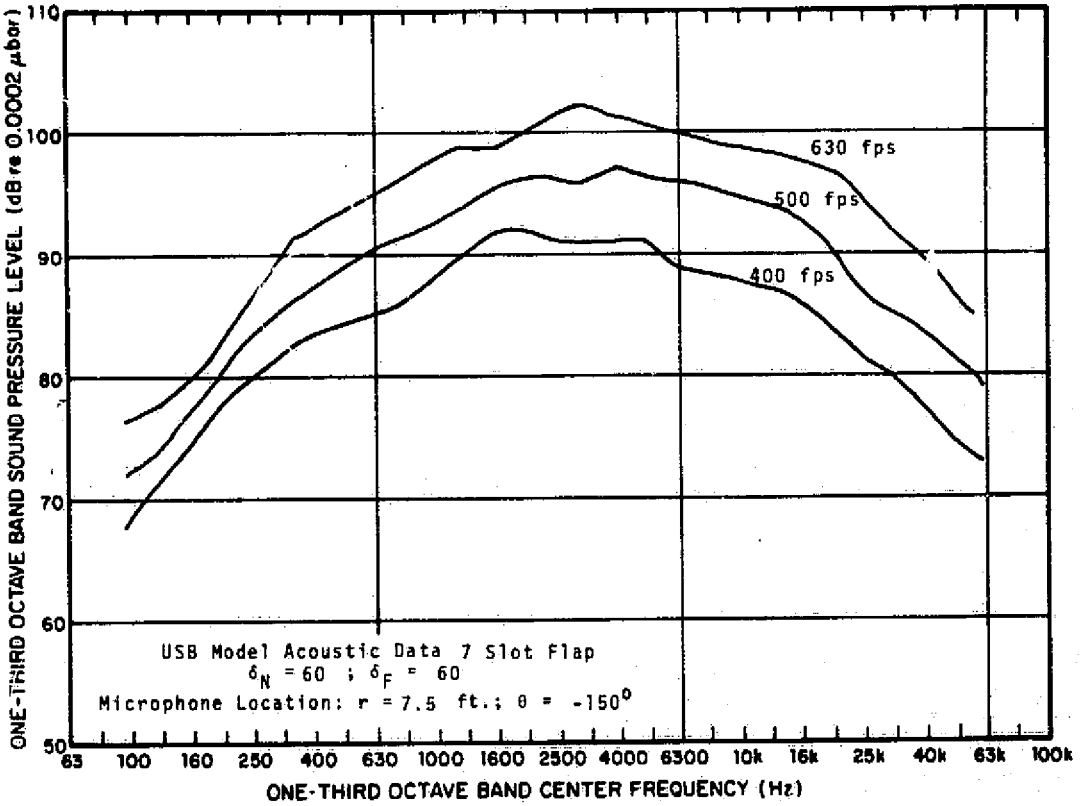

FIG. B-15 RAW DATA FROM PROPULSIVE LIFT DEVICE MODEL TEST.

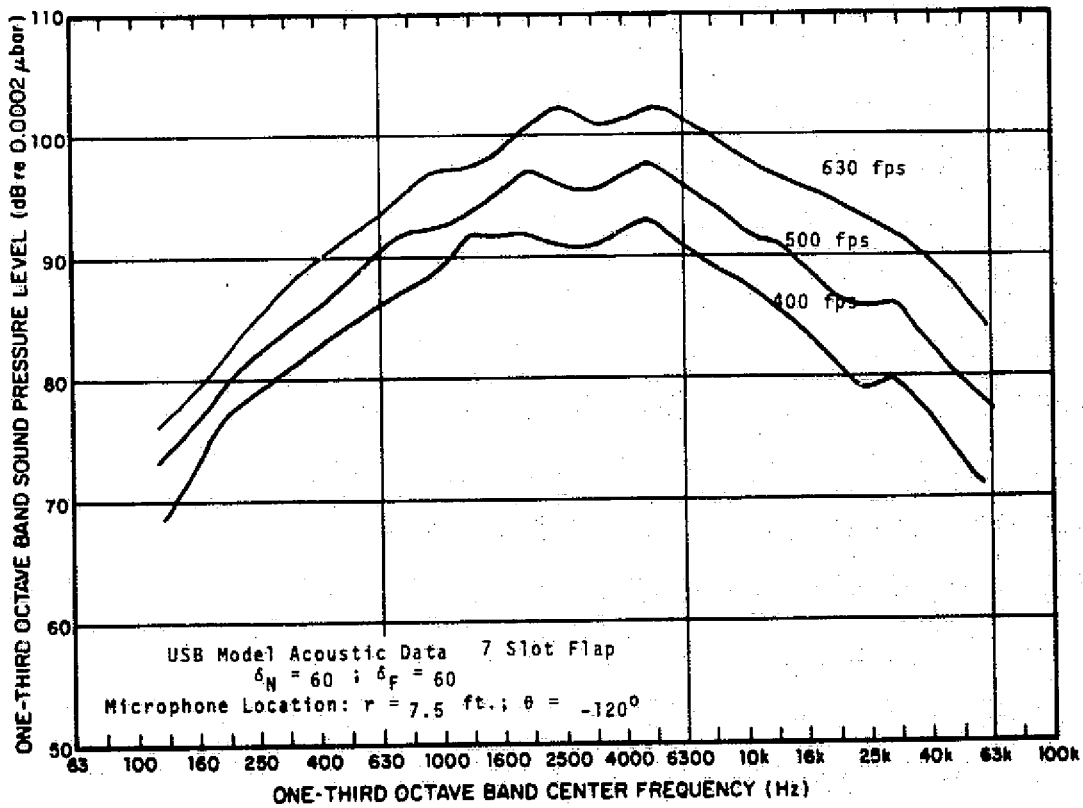

FIG. B-16 RAW DATA FROM PROPULSIVE LIFT DEVICE MODEL TEST.

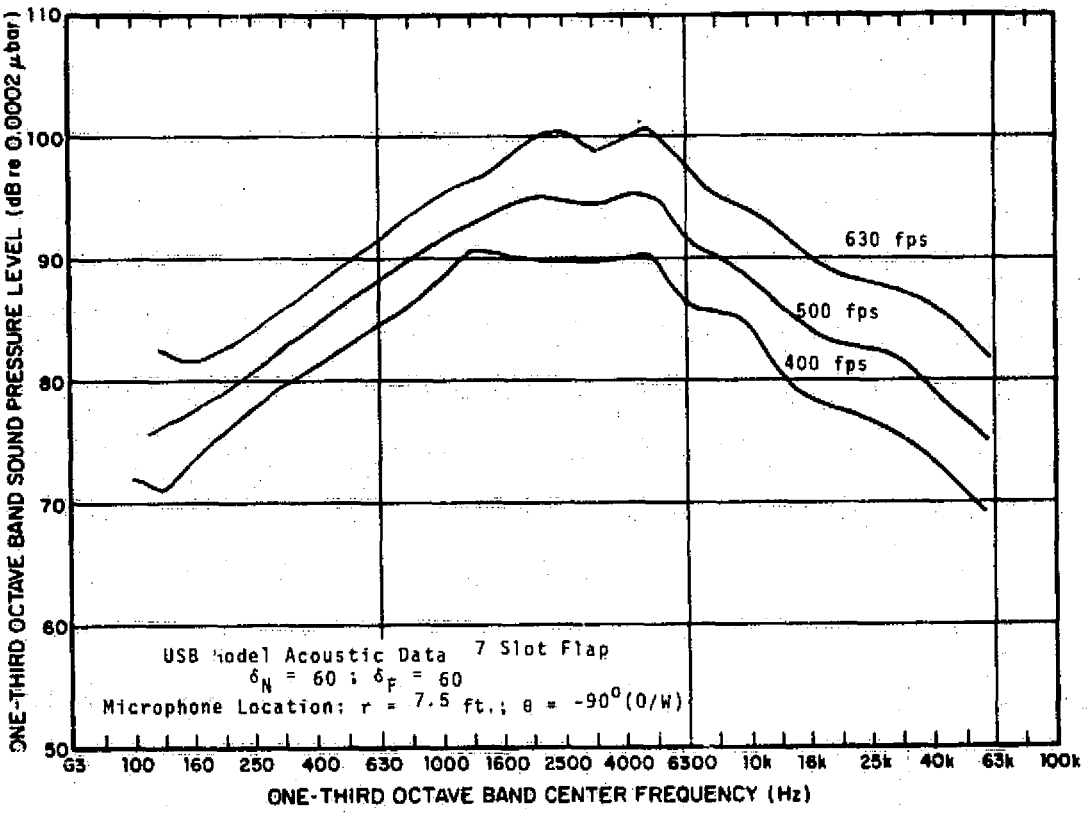

FIG. B- 17 RAW DATA FROM PROPULSIVE LIFT DEVICE MODEL TEST.

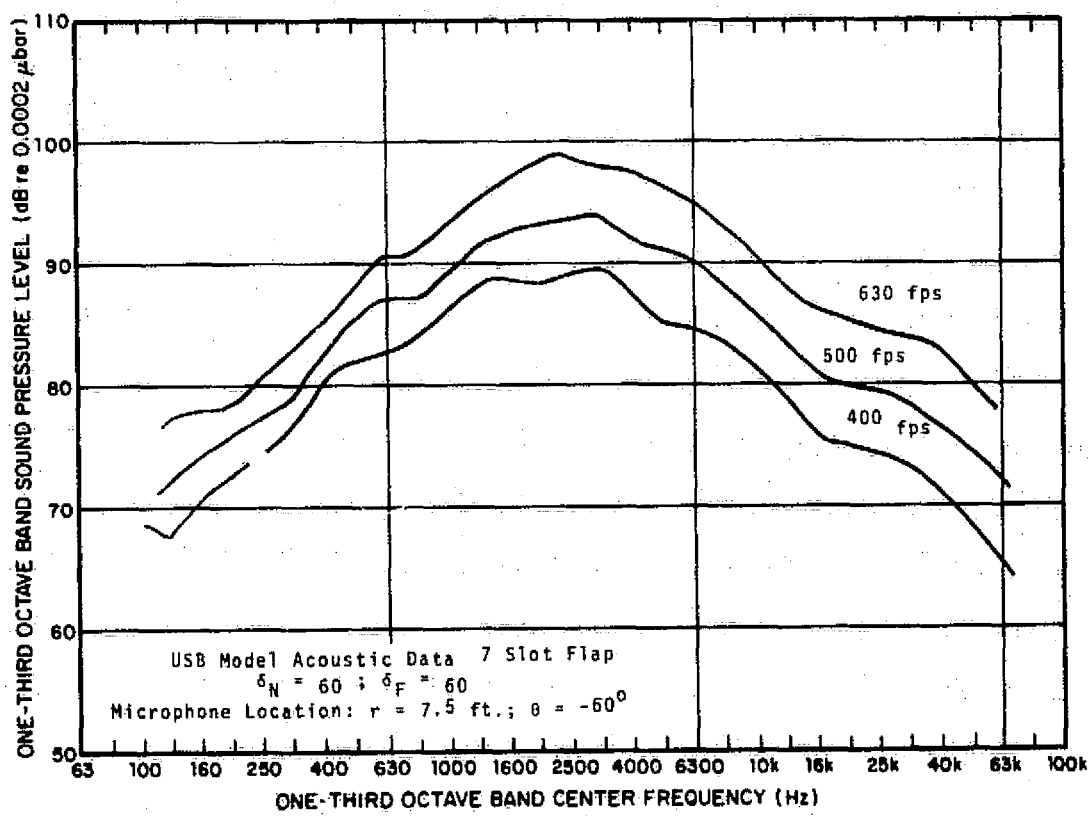

FIG. B- 18 RAW DATA FROM PROPULSIVE LIFT DEVICE MODEL TEST.

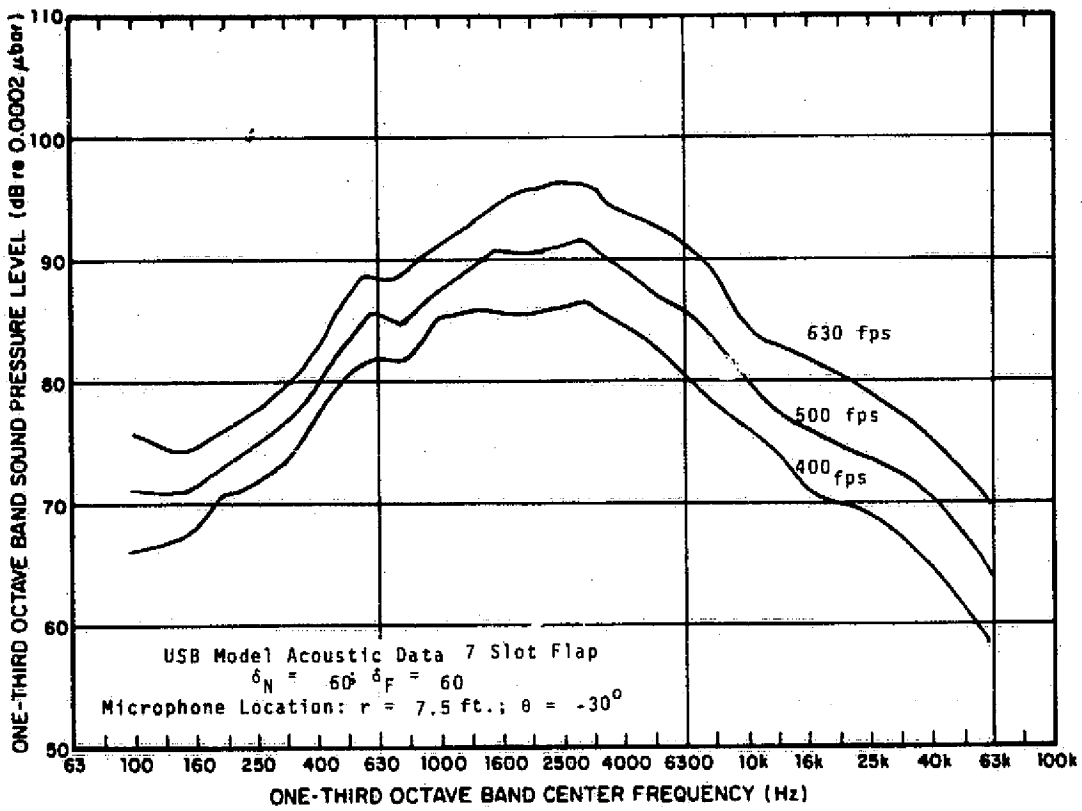

FIG. B- 19 RAW DATA FROM PROPULSIVE LIFT DEVICE MODEL TEST.

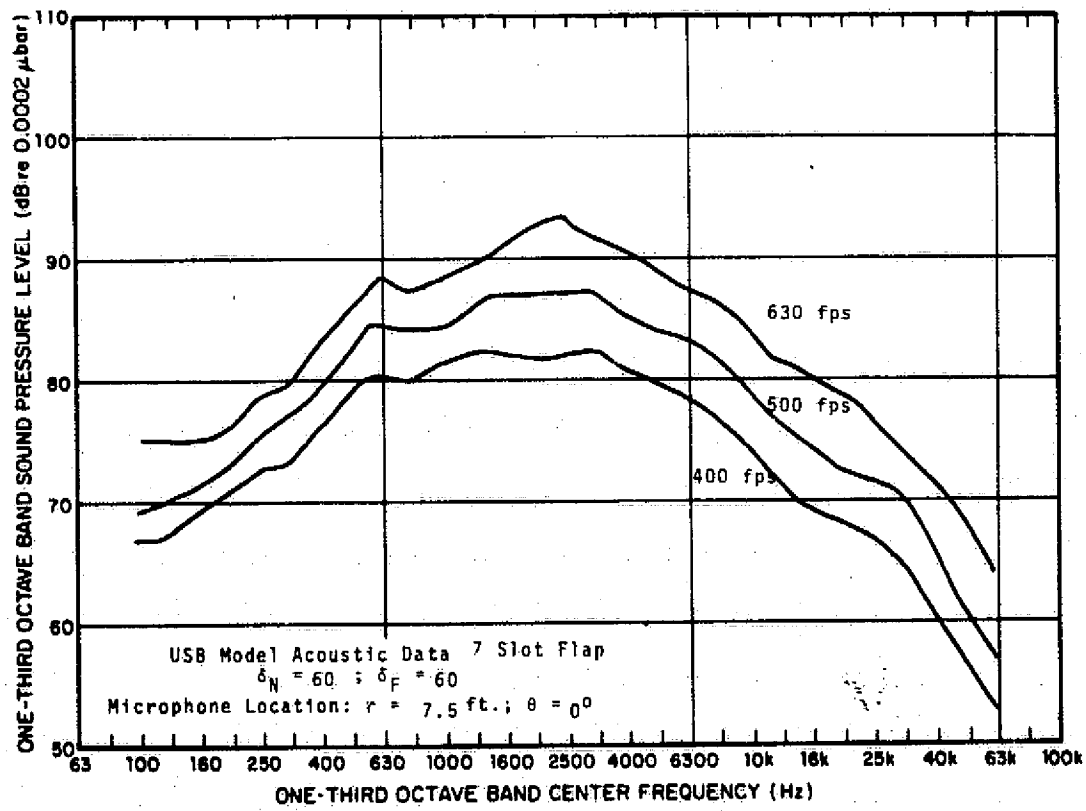

FIG. B- 20 RAW DATA FROM PROPULSIVE LIFT DEVICE MODEL TEST.

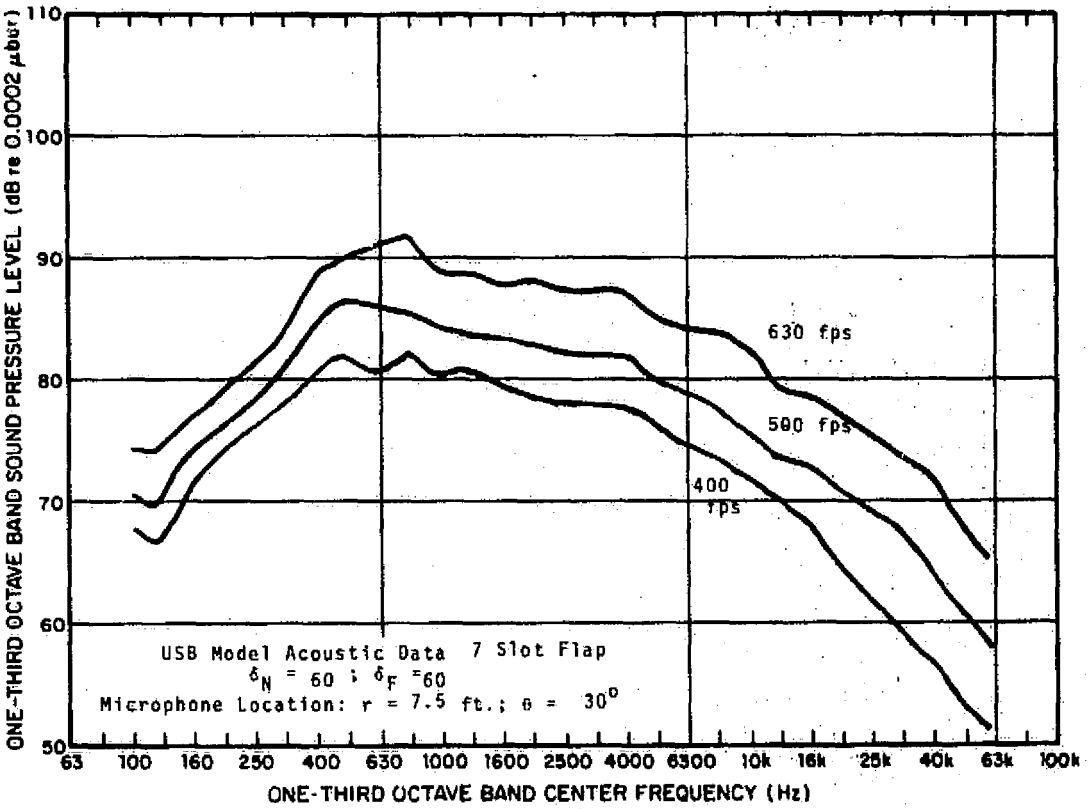

FIG. B- 21 RAW DATA FROM PROPULSIVE LIFT DEVICE MODEL TEST.

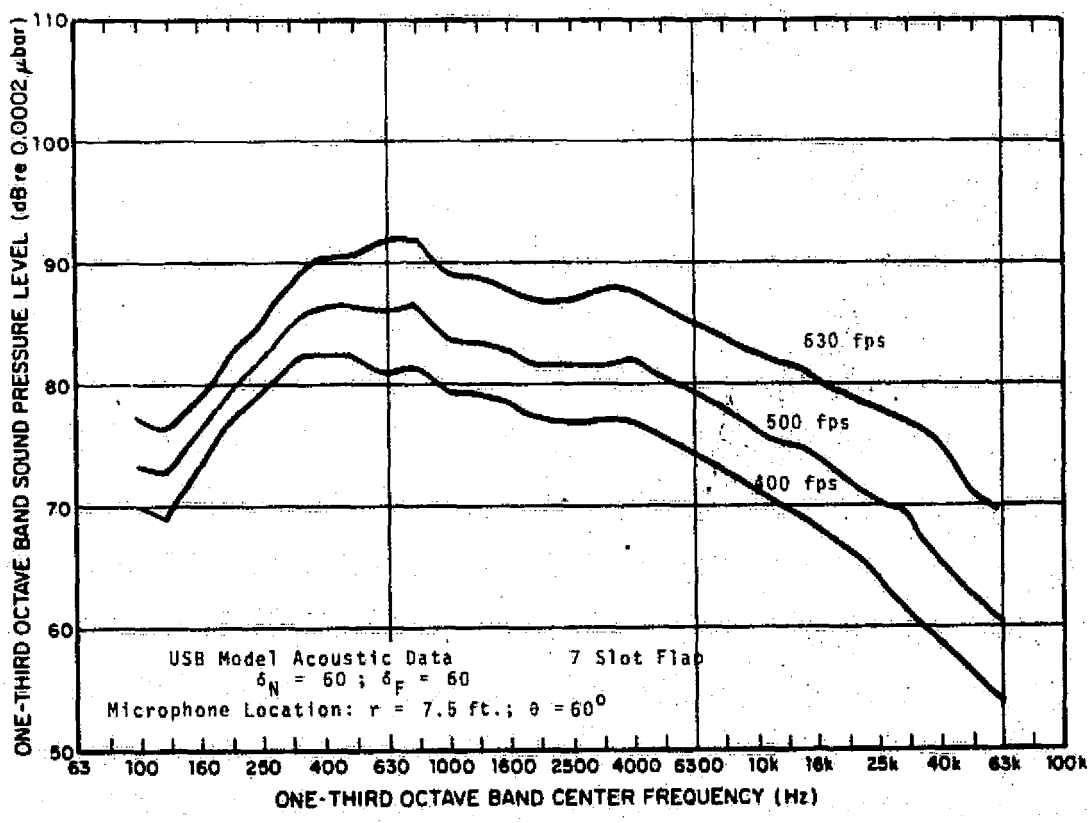

FIG. B- 22 RAW DATA FROM PROPULSIVE LIFT DEVICE MODEL TEST.

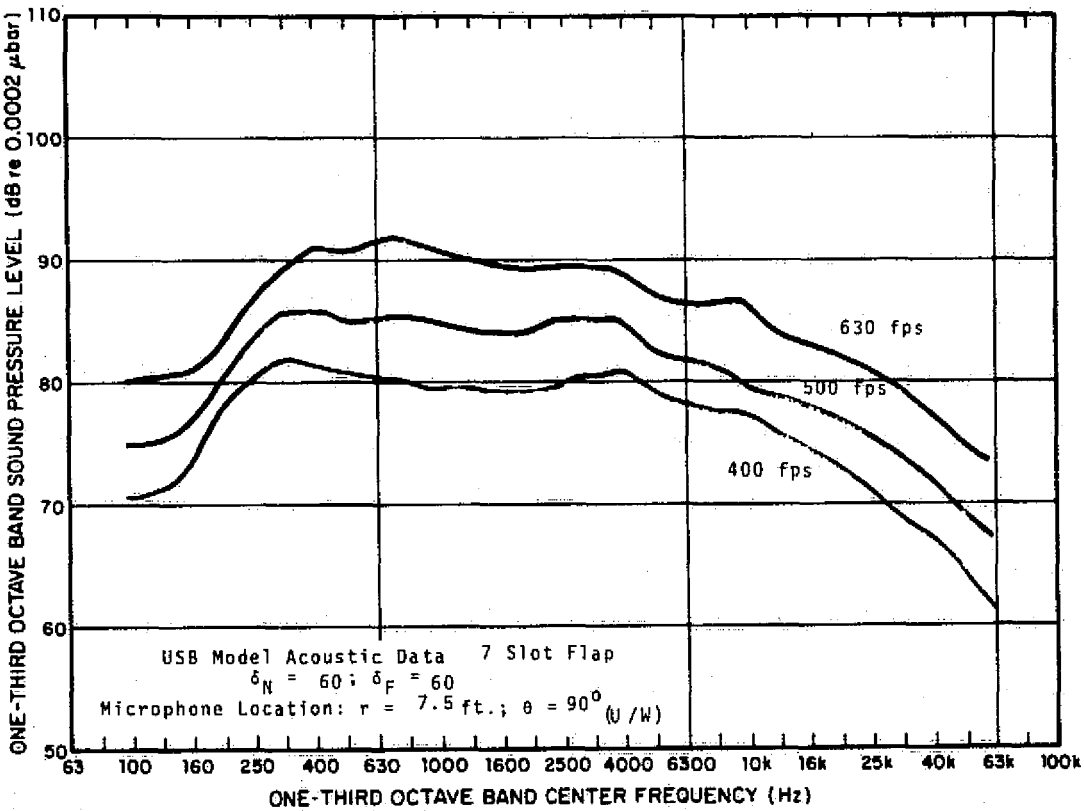

FIG. B- 23 RAW DATA FROM PROPULSIVE LIFT DEVICE MODEL TEST.

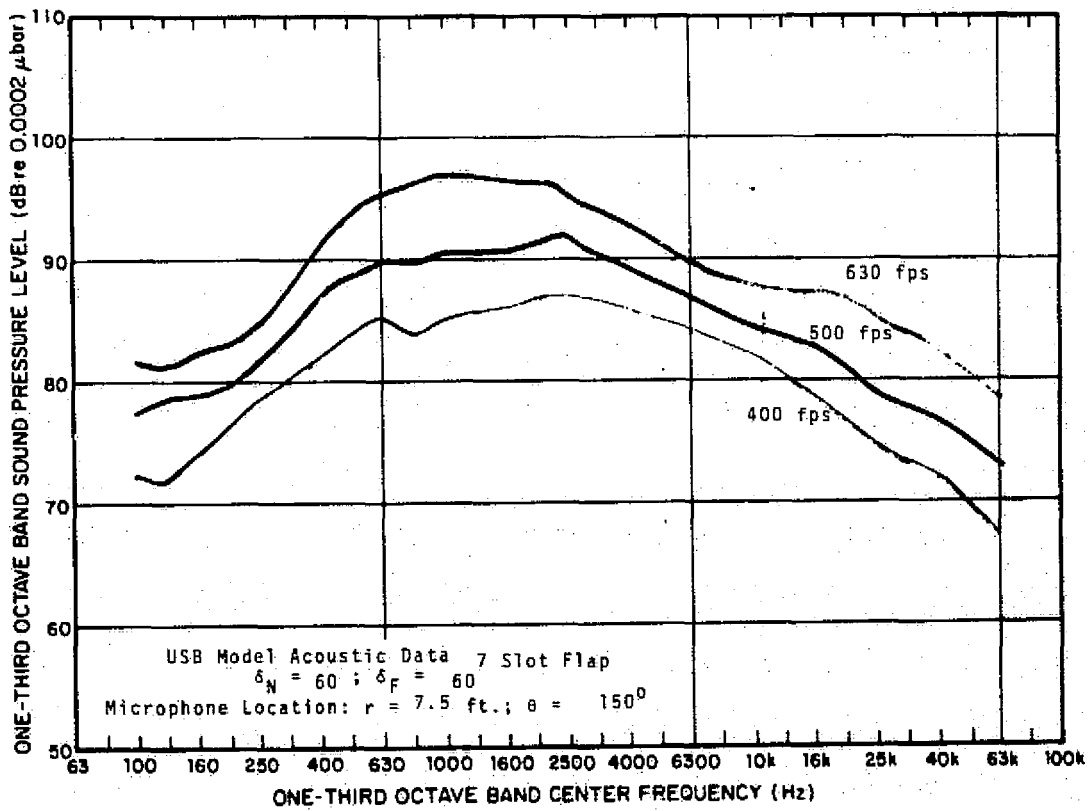

FIG. B- 24 RAW DATA FROM PROPULSIVE LIFT DEVICE MODEL TEST.

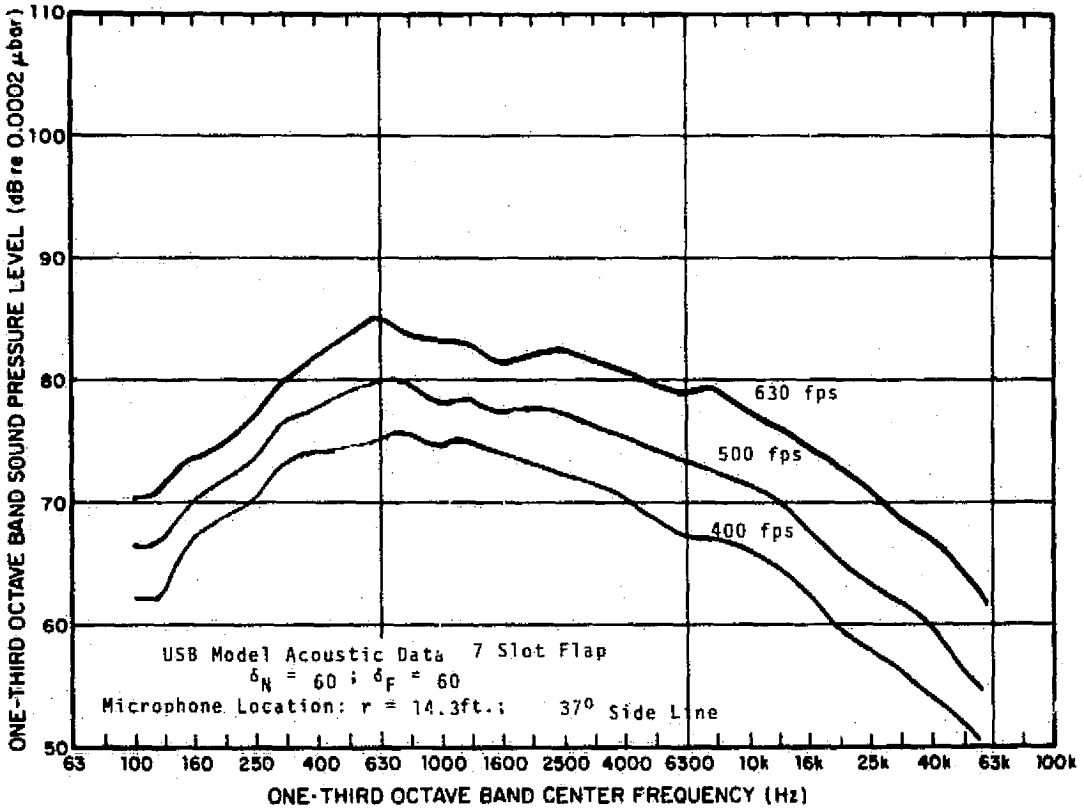

FIG. B- 25 RAW DATA FROM PROPULSIVE LIFT DEVICE MODEL TEST.

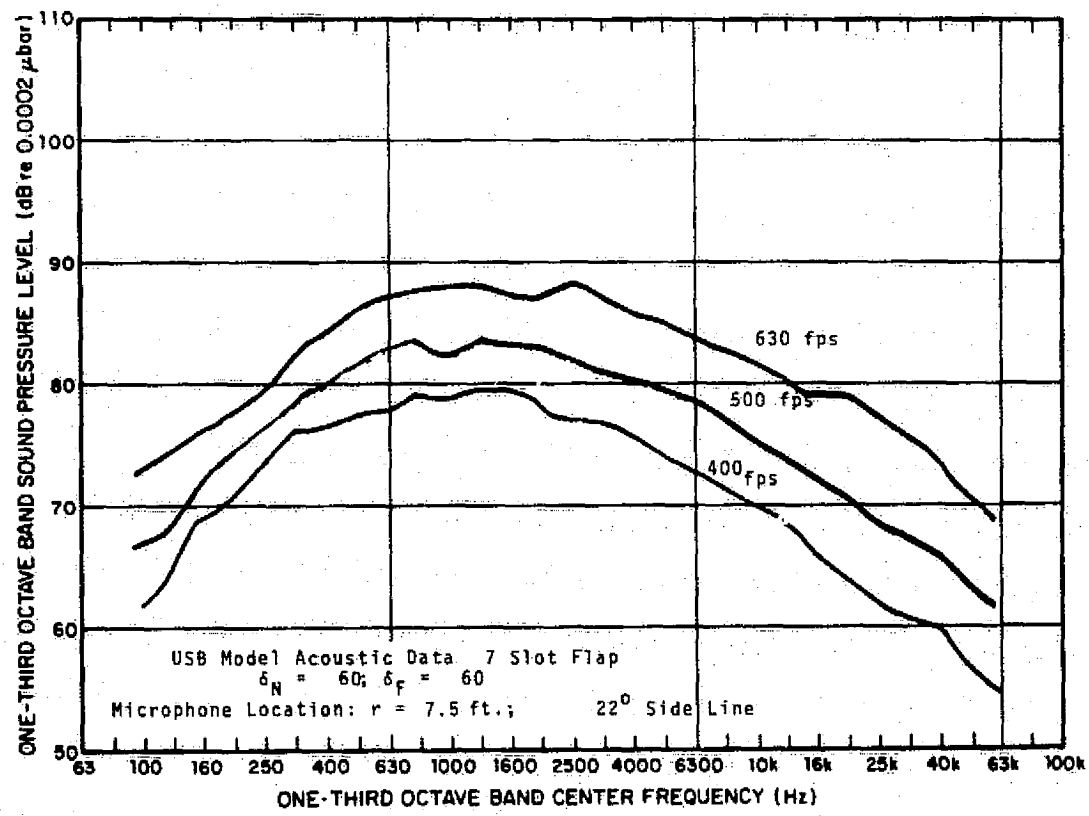

FIG. B- 26 RAW DATA FROM PROPULSIVE LIFT DEVICE MODEL TEST.

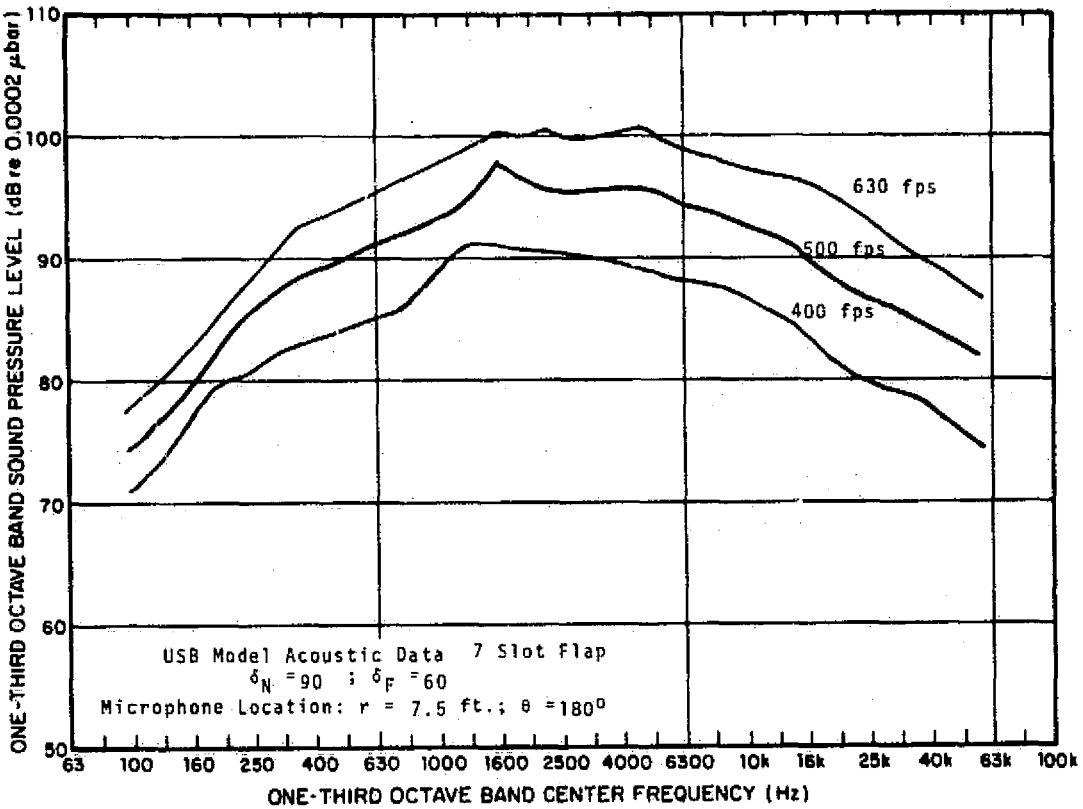

FIG. B- 27 RAW DATA FROM PROPULSIVE LIFT DEVICE MODEL TEST.

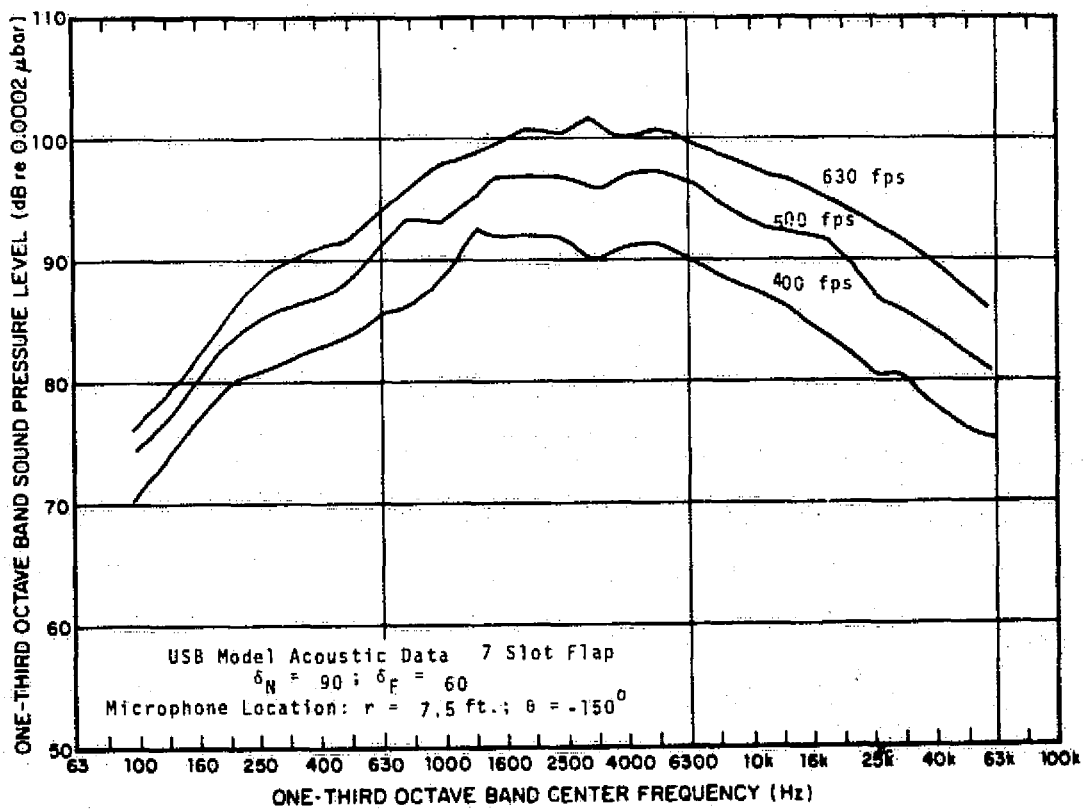

FIG. B- 28 RAW DATA FROM PROPULSIVE LIFT DEVICE MODEL TEST.

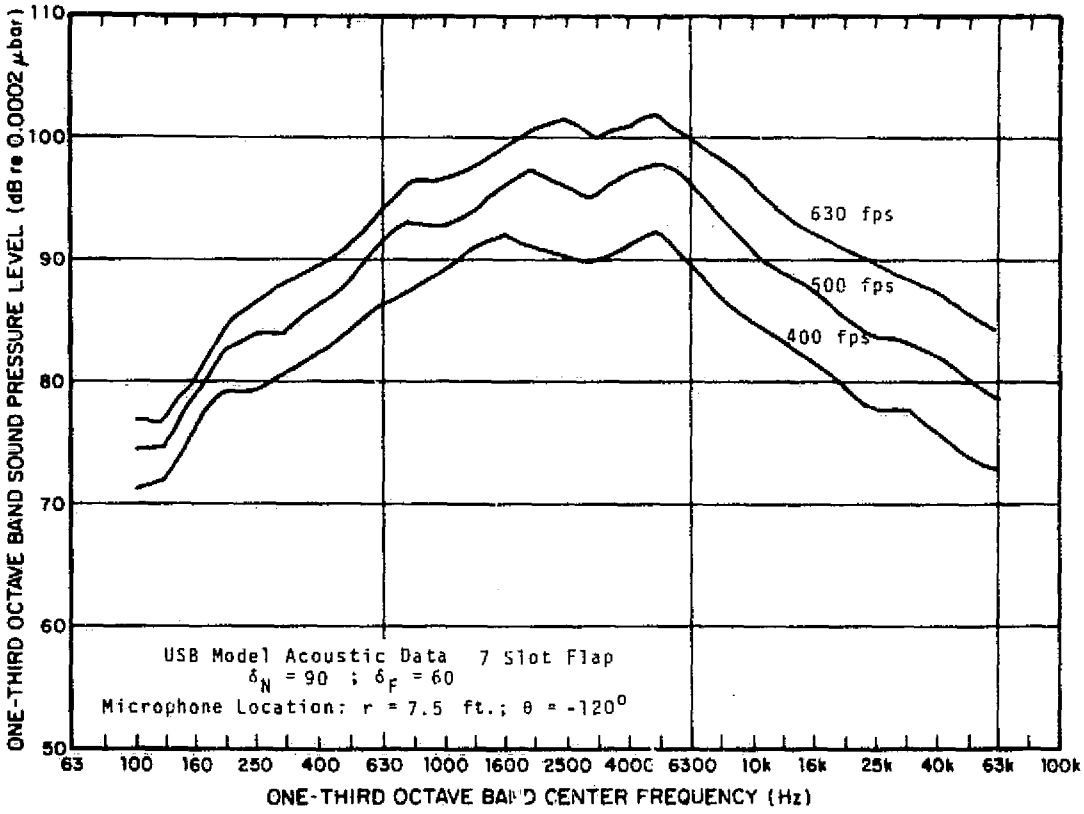

FIG. B- 29 RAW DATA FROM PROPULSIVE LIFT DEVICE MODEL TEST.

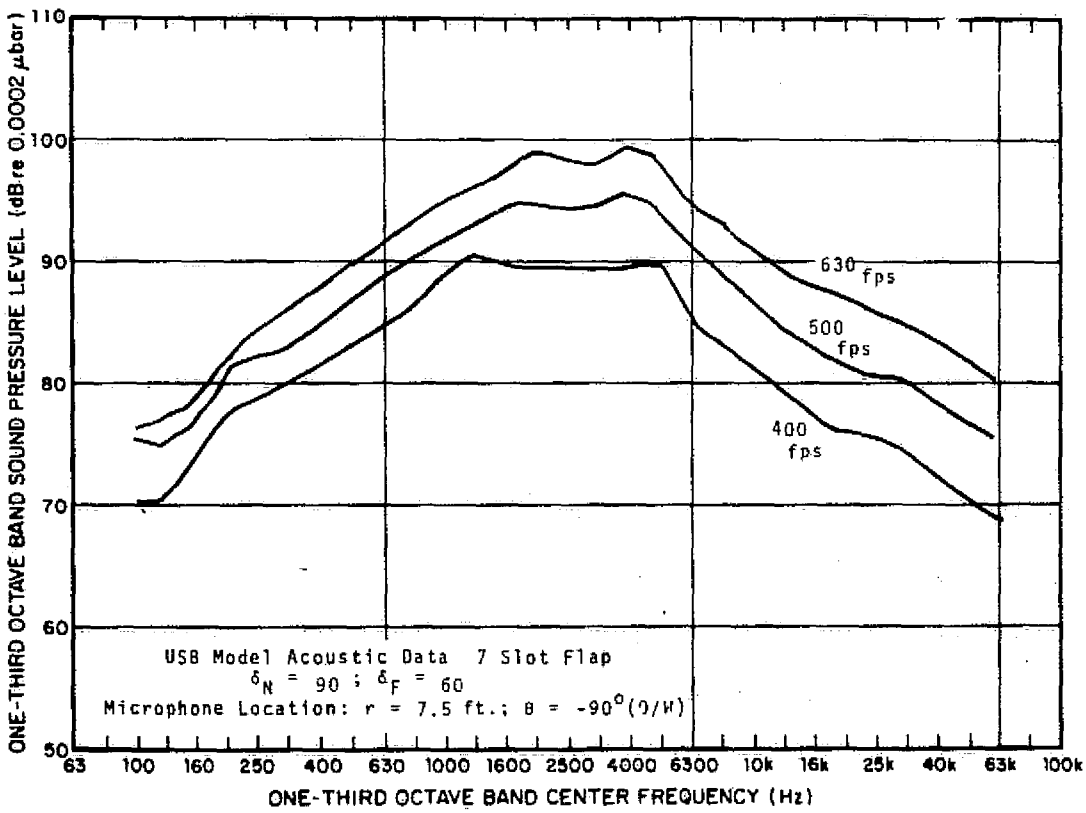

FIG. B- 30 RAW DATA FROM PROPULSIVE LIFT DEVICE MODEL TEST.

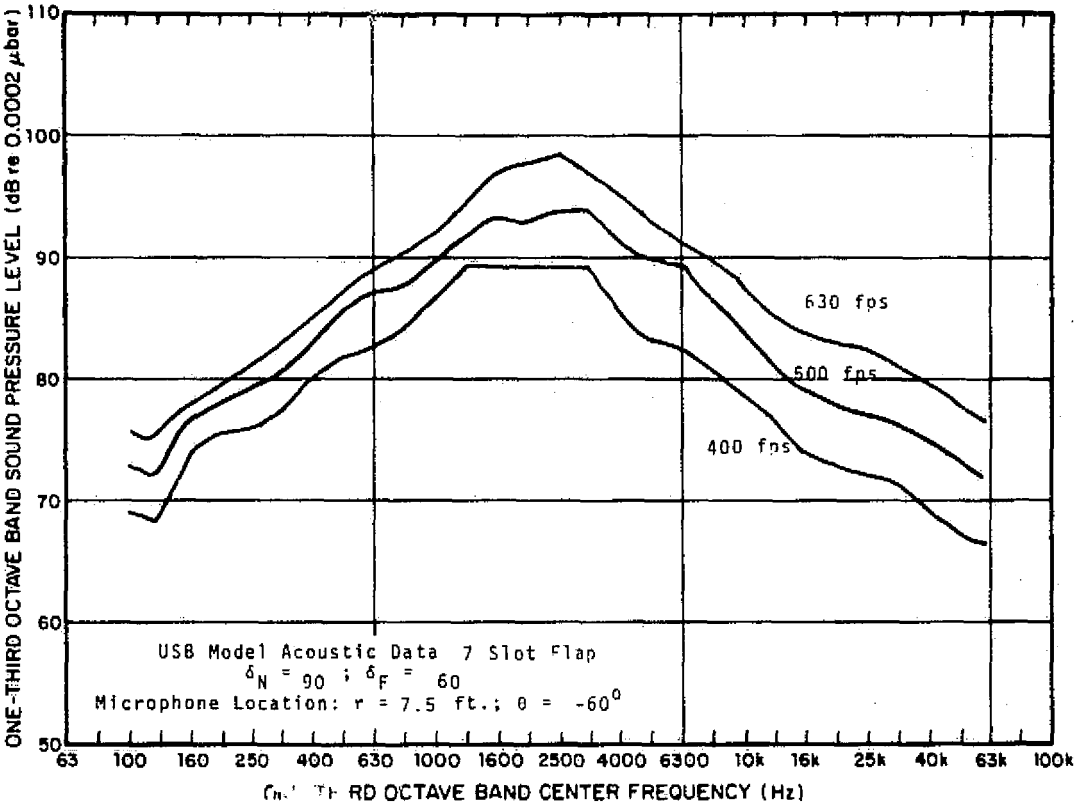

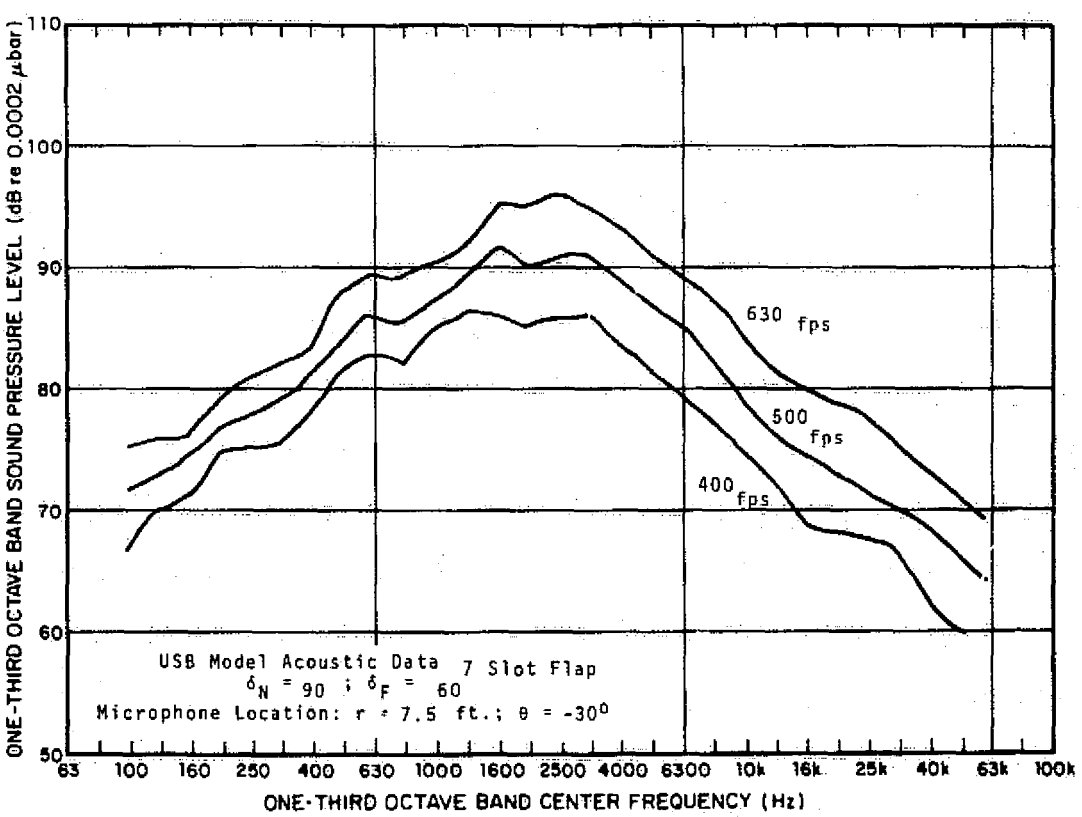

FIG. B- 32 RAW DATA FROM PROPULSIVE LIFT DEVICE MODEL TEST.

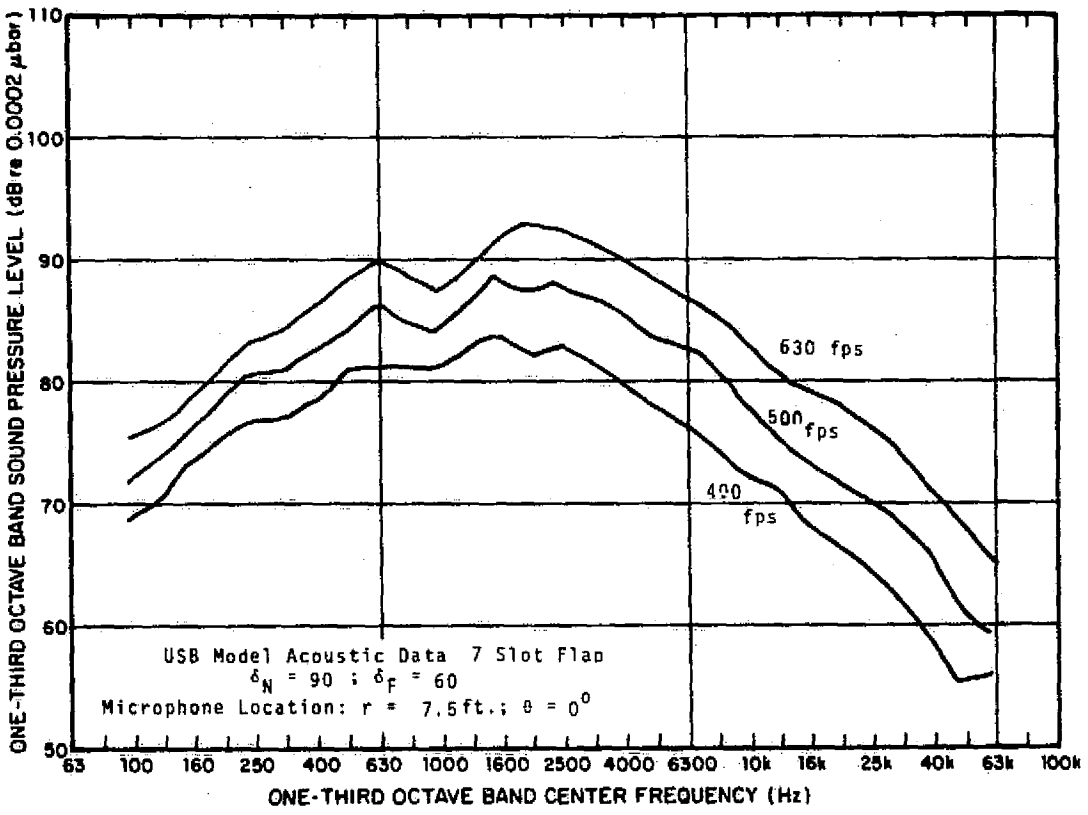

FIG. B- 33 RAW DATA FROM PROPULSIVE LIFT DEVICE MODEL TEST.

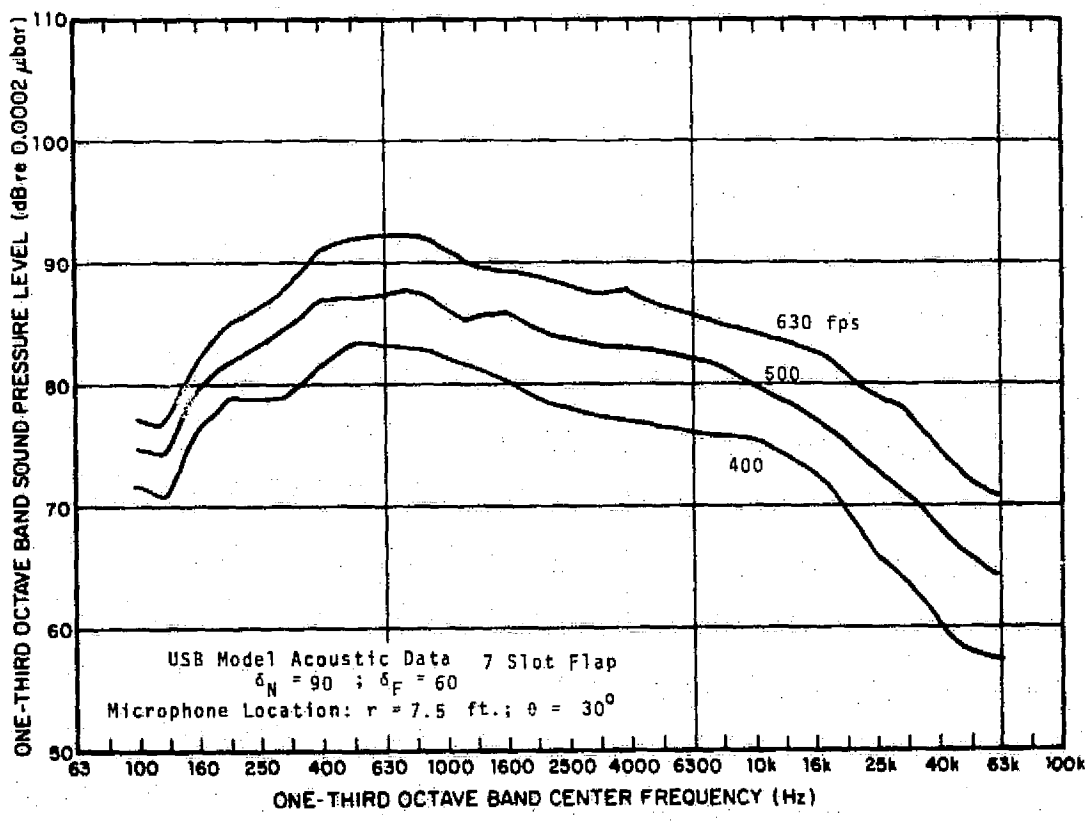

FIG. B- 34 RAW DATA FROM PROPULSIVE LIFT DEVICE MODEL TEST.

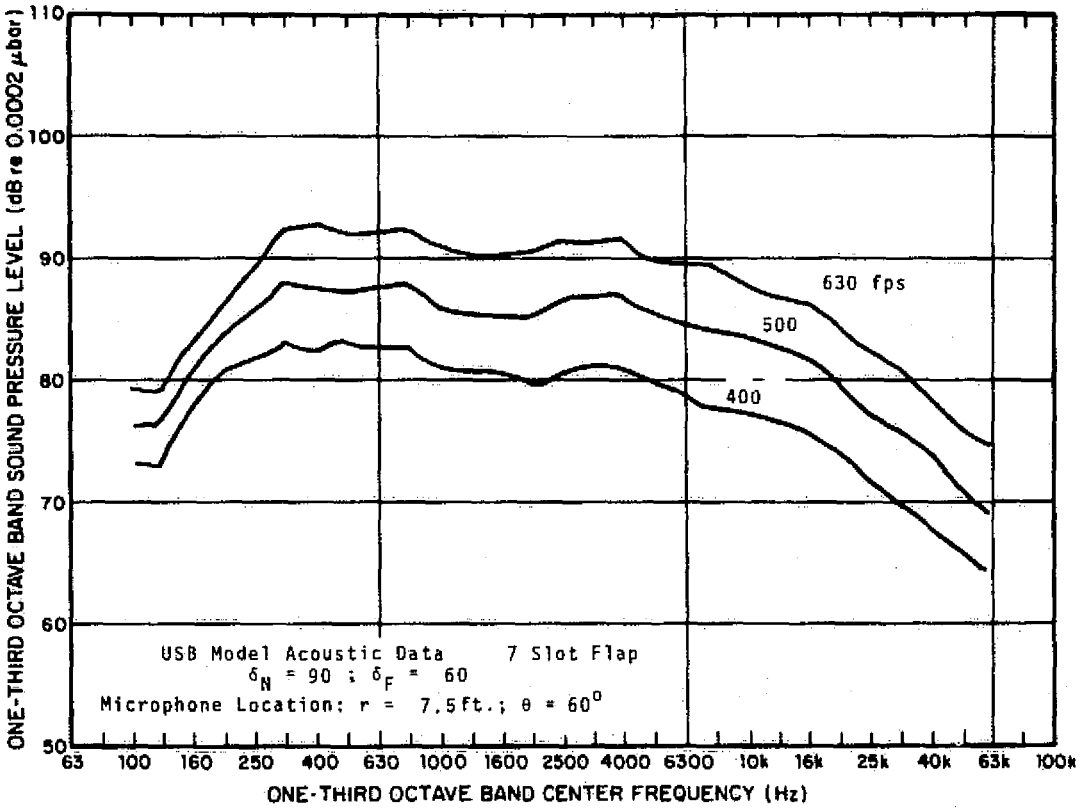

FIG. B- 35 RAW DATA FROM PROPULSIVE LIFT DEVICE MODEL TEST.

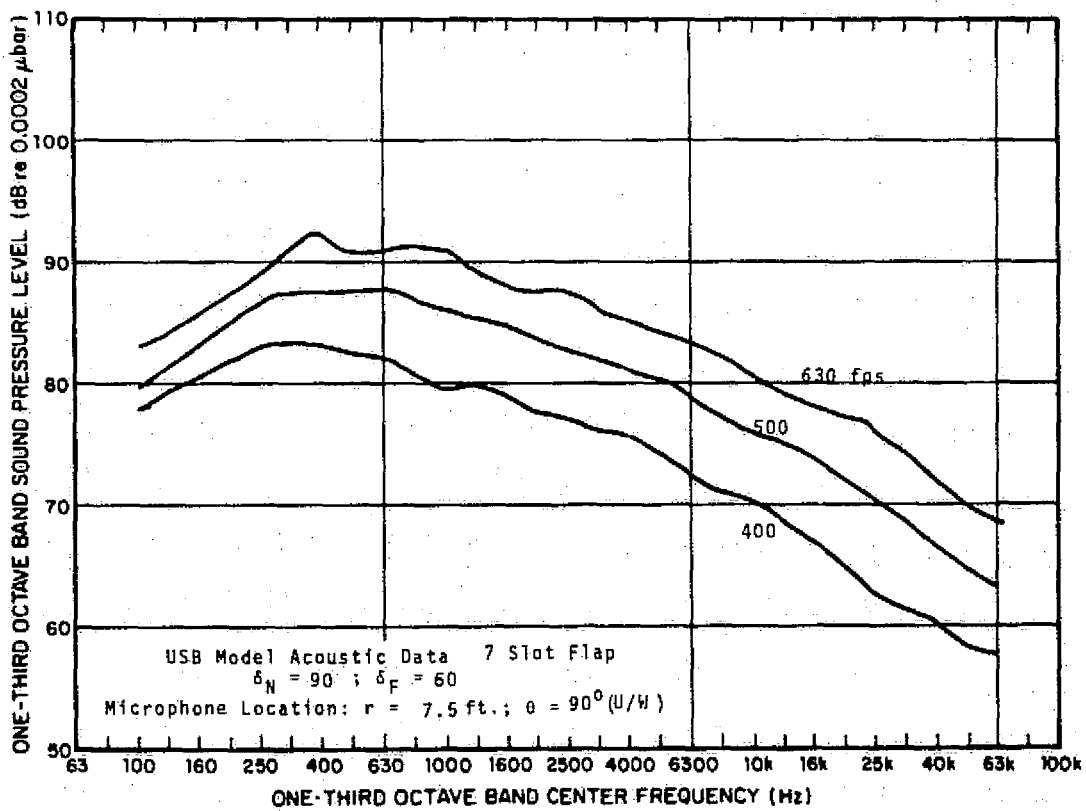

FIG. B- 36 RAW DATA FROM PROPULSIVE LIFT DEVICE MODEL TEST.

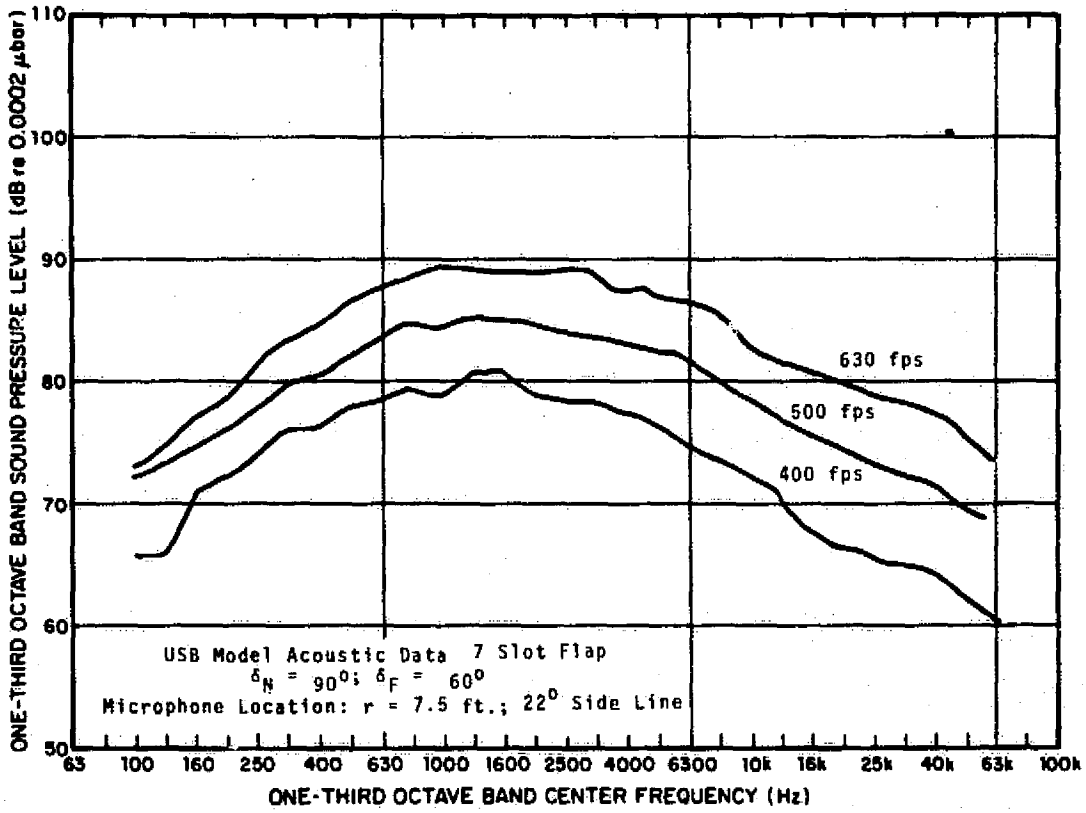

FIG. B- 37 RAW DATA FROM PROPULSIVE LIFT DEVICE MODEL TEST.

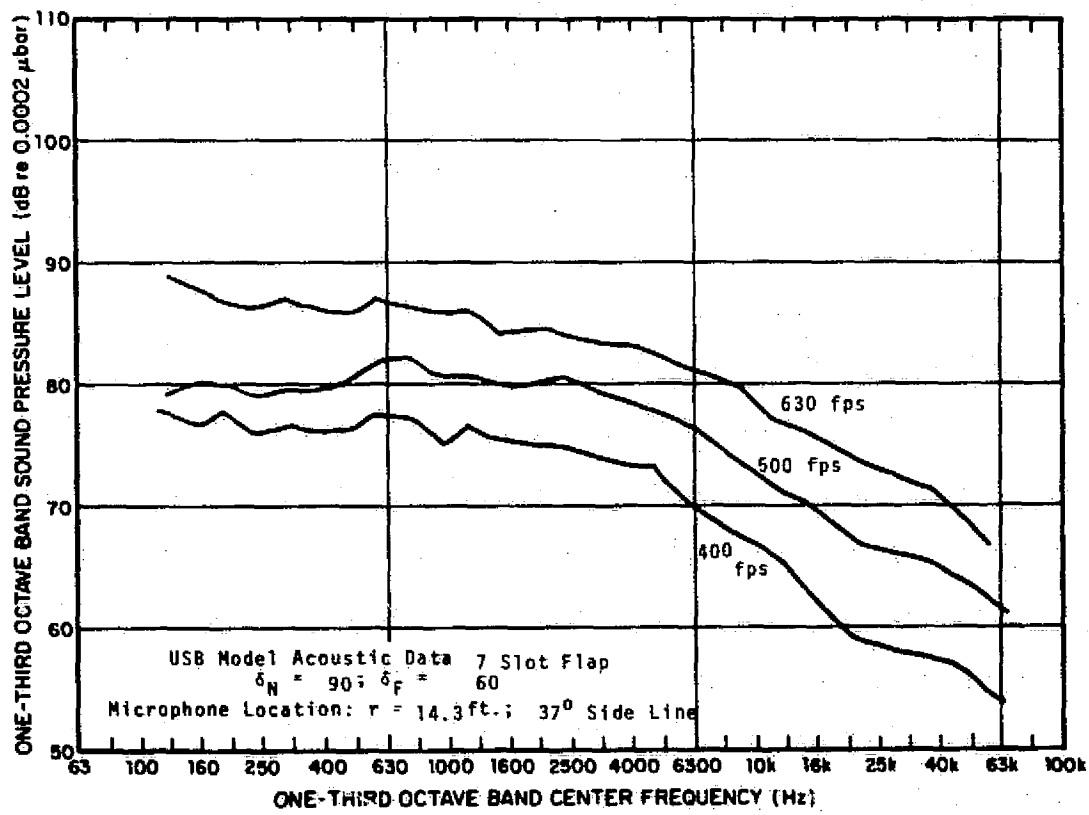

FIG. B- 38 RAW DATA FROM PROPULSIVE LIFT DEVICE MODEL TEST.

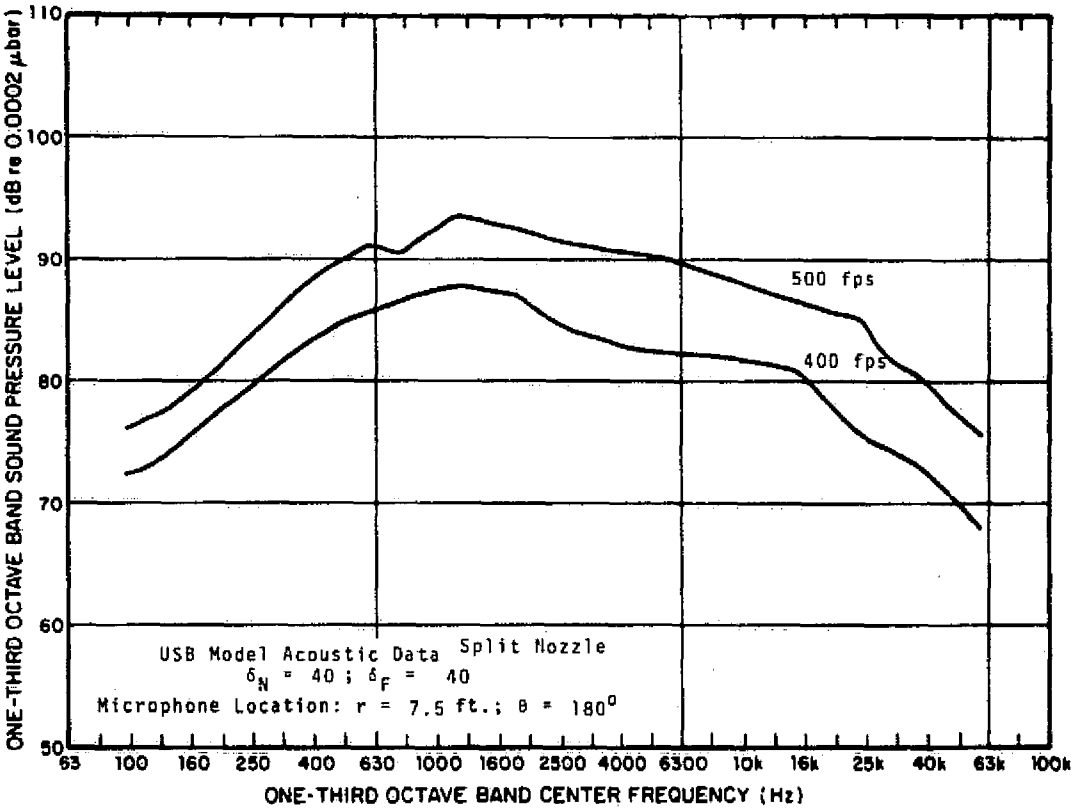

FIG. B- 39 RAW DATA FROM PROPULSIVE LIFT DEVICE MODEL TEST.

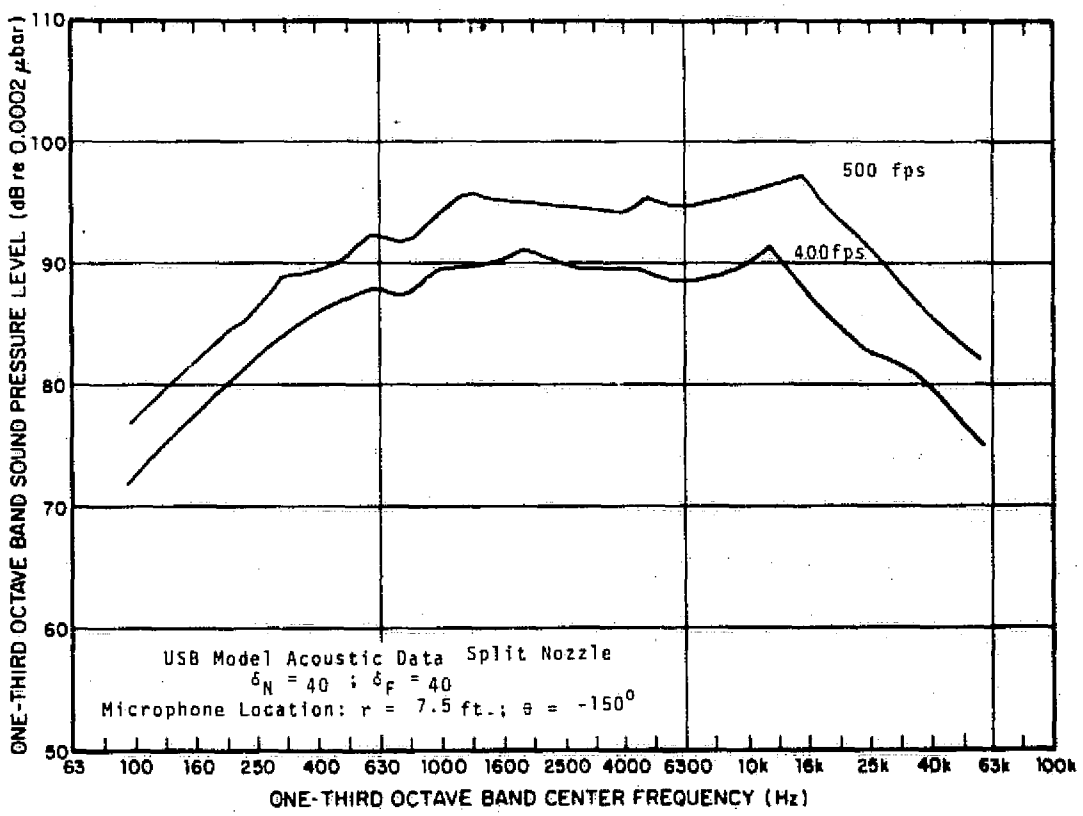

FIG. B- 40 RAW DATA FROM PROPULSIVE LIFT DEVICE MODEL TEST.

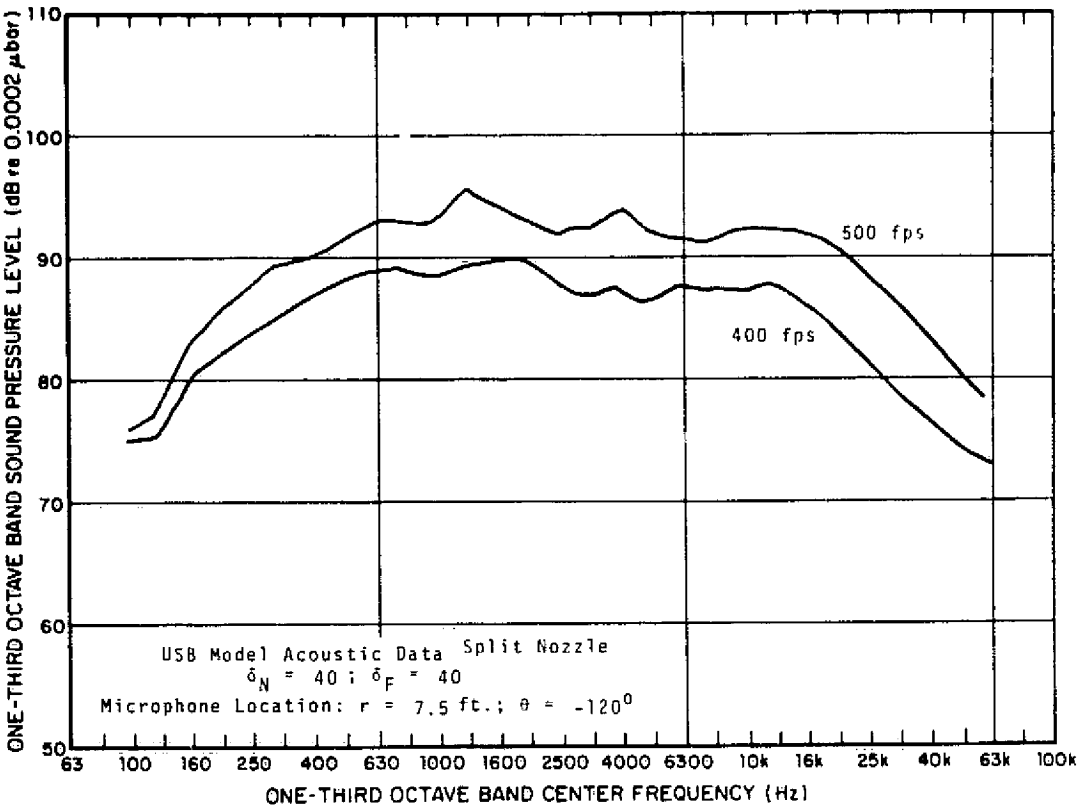

FIG. B- 41 RAW DATA FROM PROPULSIVE LIFT DEVICE MODEL TEST.

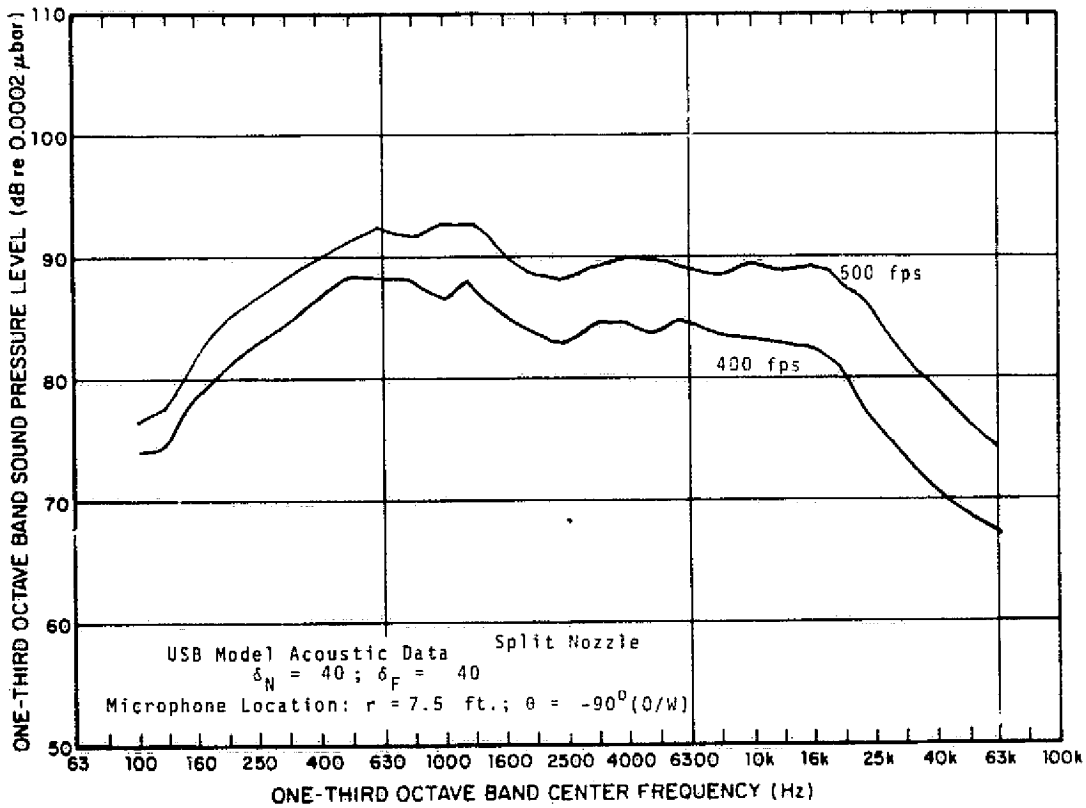

FIG. B- 42 RAW DATA FROM PROPULSIVE LIFT DEVICE MODEL TEST.

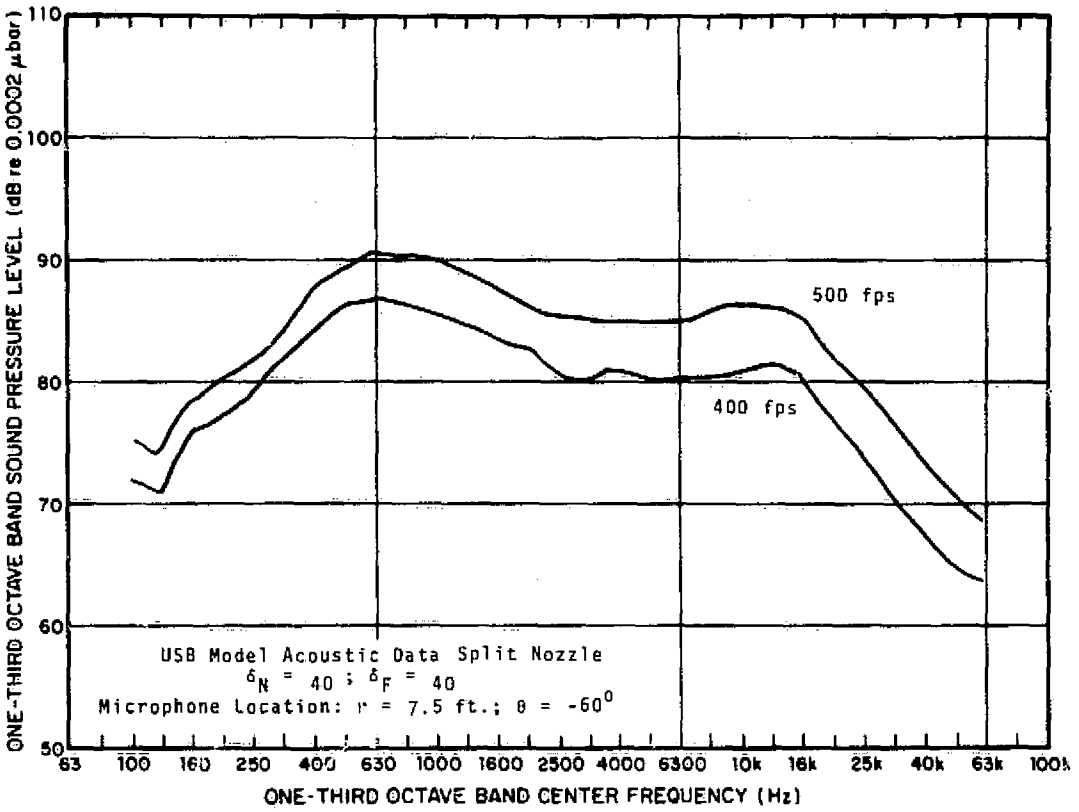

FIG. B- 43 RAW DATA FROM PROPULSIVE LIFT DEVICE MODEL TEST.

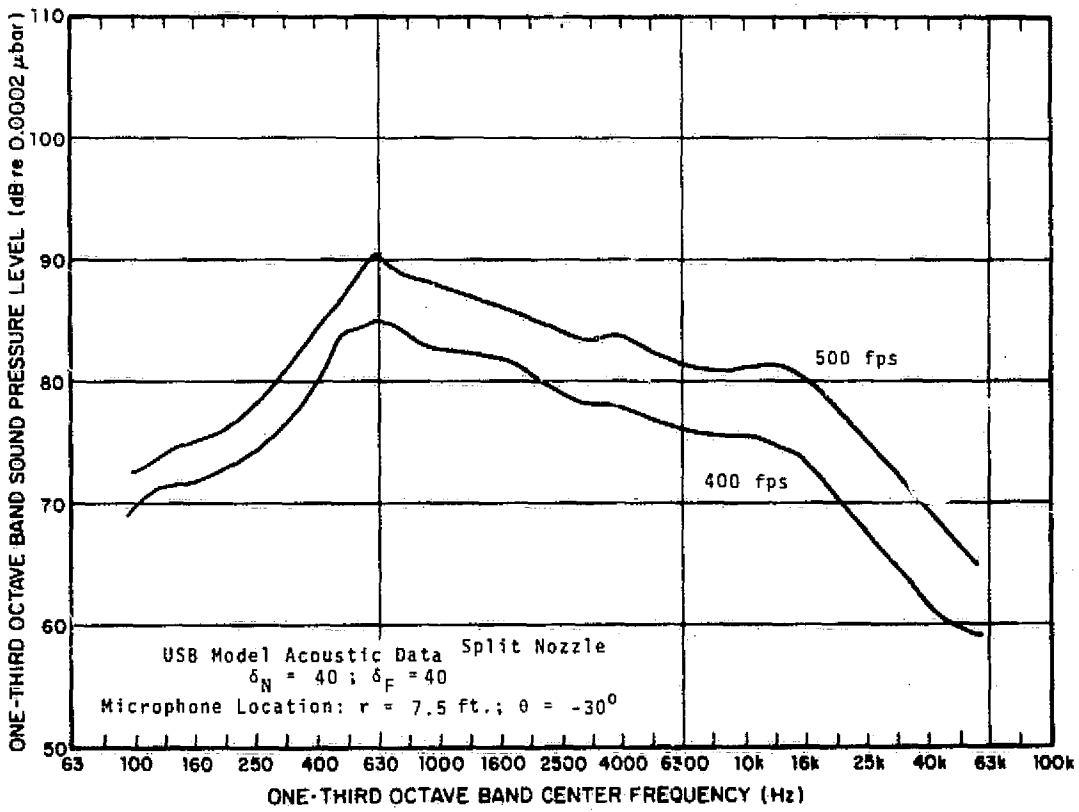

FIG. B- 44 RAW DATA FROM PROPULSIVE LIFT DEVICE MODEL TEST.

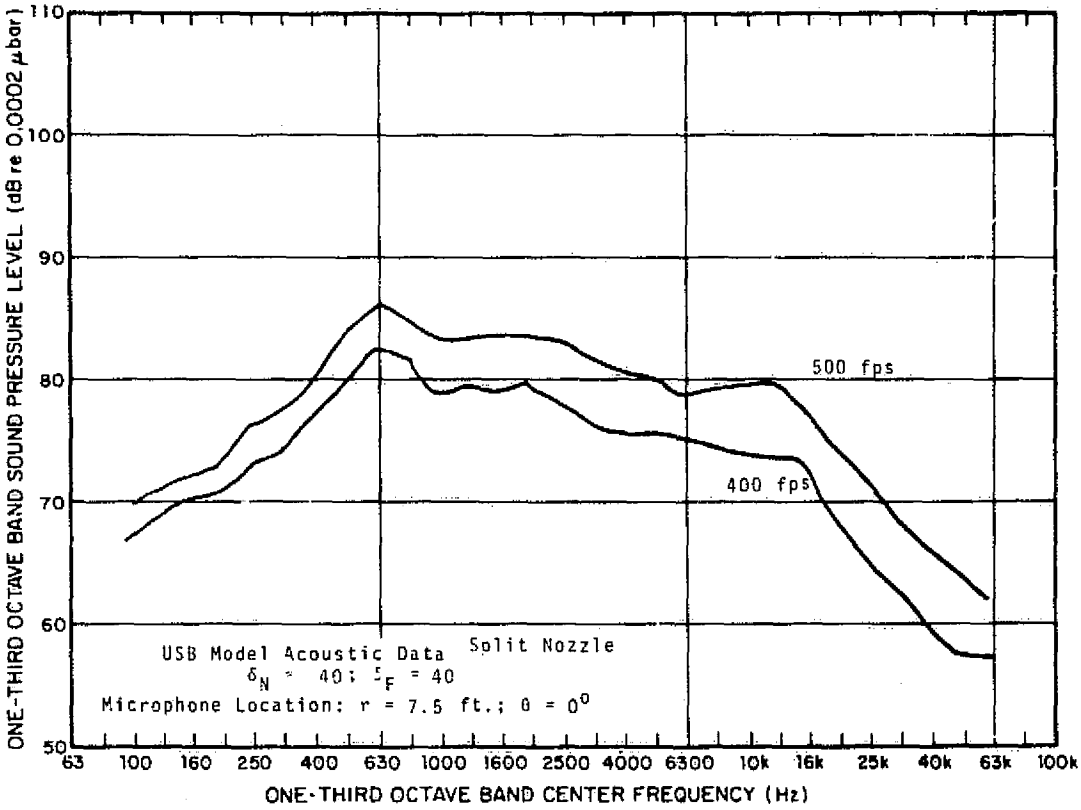

FIG. B- 45 RAW DATA FROM PROPULSIVE LIFT DEVICE MODEL TEST.

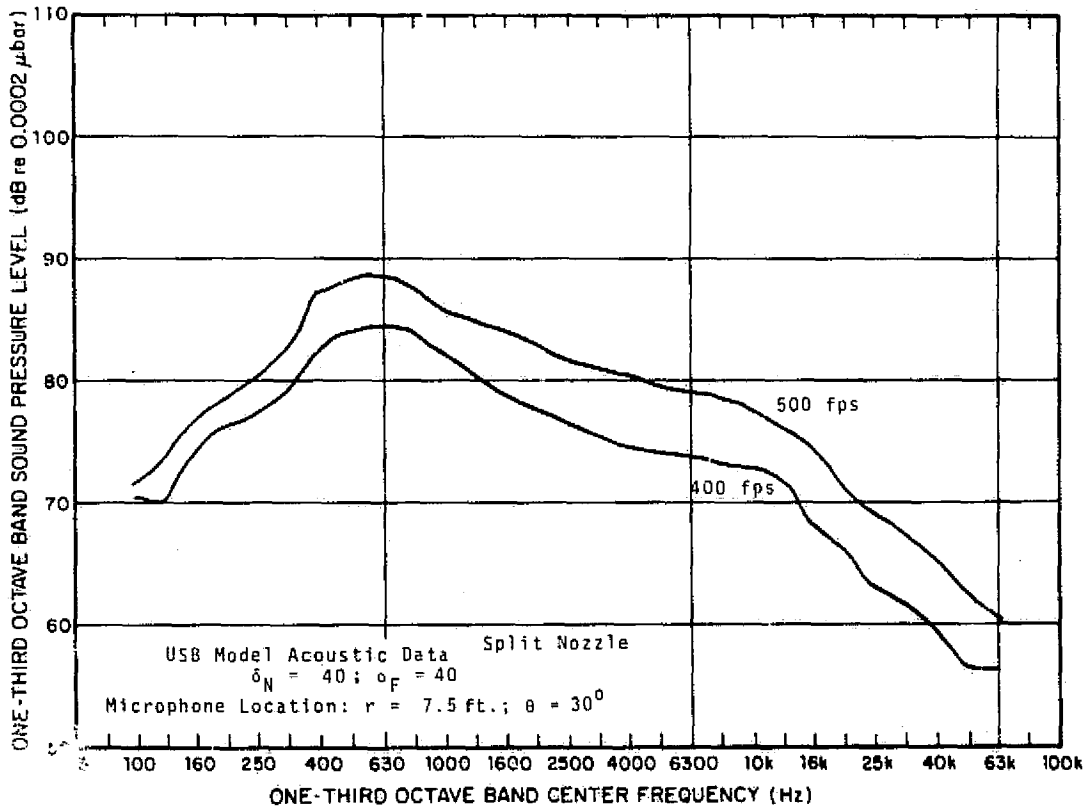

FIG. B- 46 RAW DATA FROM PROPULSIVE LIFT DEVICE MODEL TEST.

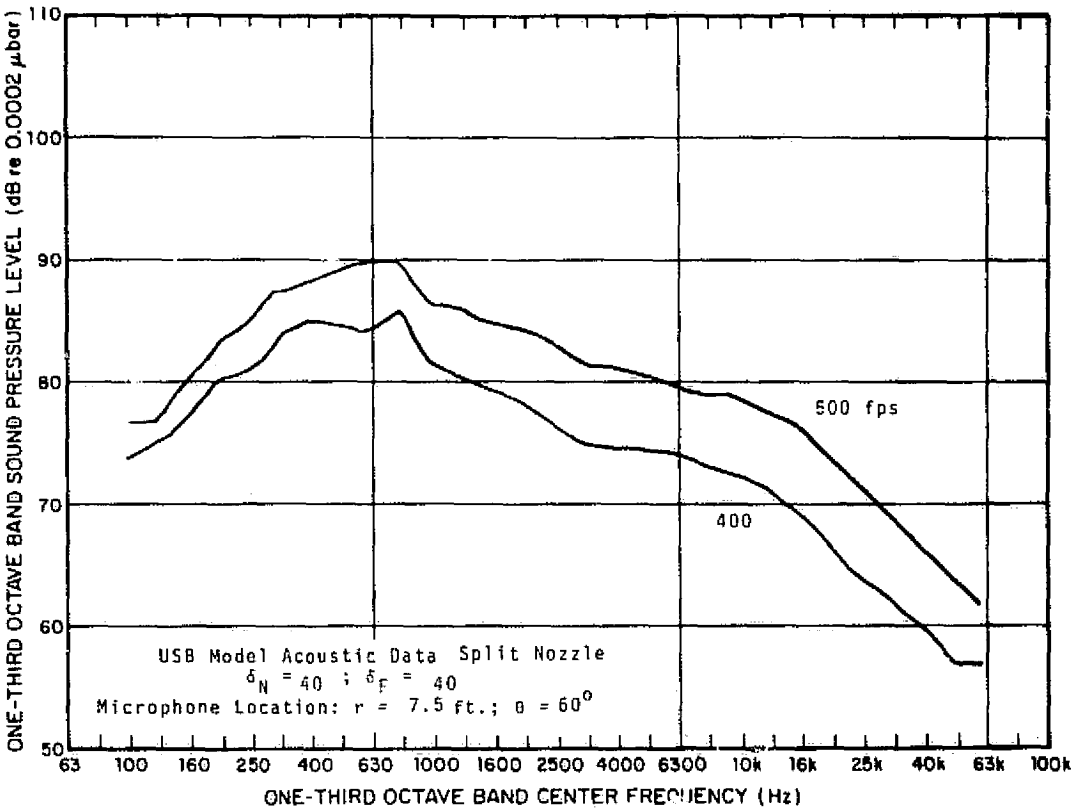

FIG. B- 47 RAW DATA FROM PROPULSIVE LIFT DEVICE MODEL TEST.

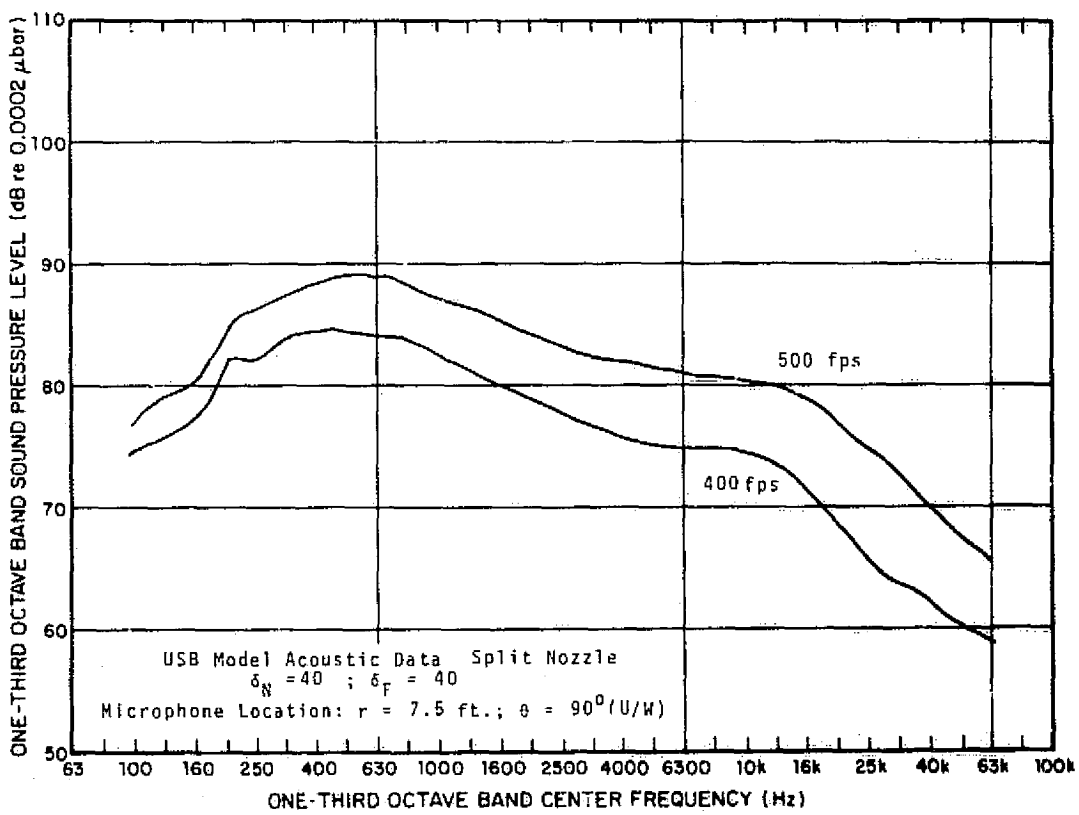

FIG. B-48 RAW DATA FROM PROPULSIVE LIFT DEVICE MODEL TEST.

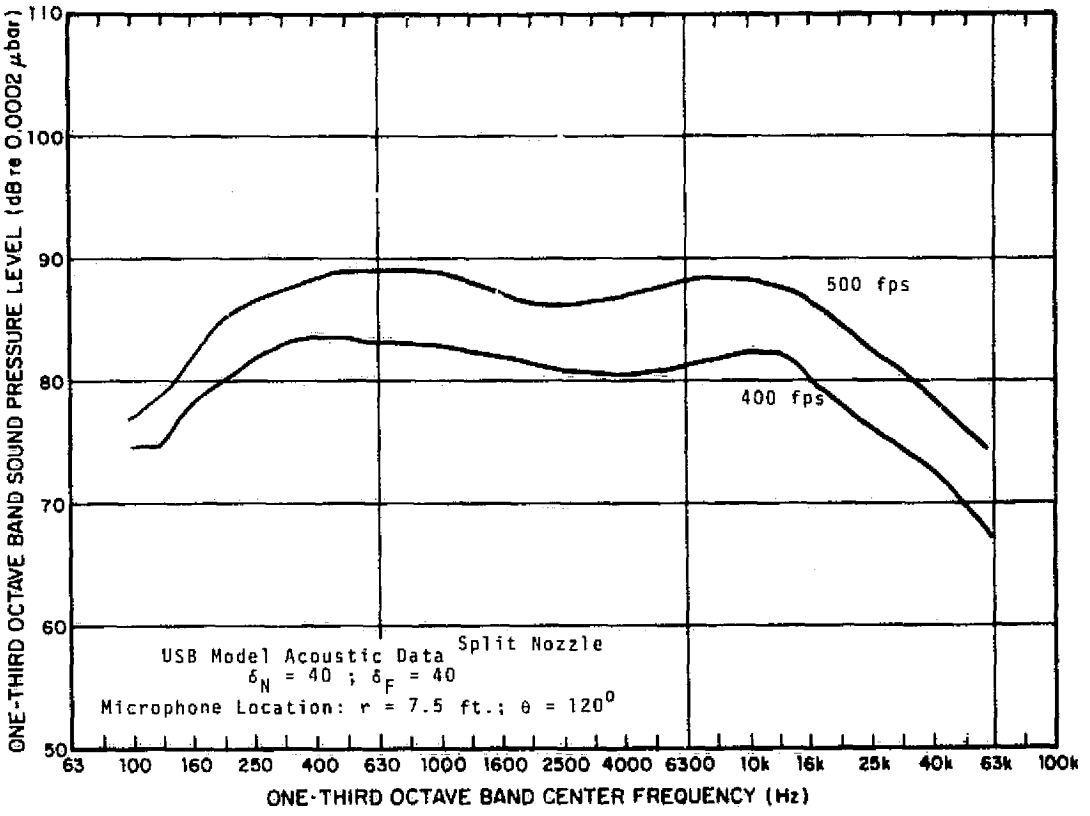

FIG. B- 49 RAW DATA FROM PROPULSIVE LIFT DEVICE MODEL TEST.

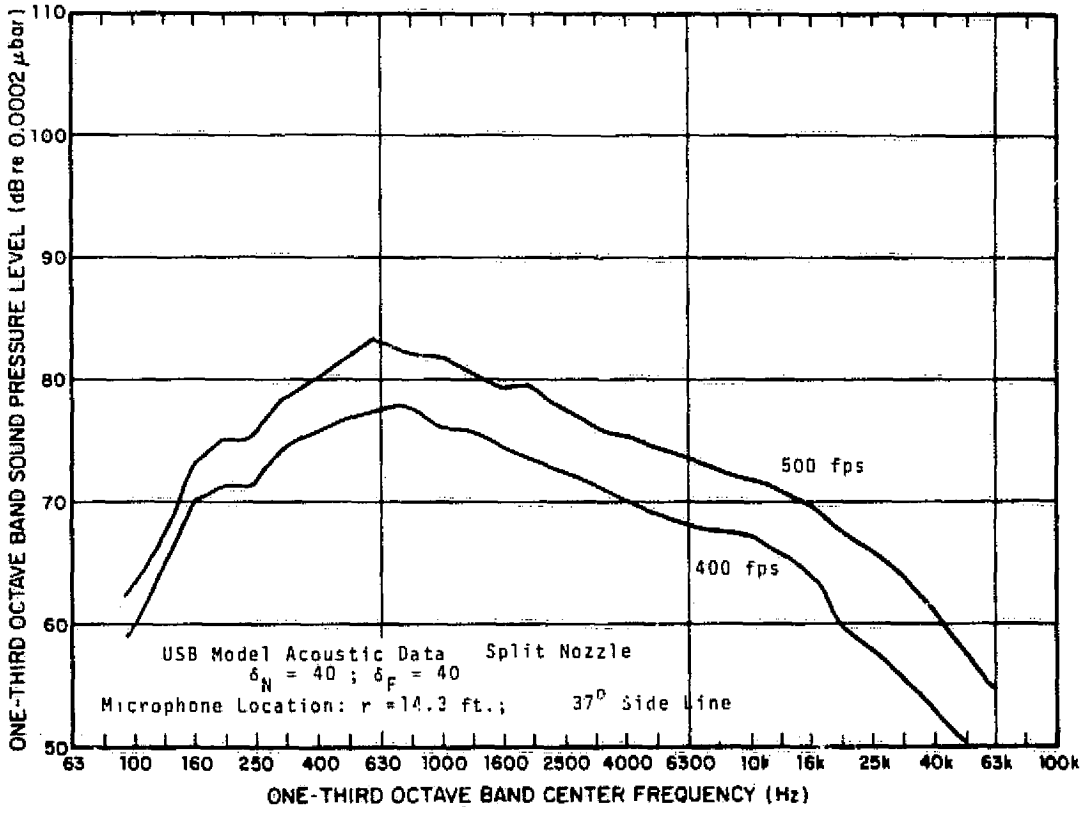

FIG. B- 50 RAW DATA FROM PROPULSIVE LIFT DEVICE MODEL TEST.

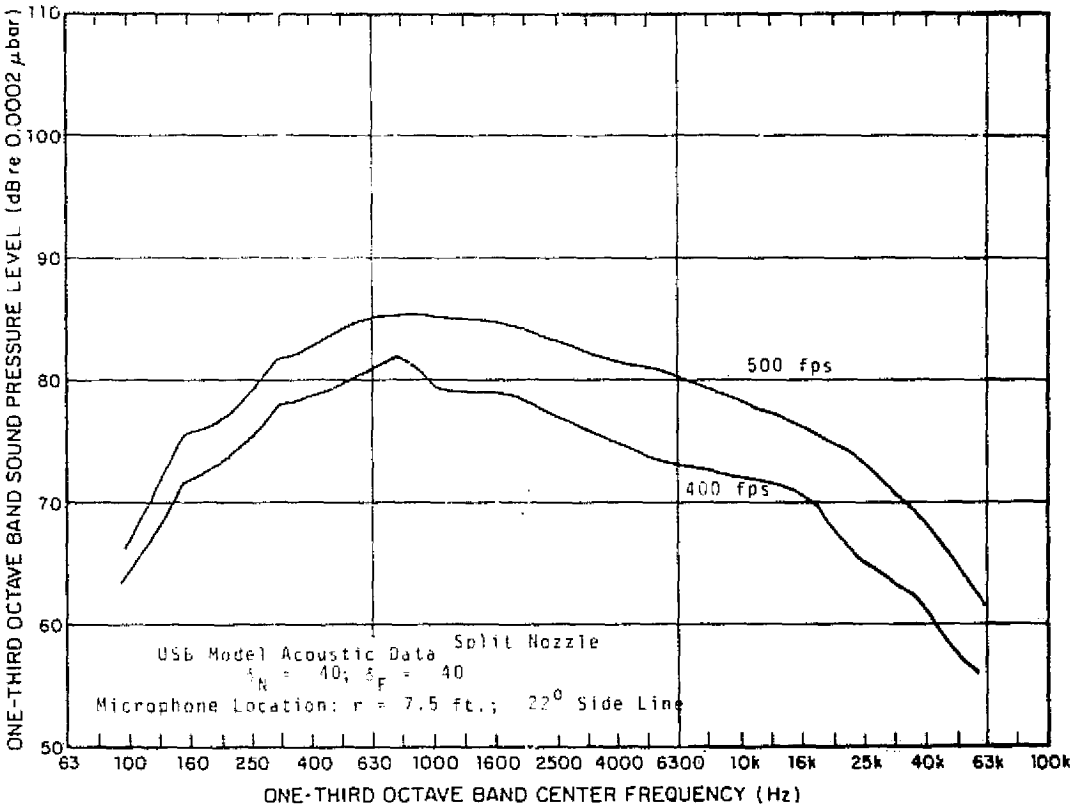

FIG. B- 51 RAW DATA FROM PROPULSIVE LIFT DEVICE MODEL TEST.

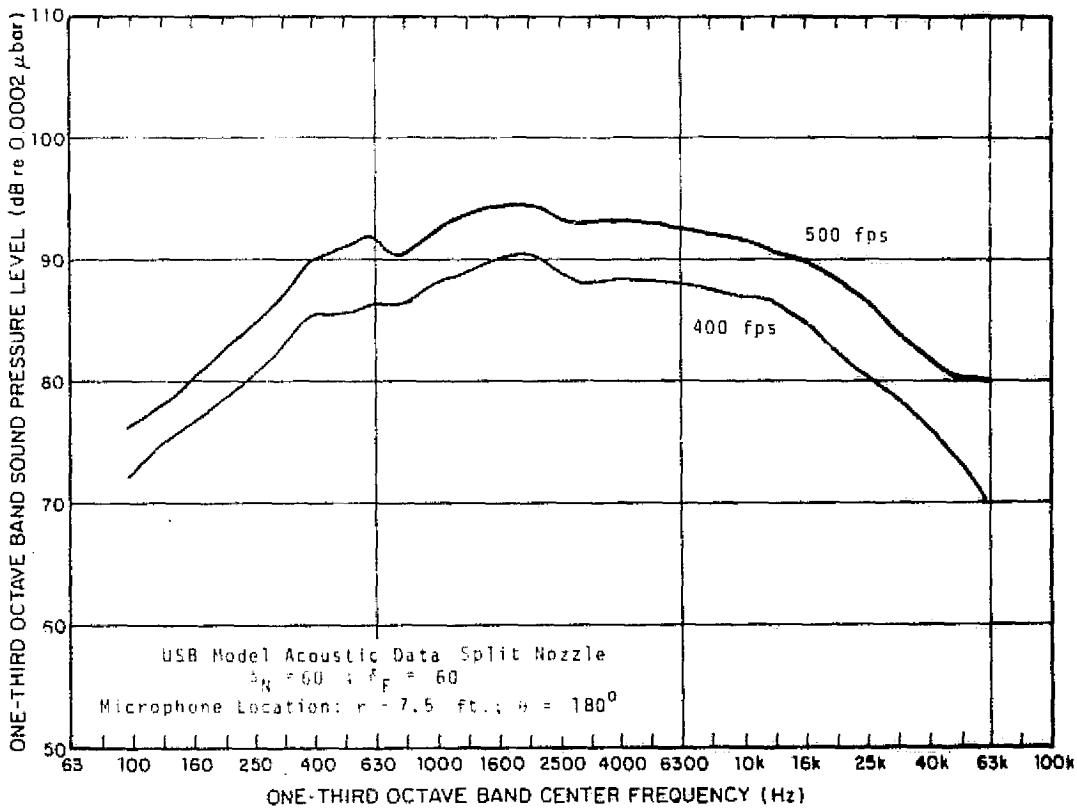

FIG. B-52 RAW DATA FROM PROPULSIVE LIFT DEVICE MODEL TEST.

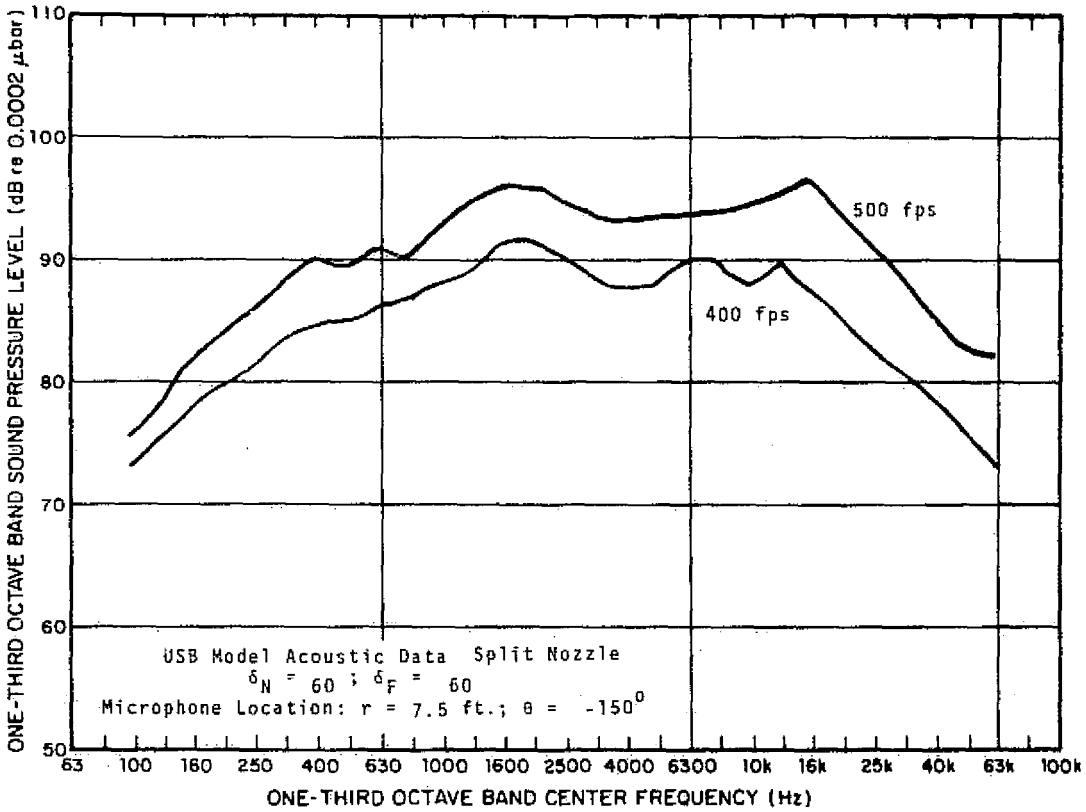

FIG. B- 53 RAW DATA FROM PROPULSIVE LIFT DEVICE MODEL TEST.

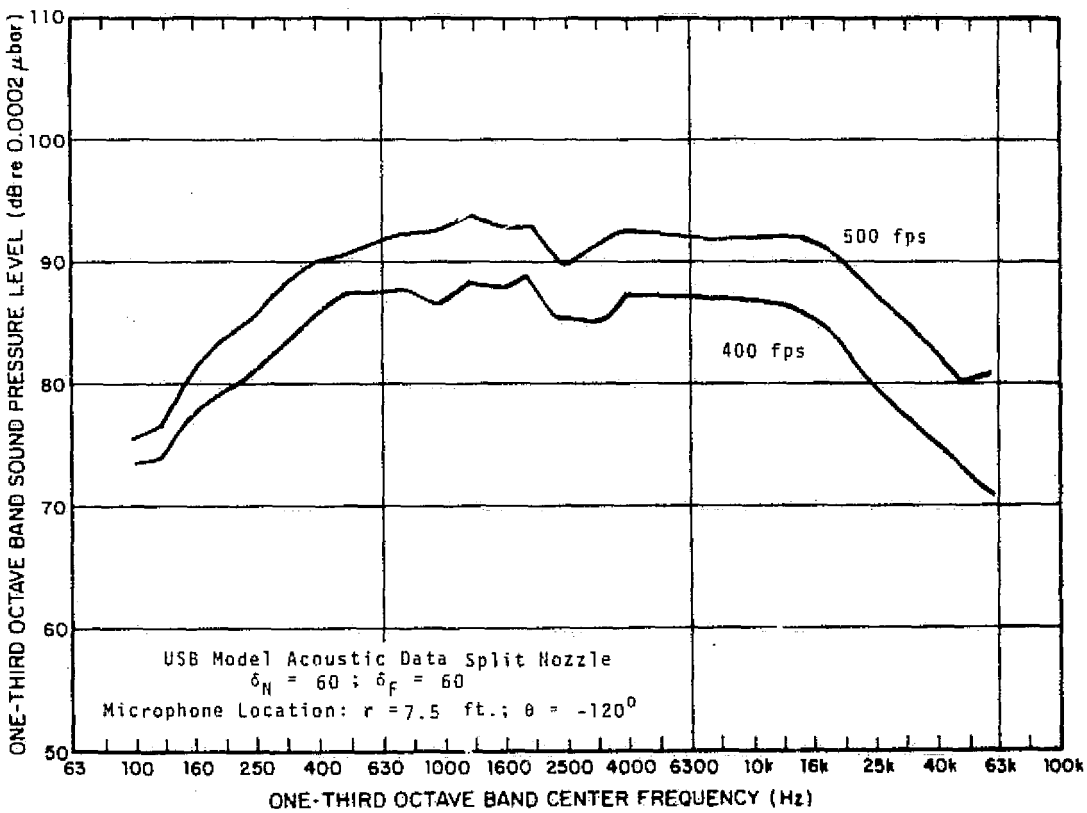

FIG. B- 54 RAW DATA FROM PROPULSIVE LIFT DEVICE MODEL TEST.

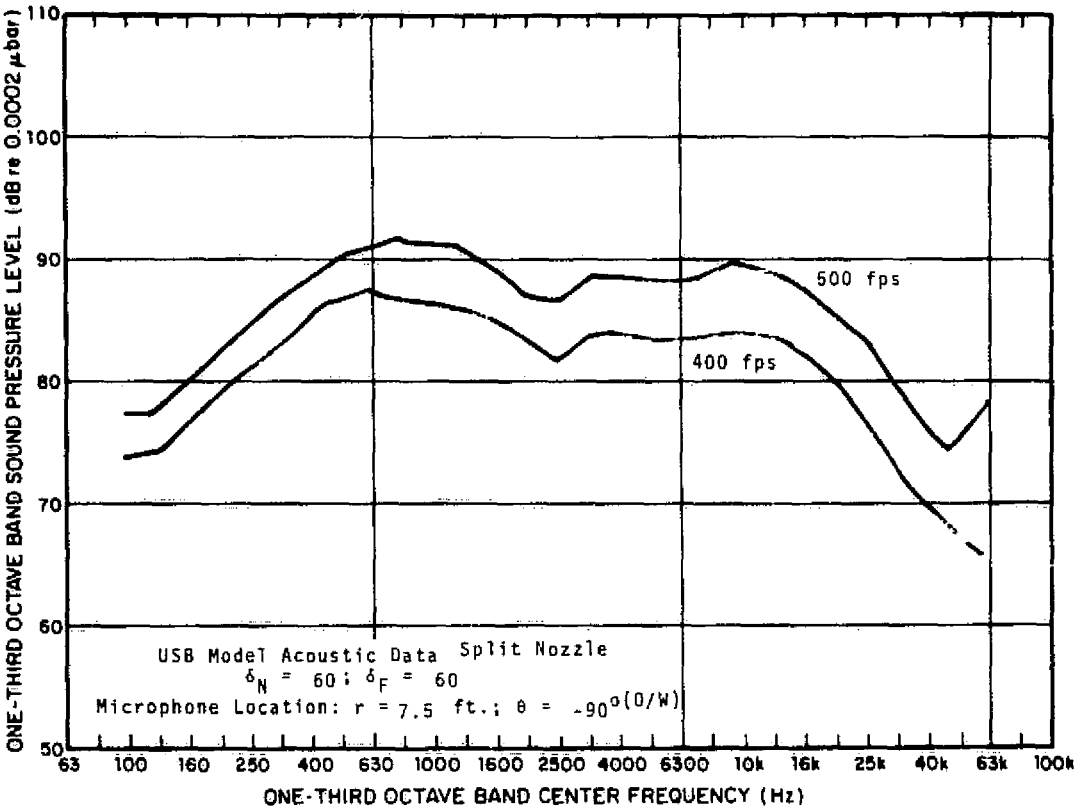

FIG. B- 55 RAW DATA FROM PROPULSIVE LIFT DEVICE MODEL TEST.

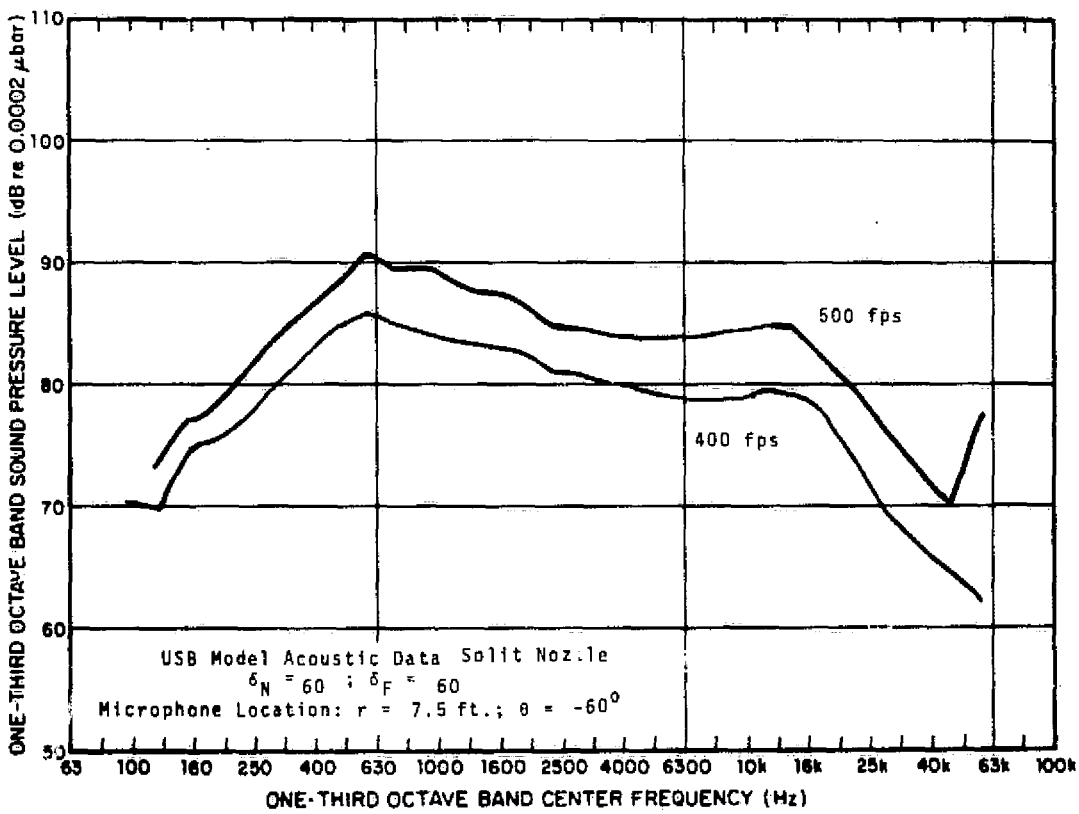

FIG. B- 56 RAW DATA FROM PROPULSIVE LIFT DEVICE MODEL TEST.

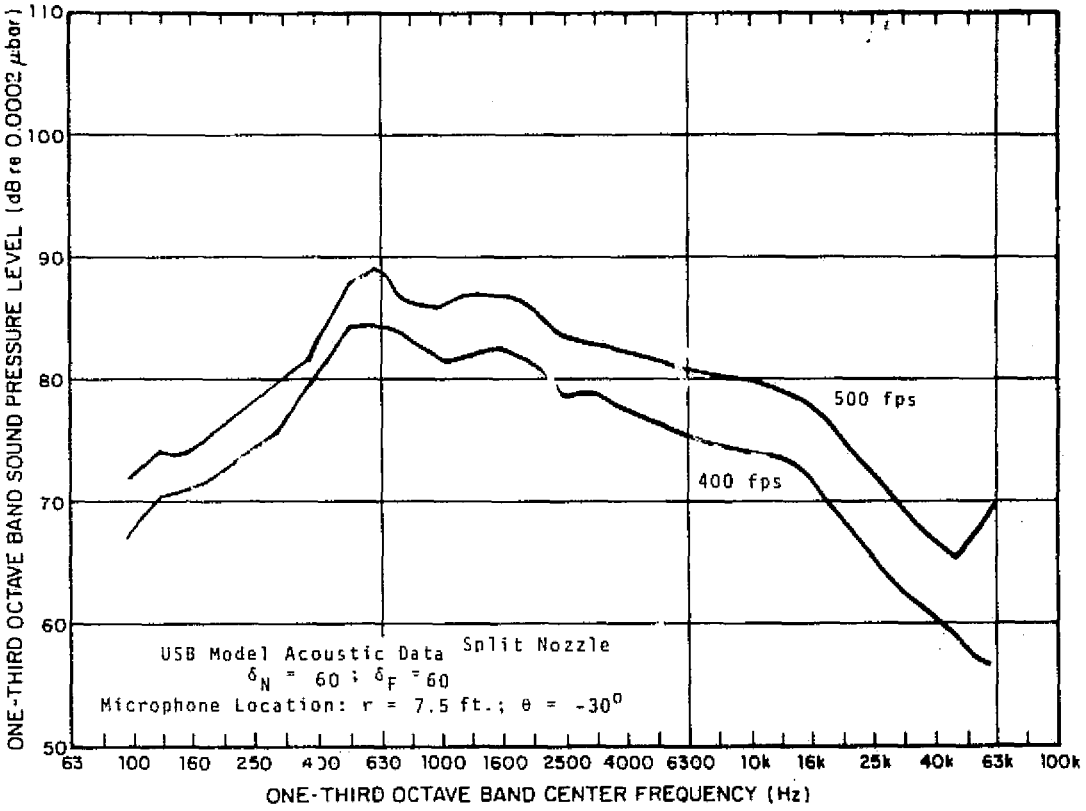

FIG. B- 57 RAW DATA FROM PROPULSIVE LIFT DEVICE MODEL TEST.

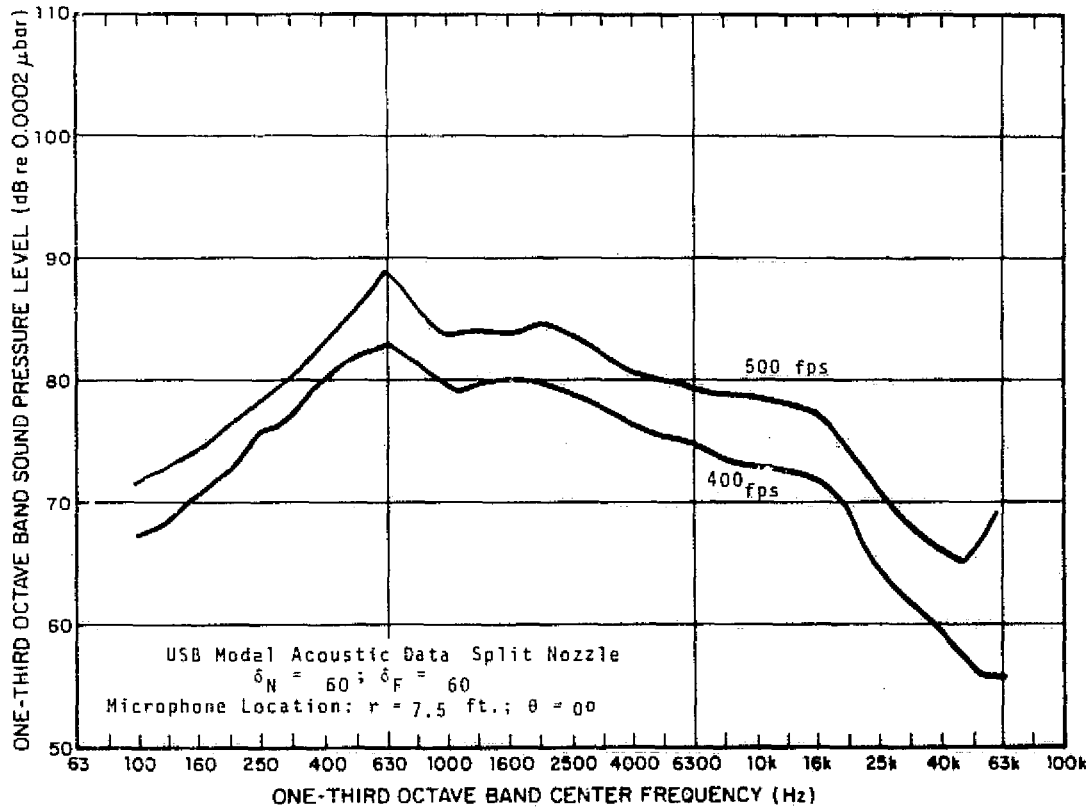

FIG. B- 58 RAW DATA FROM PROPULSIVE LIFT DEVICE MODEL TEST.

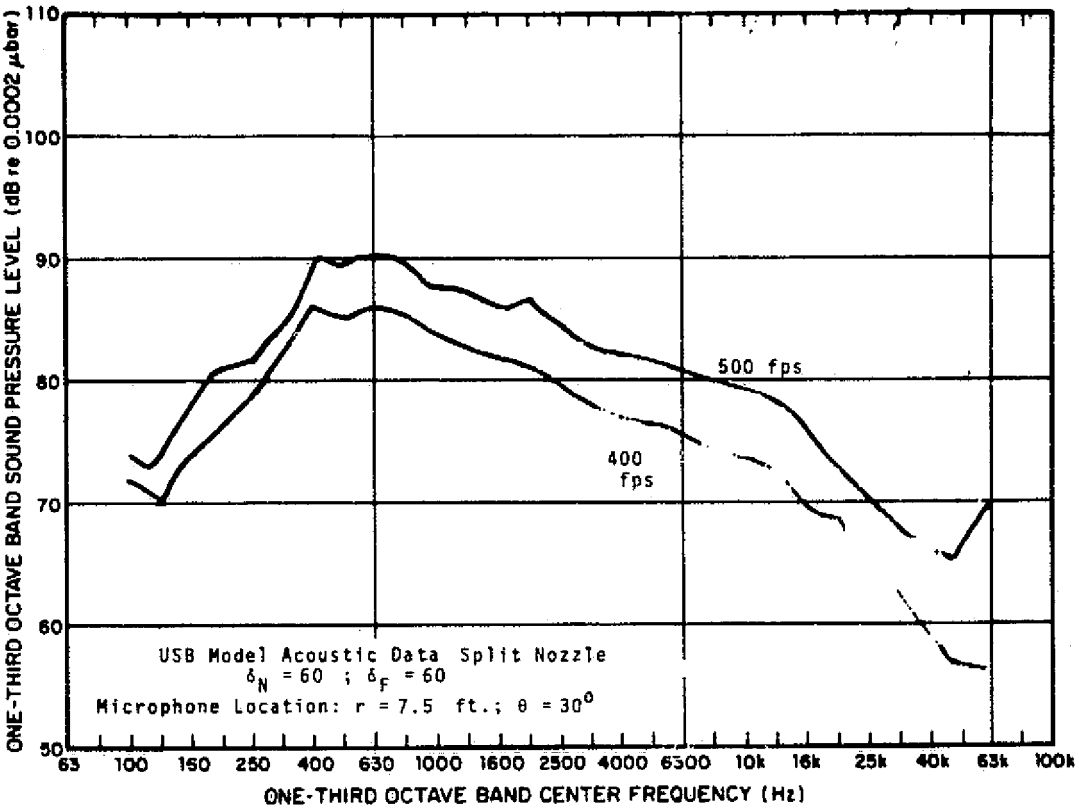

FIG. B- 59 RAW DATA FROM PROPULSIVE LIFT DEVICE MODEL TEST.

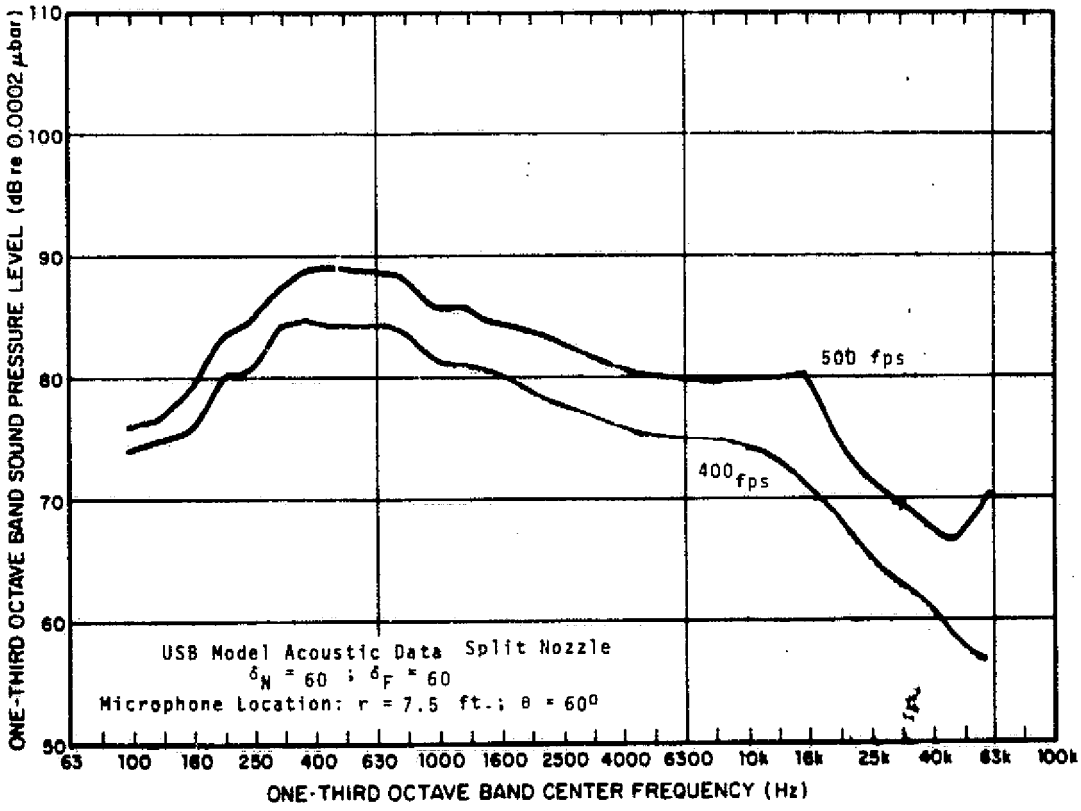

FIG. B- 60 RAW DATA FROM PROPULSIVE LIFT DEVICE MODEL TEST.

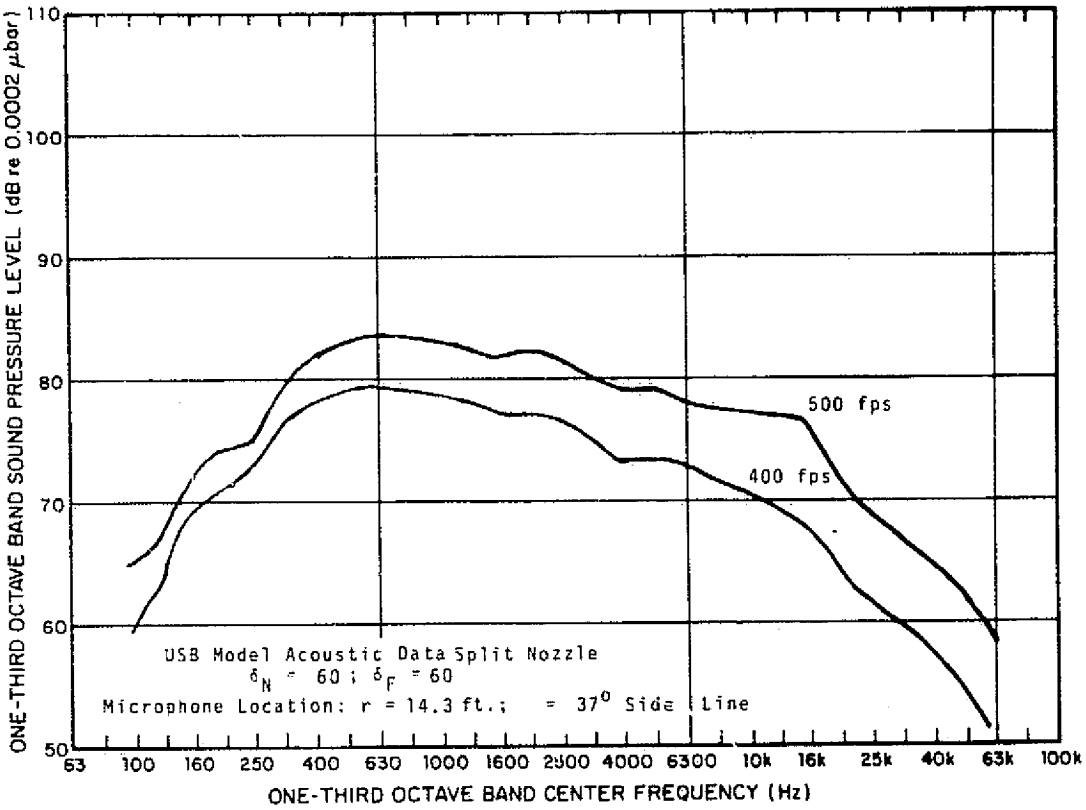

FIG. B-61 RAW DATA FROM PROPULSIVE LIFT DEVICE MODEL TEST.

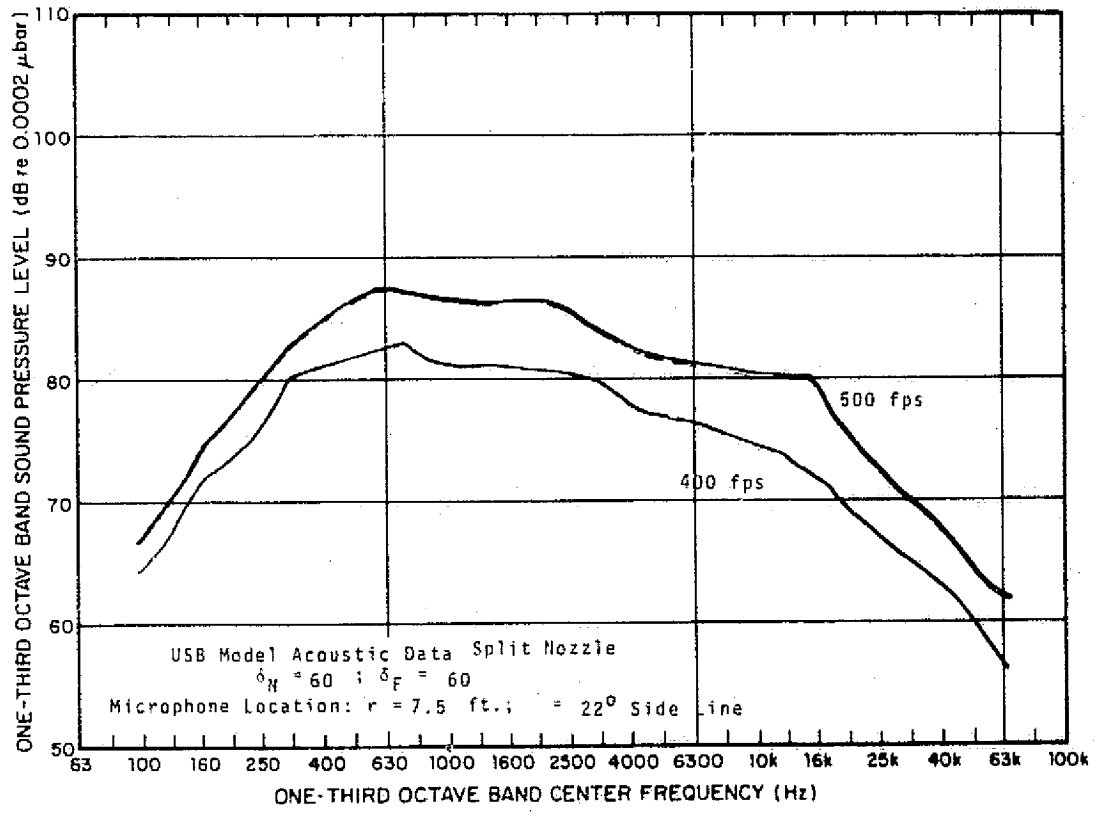

FIG. B-62 RAW DATA FROM PROPULSIVE LIFT DEVICE MODEL TEST.

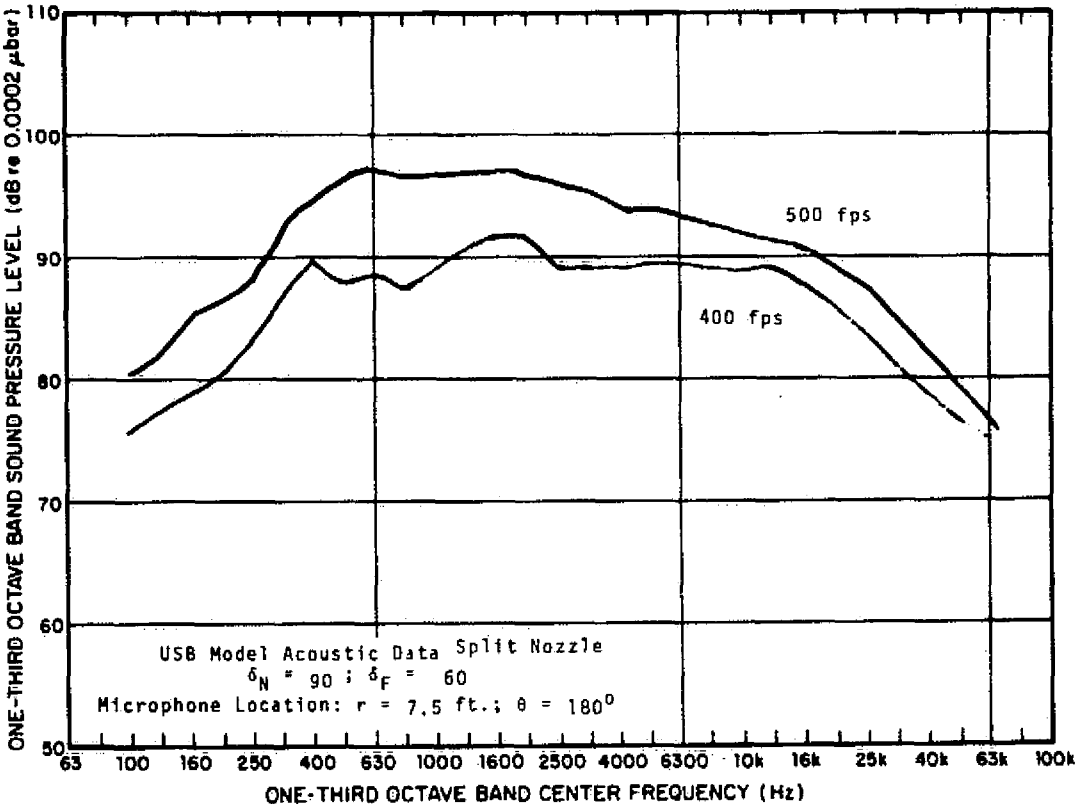

FIG. B-63 RAW DATA FROM PROPULSIVE LIFT DEVICE MODEL TEST.

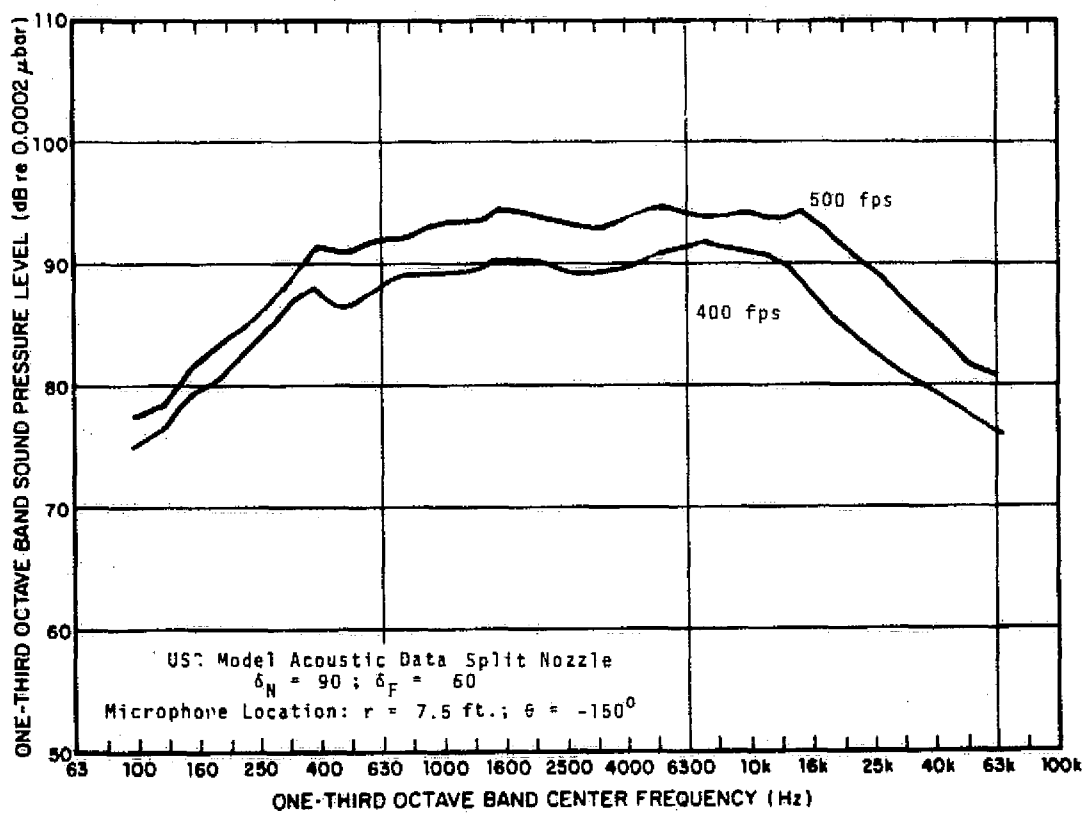

FIG. B- 64 RAW DATA FROM PROPULSIVE LIFT DEVICE MODEL TEST.

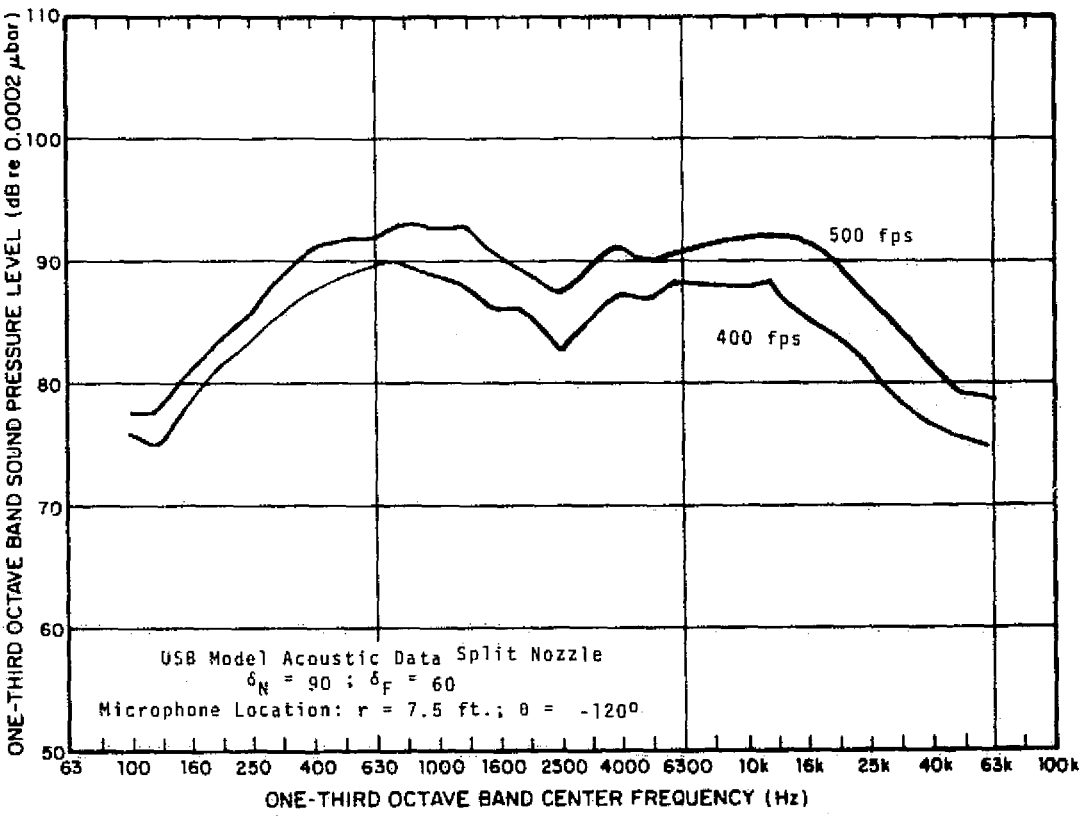

FIG. B- 65 RAW DATA FROM PROPULSIVE LIFT DEVICE MODEL TEST.

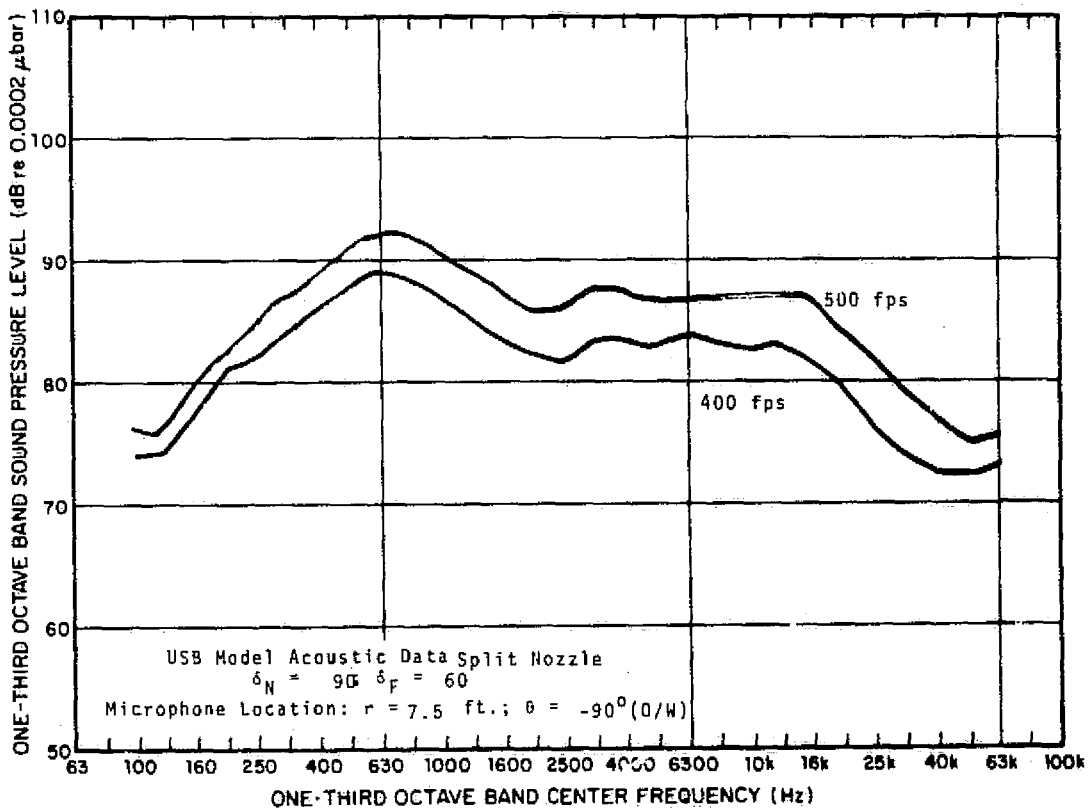

FIG. B- 66 RAW DATA FROM PROPULSIVE LIFT DEVICE MODEL TEST.

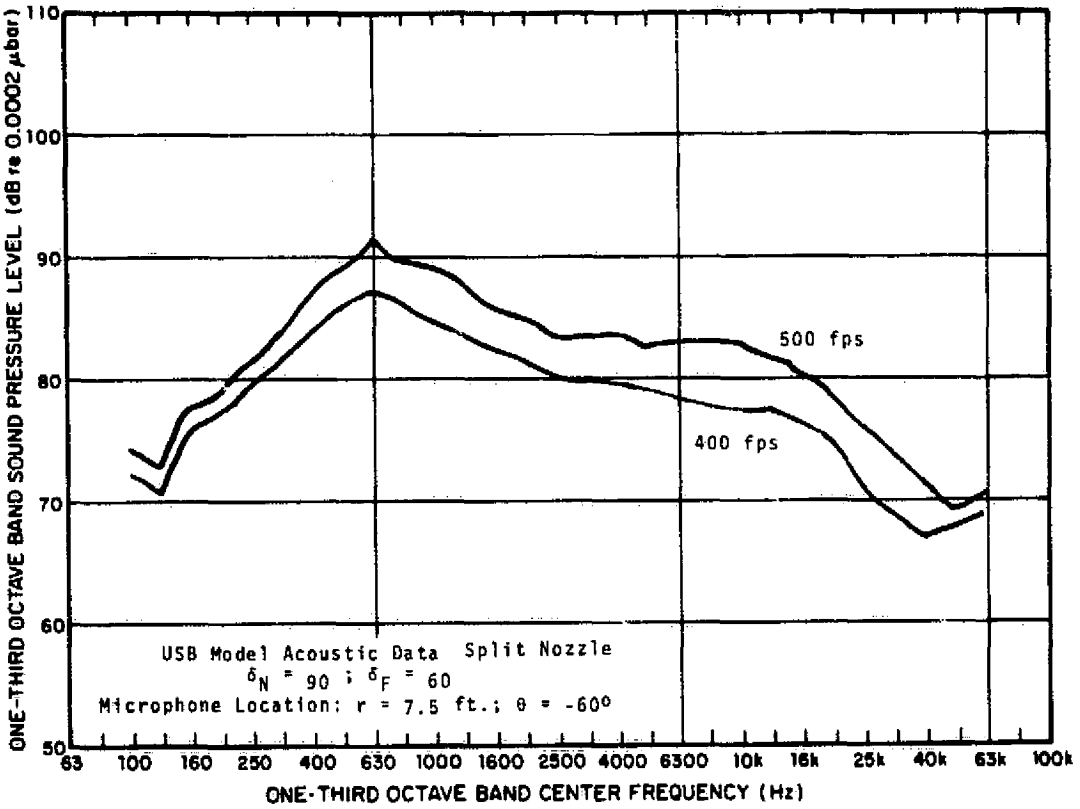

FIG. B- 67 RAW DATA FROM PROPULSIVE LIFT DEVICE MODEL TEST.

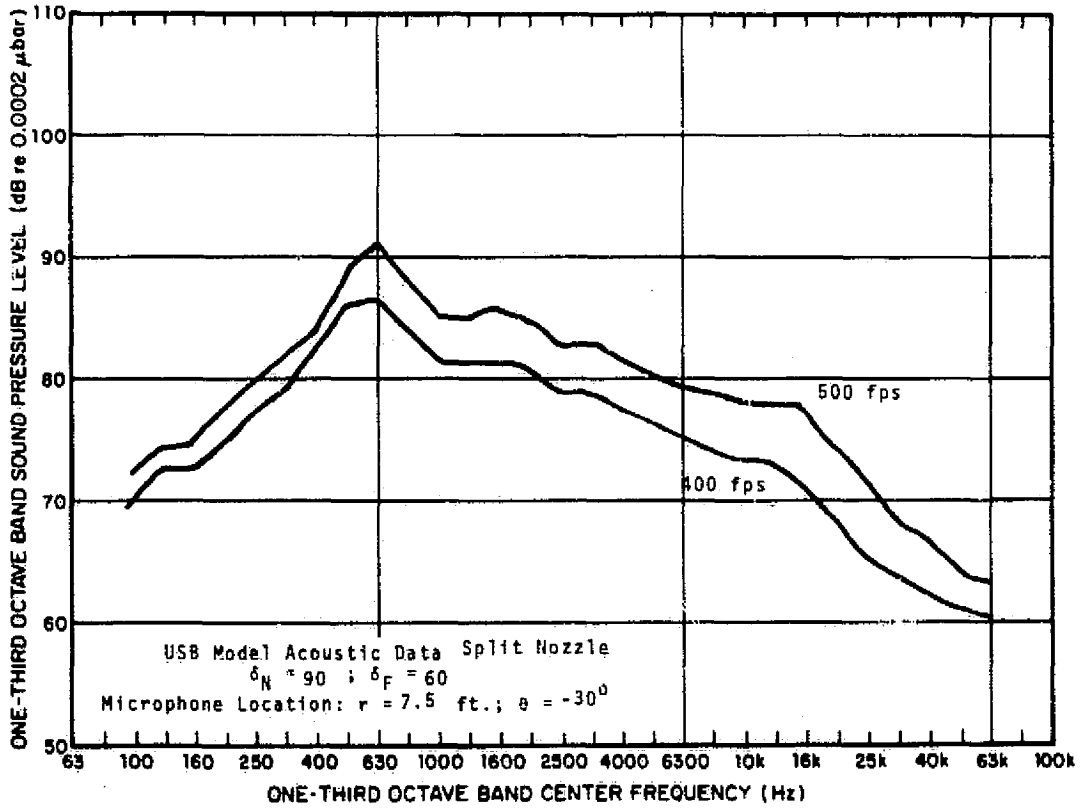

FIG. B- 68 RAW DATA FROM PROPULSIVE LIFT DEVICE MODEL TEST.

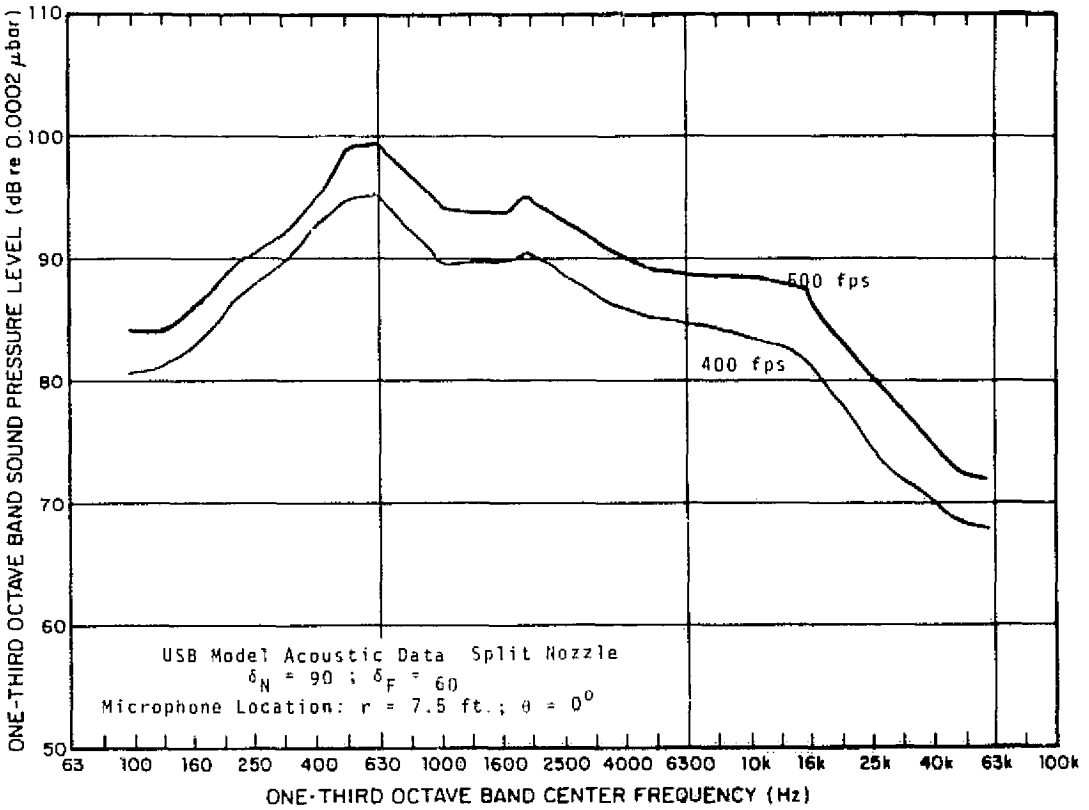

FIG. B- 69 RAW DATA FROM PROPULSIVE LIFT DEVICE MODEL TEST.

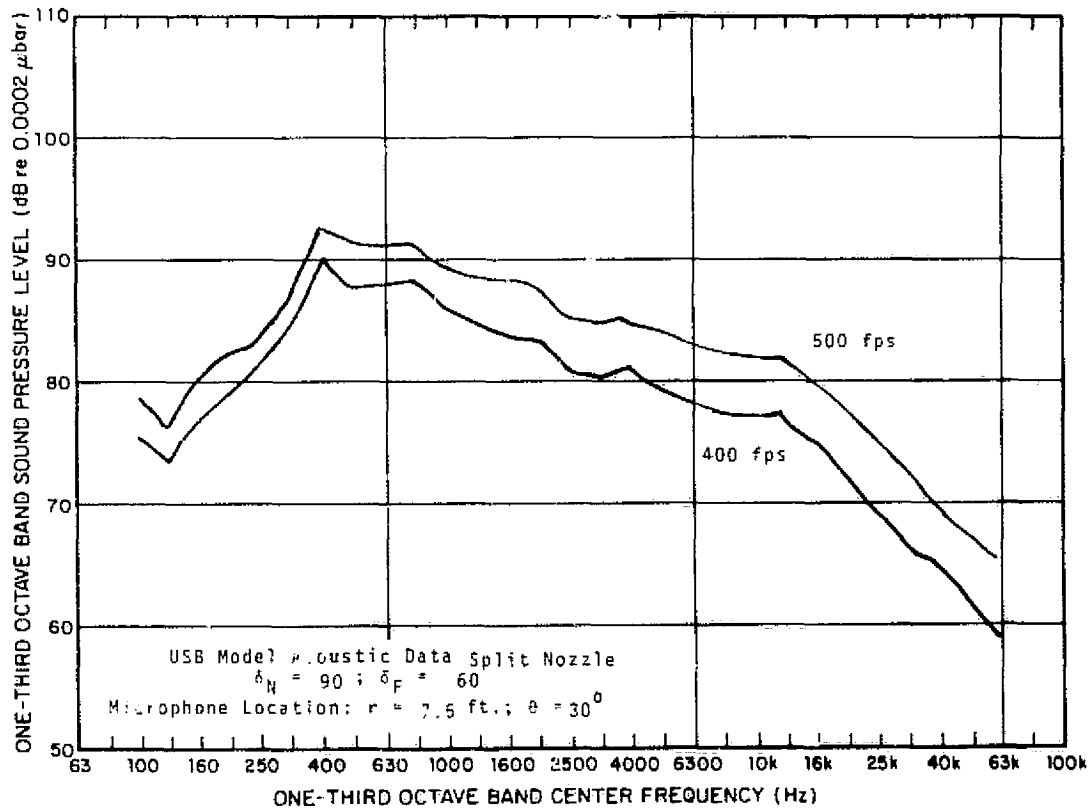

FIG. B- 70 RAW DATA FROM PROPULSIVE LIFT DEVICE MODEL TEST.

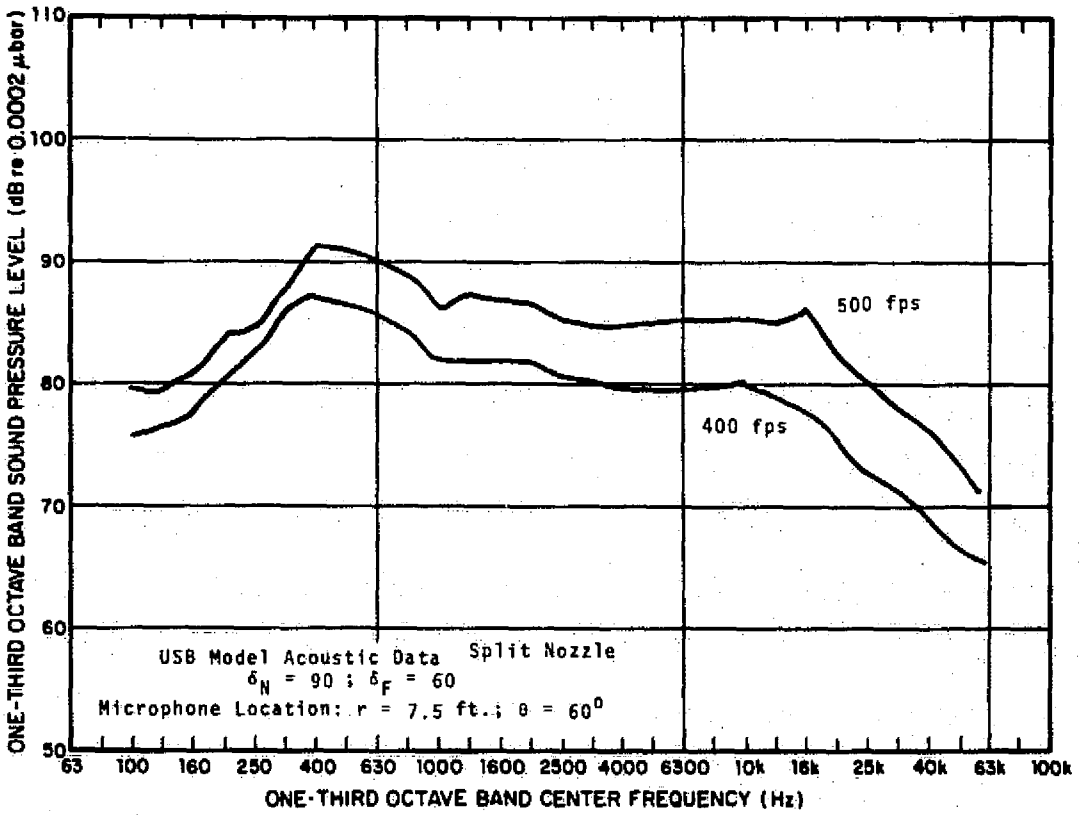

FIG. B-71 RAW DATA FROM PROPULSIVE LIFT DEVICE MODEL TEST.

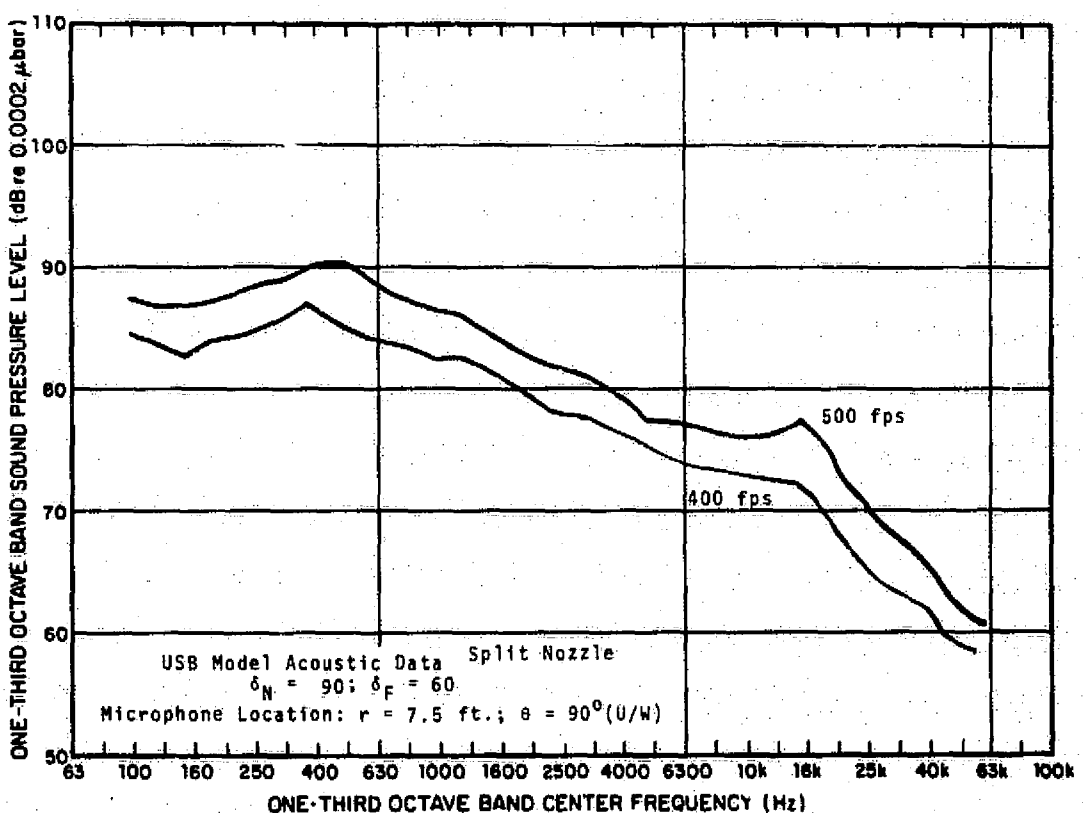

FIG. B-72 RAW DATA FROM PROPULSIVE LIFT DEVICE MODEL TEST.

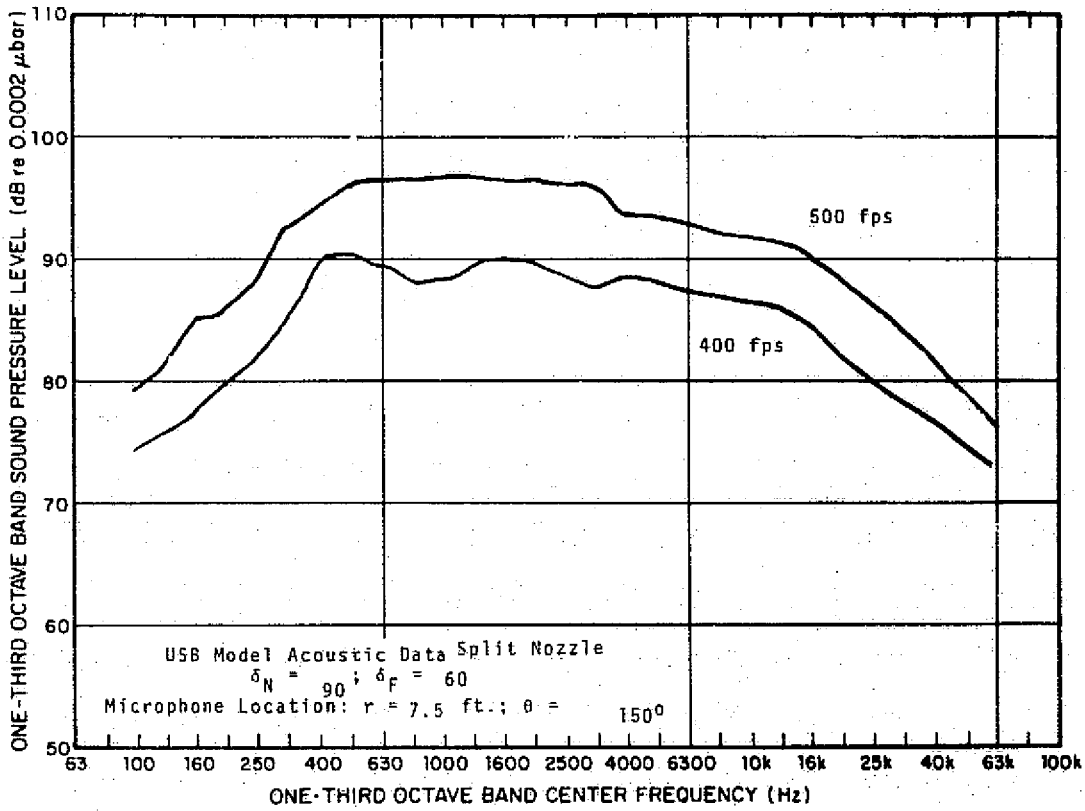

FIG. B- 73 RAW DATA FROM PROPULSIVE LIFT DEVICE MODEL TEST.

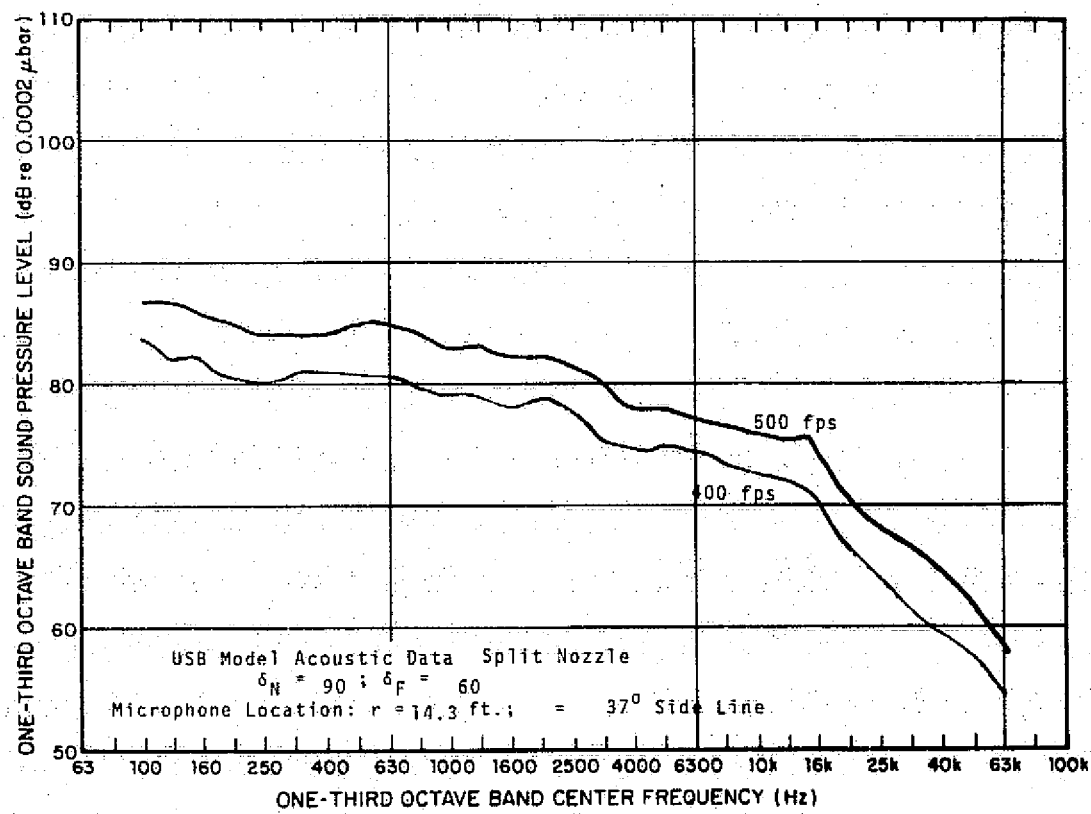

FIG. B- 74 RAW DATA FROM PROPULSIVE LIFT DEVICE MODEL TEST.

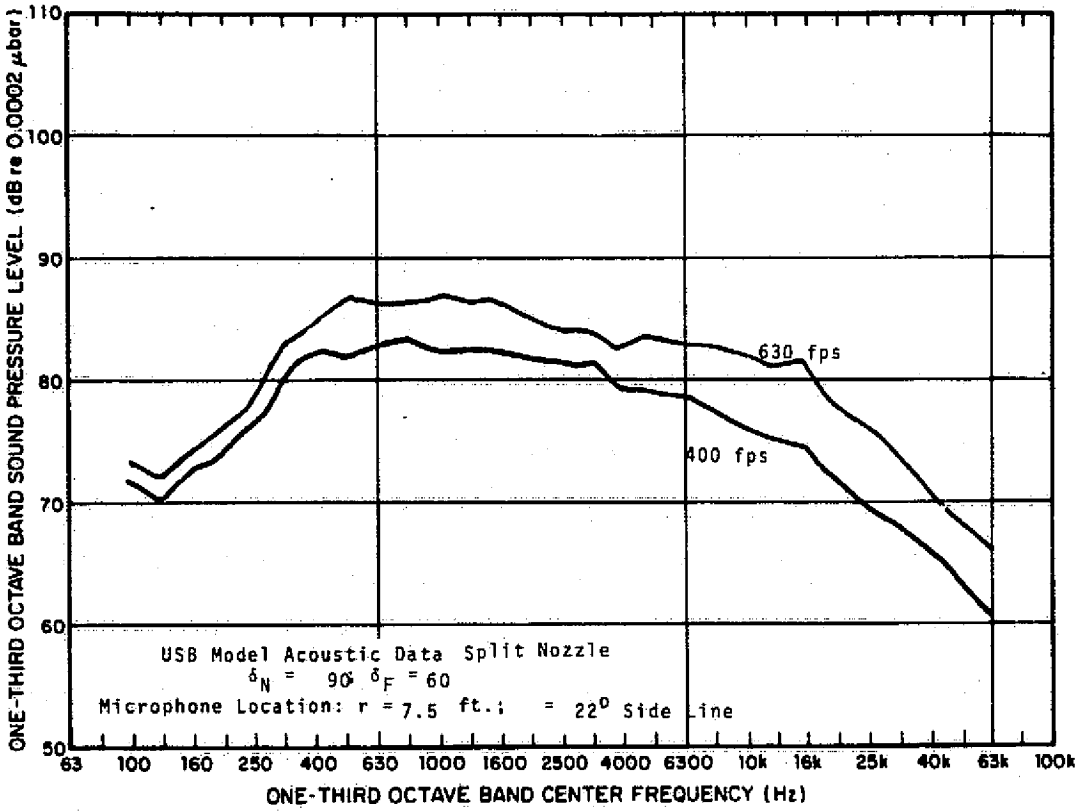

FIG. B- 75 RAW DATA FROM PROPULSIVE LIFT DEVICE MODEL TEST.